Spin polarized electron transport and the anomalous Hall effect in $L1_0$-ordered epitaxial Fe-alloys

PhD Thesis

Submitted in accordance with the requirements for the degree of

Doctor of Philosophy

Klaus Michael Seemann

School of Physics and Astronomy

Condensed Matter Department

University of Leeds

11 February 2009

Examiners: Prof. Russell Cowburn

Prof. Denis Greig

Supervisors: Dr. Christopher Marrows

Prof. Bryan Hickey

Contents

List of Figures

List of Tables

Abstract

Two epitaxial ferromagnets FePd and its isoelectronic partner FePt, which order in the well known face-centered tetragonal $L1_0$-phase, have been fabricated to (a) evaluate the current spin polarization in the ballistic and in the diffusive electron transport regime, (b) to elucidate whether there is a discrepancy in the current spin polarizations depending on the transport regime, how high this discrepancy is, and finally (c) how the spin-orbit scattering strength changes by replacing Pd by Pt. These are questions of fundamental importance in the field of electron transport studies in magnetic materials, in the recent years known as spintronics.

The study began with experimental investigations on the structural, magnetic, and electron transport properties of a $L1_0$-ordered epitaxial iron-platinum (FePt) alloy layer fabricated by magnetron-sputtering on a single-crystal MgO(001) substrate. At all temperatures ranging from 2 K to 258 K, a diffusive spin current polarization of $> 80\%$ was found. To study the ballistic transport regime, point-contact Andreev-reflection measurements at 4.2 K were performed and a value for the ballistic current spin polarization of $\sim 42\%$ was obtained (which compares very well with that of a polycrystalline thin film of elemental Fe). This discrepancy is attributed to a difference in the characteristic scattering times for oppositely spin-polarized electrons,

such scattering times influencing the diffusive but not the ballistic current spin polarization.

One of the main parameters in the $L1_0$-phase ferromagnets is the degree of crystallographic long range ordering. To investigate the influence of the long range ordering on the current spin-polarization, epitaxial FePd magnetic thin films of varying degrees of $L1_0$-phase chemical order were used. By quantitatively accounting for changes in micromagnetism through simulation and magnetic force microscopy, it is shown within the Levy-Zhang spin-mistracking theory of domain wall resistance, that this is connected to a change in the average degree of spin-dependence at the scattering centers that control the diffusive transport in this system, suggesting a possible means of producing highly spin-polarized currents in the diffusive electron transport regime.

Finally, both materials $L1_0$-FePd and -FePt were investigated with respect to the anomalous Hall effect as a consequence of spin-orbit scattering. A linear dependence between transverse and longitudinal resistivity in epitaxial $L1_0$-ordered FePd and FePt films due to the anomalous Hall effect (AHE) has been observed. In ordered ferromagnets such a linear relation may be anticipated due to the skew-scattering mechanism; the absence of an additional quadratic term suggests that side-jump scattering, which is dominant in less well ordered material, has been effectively suppressed. One finds that on exchanging Pd for the heavier, though isoelectronic Pt, the skew-scattering deflection angle in an individual electronic scattering event dramatically increases from 17 to 49 mrad. This increase corresponds well to a $Z^{3/2}$ dependence of the atomic spin-orbit interaction energy, contrary to commonly

assumed Z^4 dependence.

Chapter I

Introduction

The degree of spin-polarization of a electrical current flowing in a magnetic thin film is of central interest in spin electronic applications [6]. It can be considered as the source strength flowing into an electronic device transforming the spin signal of electrons. The influence of spin-dependent scattering of conduction electrons in a crystallographically ordered magnetic thin film on the degree of current spin-polarization was unknown to date. The question as to whether there is a difference of current spin polarization in the ballistic transport regime compared to the diffusive one, the two relevant for spintronic applications besides tunnelling transport, quickly arises.

Secondly, one of the most fundamental physical effects in ferromagnetic material, the spin-orbit scattering of conduction electrons leading to the extraordinary Hall effect also known as the anomalous Hall effect and its dependency on the mass of the scattering center has not been elucidated experimentally very well. Neither was it clear, whether skew scattering or side jump scattering of conduction electrons would dominate in a crystallographically well ordered ferromagnetic system.

Additionally, recent advances in the research field of current induced magnetization switching and current driven magnetization dynamics[7] as well as the developments in the hard disk drive industry to change the magnetic storage process to perpendicular magnetic recording caused a resurgence of interest in epitaxial material with out-of-plane magnetic anisotropy[8, 9, 10]. This upsurge in research interest in epitaxial material exhibiting a high perpendicular uniaxial anisotropy constant has been stimulated especially since sputter deposition now yields epitaxial thin films of an ordering quality comparable to molecular beam epitaxy. This makes fundamental physical phenomena like magnetoresistance due to electron scattering at magnetic domain walls accountable on a similar or even equal scale in sputter deposited material. The chemical long range order parameters achieved on a regular basis by epitaxial magnetron sputtering are comparable with that of other groups in the world [11, 12, 13] and the magnetoresistance due to domain wall scattering is at least equally high as for the same type of material grown by molecular beam epitaxy (MBE) [14]. While the anomalous Hall effect has been receiving extensive attention in ferromagnetic metals and magnetic multilayers[15, 16], domain wall scattering has been a research topic in some early experimental work [17, 18] and has drawn increased attention in the recent years [19, 20, 21] since imaging magnetic domains and domain walls [22, 23] especially of out-of-plane magnetized material on insulators has become more readily feasible by magnetic force microscopy or photo-excitation electron microscopy [24, 25]. The effect of an increased electric resistivity in the presence of magnetic domain walls in a ferromagnetic thin film was predicted theoretically by Levy et al. [26] based on a Hamiltonian employed

to calculate giant magnetoresistance in a spin-split system and was experimentally discovered by Viret et al. [27].

It was the discovery of the giant magnetoresistance in 1988 by Peter Grünberg [28] and Albert Fert [29] that sparked an enormous research activity in a subfield of electron transport studies in magnetic materials, which evolved into what is now known as spintronics. Particularly stunning is in this respect, that a fundamental physical phenomenon that yielded the Nobel Prize in Physics 2007, arrived at the consumer market as an application in the form of the read-head of the modern hard-disk drive only ten years after its discovery in the laboratory. Spintronics essentially is a short form for spin-electronics that incurs that the electron's spin, i.e. the magnetic moment of the electron, governs transport characteristics in addition to the electron's charge.

The experiment of Otto Stern and Walther Gerlach in 1922 [30] proved the quantization of spin-direction of a beam of Ag-atoms passing through a magnetic field [31]. Similarly, the spin of a conduction electron passing through a magnetic material is aligned either parallel of anti-parallel to the magnetization. This essentially justifies the Mott-two-current resistor model [32, 33, 34], where two largely independent spin-currents cause $R_{\downarrow}$ and $R_{\uparrow}$ according to spin-dependent scattering rates. One way to influence electron transport in magnetic materials is to change the concentration of spin-dependent scattering centers. A more convenient way on the other hand is to fabricate magnetic layer systems where spin-dependent scattering depends on the relative orientation of magnetization. Such systems additionally make physical phenomena like spin-dependent scattering or the spin-dependent tunnelling effect employable. The latter, discovered already

in 1975 by Jullière [35], which centers around two ferromagnetic layers separated by a insulating or semiconducting tunnelbarrier is considered to be the predecessor to the giant magnetoresistance (GMR) effect [28, 29]. GMR occurs as in a multi-layer system of alternating ferromagnetic/non-magnetic materials, that gives rise to a high resistance state when the direction of magnetization of the ferromagnetic layers are aligned anti-parallel and likewise a low resistance state is manifested when the ferromagnetic layers are aligned parallel. This phenomenon is caused by spin-dependent scattering of the spin-up and spin-down electrons passing through the individual layers and is employed for more than ten years already in the commercial read-heads and has paved the way for ultra-high data densities in modern hard disk drive technology. Interestingly, the tunnelling magnetoresistance effect (TMR) is becoming dominant now commercially in MRAM-based storage devices (Magnetic Random Access Memory) and also biosensors.

The latest research focus centers around current induced magnetization switching, which is based on spin transfer torque of a highly spin-polarized electron current that initially causes the local magnetization of a ferromagnetic layer to precess and eventually to switch direction altogether at increased current densities [36, 37, 38]. Current induced magnetization switching is considered most suitable for write-processes in MRAMs or for nanoscale microwave sources. Closely related to current-induced magnetization switching is magnetic domain wall motion based on spin-transfer torque, which led to a new concept for data mass storage [39] and a vibrant field of new research [40, 41, 42, 43, 44].

This thesis is structured to contain a brief introduction to the relevant theory with respect to spin-polarized currents in a ferromagnet. Here, in particular the Levy-Zhang theory covering the diffusive electron transport regime is outlined in more detail and stands against the Blonder-Tinkham-Klapwijk theory governing the ballistic electron transport regime. Complementarily, the theoretical picture of skew scattering and side jump scattering of conduction electrons is depicted in ferromagnetic material magnetized perpendicular to the film plane. Both scattering mechanisms are the origin of the anomalous Hall effect discovered by E. H. Hall in 1879 [45].

The first experimental chapter outlines the physical methods employed to fabricate and characterize epitaxial $L1_0$-ordered FePt and FePd. Beginning with the principles of magnetron sputtering as a method of deposition, vibrating-sample magnetometry as the method of choice in determining the anisotropy energy constant, exchange stiffness parameter and saturation magnetization is described subsequently. Followed by a brief introduction to x-ray diffraction as a means of determining the crystallographic long range parameter of the fabricated magnetic thin films, this chapter continues with magnetic force microscopy MFM as representative of the scanning probe family. This technique is utilized as a rapid, inexpensive and reliable experiment to image the magnetic domain pattern in zero applied field and at room temperature. Complementarily to this, the considerably more sophisticated method of x-ray magnetic dichroism photoelectron microscopy XMCD-PEEM provides electron microscopic images of the magnetic domain pattern not relying on the detection of magnetic surface stray fields as in the case of MFM. This is reassuring with respect to the magnetic proper-

ties of the films investigated and has been shown on $L1_0$-FePt and -FePd for the first time at the BESSY synchrotron facility by the group around W. Kuch. Besides x-ray crystallographic studies to determine the degree of long range ordering of the thin film material of a typical thickness of 30 nm, carefully performed high-resolution transmission electron microscopy (HRTEM) in particular in $L1_0$-FePt and the correlation of these data with routine x-ray diffraction experiments, that also have been executed for the epitaxial $L1_0$-FePd films. Subsequently, a strong focus lies on the electron transport properties in two regimes, the ballistic one in the form of point contact Andreev spectroscopy experiments (PCAR) and the diffusive transport regime via magnetoresistance measurements involving domain wall scattering of conduction electrons. While some of the magnetoresistance measurements were carried out directly on non-patterned sheet film material to probe for electron transport properties in 4-probe DC measurements or point-contact Andreev reflection measurements, a dry-etching process has been developed to pattern Hall bar structures to assess spin-orbit scattering events associated with the pronounced anomalous Hall effect observed in $L1_0$-FePt and -FePd. One essentially employs a negative-tone resist that provides sufficient etch-selectivity in an argon-ion milling process to provide for a satisfactory smooth edge-definition in the Hall bars used to study the anomalous Hall effect.

The experimental results giving insight into fundamental aspects like spin-dependent scattering leading to high current spin polarizations but also the spin-obit interaction giving rise to anomalous Hall effect are presented beginning with a description of the details of the deposition process and the key

parameters of structural and magnetic characterization. The central experiments here are x-ray crystallography and vibrating-sample-magnetometry (VSM) at variable temperatures, both in a quantitative manner. From the (001)- and (002)- peaks exhibited as a pronounced hallmark of $L1_0$-order in x-ray crystallographic analysis a long range order parameter was determined, that ranges in $0.4 \leq S_{\mathrm{Order}} \leq 0.8$ in FePd and reaches $S_{\mathrm{Order}} = 0.9$ in FePt. The ferromagnetic hysteresis was measured in a vibrating-sample magnetometer in a temperature interval ranging between $(50 \leq T \leq 280)$ K, which is the basic data necessary to evaluate the micromagnetic parameters A, $K_{\perp}$ and M. Subsequently, a thorough micromagnetic simulation based on the Landau-Lifshitz-Gilbert equation serves as a corroboration for the three experimentally determined magnetic parameters, i.e. exchange stiffness constant A, saturation magnetization M and uniaxial anisotropy constant $K_{\perp}$ the uniaxial anisotropy constant of the ferromagnets FePt and FePd. The OOMMF code made available by the US National Institute of Standards and Technology in conjunction with customized parameter files form the core of simulations of the zero-field domain pattern based on experimentally relevant parameters. This procedure yields a result that is directly comparable with domain images obtained in experiments such as MFM or XMCD-PEEM. A straight forward Fourier-analysis gives a further means of verification between experiment and simulation on the basis of the average domain width. Based on the Levy-Zhang model [26] one is able to evaluate the diffusive current spin polarization at 4.2 K in order to directly compare with point contact Andreev reflection experiments. While the diffusive current spin polarization is evaluated to be in the range of $0.85 - 0.90$, one simultaneously observes a

ballistic current spin polarization for $L1_0$-ordered films of $0.48 - 0.5$, which lies close to that of a polycrystalline film of elemental Fe (~ 0.45).

Finally, in a separate section, both $L1_0$-FePt and the isoelectronic FePd have been analyzed with respect to their anomalous Hall properties. The anomalous Hall coefficient has been determined for both alloys and its discrepancy is found to have its origin in the skew-scattering Hall angle, i.e. the deflection angle of an individual spin-orbit scattering event of a conduction electron from an impurity. The skew scattering Hall angle increases by approximately a factor of 3 from 17 mrad in $L1_0$-FePd to 49 mrad in $L1_0$-FePt per individual scattering event. This is to be attributed to replacing Pd by the much heavier Pt and follows the $Z^{3/2}$ dependence of the valence spin-orbit interaction strength as predicted theoretically [46, 47, 48].

Finally a conclusion and outlook is given addressing possible applications for $L1_0$-material such as epitaxial spin-polarizers in semiconductor-based spin-transistors or novel magnetic devices exploiting the pronounced anomalous Hall effect in conjunction with a highly spin-polarized diffusive current. Last but not least, extremely narrow Bloch-type domain walls of only ~ 10 nm inherent to $L1_0$-FePd as well as -FePt render these materials as candidates of enormous interest in domain wall spintronic devices that are functional at room temperature and above.

Chapter II

Theory

II .1 Spin-polarized currents in a ferromagnet

The Stoner-exchange splitting of the electron density of states in the d-band of a ferromagnet gives rise to different subband structures for $\uparrow$-electrons and $\downarrow$-electrons, which essentially behave as two parallel conduction channels. This fact led Mott to develop his two-current resistor model [32, 33, 34]. As a consequence, currents flowing through a ferromagnet are spin-polarized and according to the nature of the current, be it ballistic of diffusive, one has to distinguish between a ballistic and a diffusive spin-polarization.

II .1.1 Diffusive spin-polarization

In the diffusive electron transport regime the mean free path of the electron is considerably shorter than the dimensions of the structure through which the current is flowing, also called the sample length. On the other

hand, in the ballistic electron transport case, the sample length is shorter than the electron mean free path. In diffusive electron transport, pictorially spoken, electrons are traveling ballistically between collisions, although undergoing many collisions as they traverse the sample. This means at the same time that the electrical resistivity is determined by electron collisions with phonons, magnons and also by scattering from impurities and defects. Each collision can cause the electron spin to flip, such that in a conventional non-magnetic metal the common ordering of the physical lengths electron mean free path λ_{t}, spin diffusion length l_{sf} and mean distance between spin-flipping collisions λ_{sf} is: $\lambda_{\mathrm{t}} < l_{\mathrm{sf}} < \lambda_{\mathrm{sf}}$.

Considering ↑- and ↓-electron conduction channels within a ferromagnet with inherent spin-split electron density of states as introduced by Mott, one arrives qualitatively at separate electron mean free paths $\lambda_{\uparrow}^{\mathrm{F}}$ and $\lambda_{\downarrow}^{\mathrm{F}}$ with a general understanding of ↓-electron scattering being stronger than ↑-electron scattering. This causes asymmetric electron scattering and essentially also gives rise to separate spin-diffusion lengths $l_{\uparrow}^{\mathrm{F}}$ and $l_{\downarrow}^{\mathrm{F}}$ [49]. In a ferromagnet, there is one major additional entity of electron scattering over the non-magnetic metal case with its aforementioned scattering centers, namely the magnetic domain wall. The Levy-Zhang model [26] poses a viable model to explain the resistivity of a magnetic domain wall scattering the electrons of a spin-polarized current. This model is based on the Hamiltonian describing giant magnetoresistance (GMR)

$$H_0 = \frac{\hbar^2 \nabla^2}{2m} + V(\overrightarrow{r}) + J\sigma \cdot \widehat{M}(\overrightarrow{r}), \qquad \text{(II .1)}$$

where J denotes the exchange splitting, σ stands for the vector of Pauli-matrices $V(\overrightarrow{r})$ is the nonmagnetic periodic potential and $\widehat{M}(\overrightarrow{r})$ is the unit

vector pointing into the direction of the local magnetization. The scattering of the electrons is given by

$$V_{scatt} = \sum_i \left[v + j\sigma \cdot \widehat{M}(\overrightarrow{r}) \right] \delta(\overrightarrow{r} - \overrightarrow{r}_i), \qquad \text{(II .2)}$$

where $\overrightarrow{r}_i$ is the position of the impurities, v is the Coulomb scattering potential and j represents the spin dependence of the scattering. The diagonalization of H_0 in spin space using a rotation operator around the axis about which the magnetization rotates makes a correction term to the electron wave functions due to the twisting of the magnetization in domain walls

$$V_{pert} = \frac{\hbar^2}{2m}(\sigma \cdot \widehat{n})(\nabla\Theta) \cdot p - \frac{i\hbar^2}{4m}(\sigma \cdot \widehat{n})\nabla^2\Theta + \frac{\hbar^2}{8m}|\nabla\Theta|^2 \qquad \text{(II .3)}$$

as the rotation operator itself does not commute with the kinetic energy operator in case of a non-collinear magnetization, e.g. in a magnetic domain wall. Θ is the angle of the local magnetic moment with respect to the z-axis. This correction term represents a stationary spin mistracking. It is the origin of an additional resistance due to electrons scattering in magnetic domain walls which mixes the currents of both spin channels. The GMR Hamiltonian was first employed to theoretically describe and explain electrical conductivity of magnetic multilayered structures [50] such as the renowned Fe/Cr/Fe system [28, 29].

The Levy-Zhang model enables a quantitative determination of the spin asymmetry parameter $\alpha = \frac{\sigma_\uparrow}{\sigma_\downarrow} = \frac{\rho_\downarrow}{\rho_\uparrow}$ via resistivity measurements of ferromagnetic thin films. From the perturbation Hamiltonian stipulated above in equation II .3 one determines the eigenfunctions of an electron passing through the rotation of magnetization of a magnetic domain wall. Subsequently, the matrix elements of the spin-dependent scattering potential are

accessible. This in turn leads to spin-dependent scattering rates and in conjunction with the respective Boltzmann-distribution function gives finally an expression of the resistivity contribution of a magnetic domain wall [26]. The domain wall magnetoresistance for a isotropic labyrinth domain state is written as summation of the resistivity terms of the current-perpendicular-wall (CPW) and current-parallel-wall (CIW) geometries

$$\Delta\rho = \Delta\rho_{CPW} + \Delta\rho_{CIW} = \frac{\rho_0}{5}\left(\frac{\pi\hbar^2 k_F}{4m\delta_W J}\right)\frac{(\alpha-1)^2}{2\alpha}\left(4+\frac{10\sqrt{\alpha}}{\alpha+1}\right). \quad \text{(II .4)}$$

Herein k_F denotes the Fermi wave vector, δ_W the width of the magnetic domain wall, J the exchange splitting, $\rho_{\uparrow/\downarrow}$ is the resistivity in the spin-up and spin-down channel respectively and ρ_0 is the resistivity of the magnetically saturated system, i.e. a ferromagnet with uniform magnetization.

Depicting the current density J as a function of applied electric field ε and the electron density of states at the Fermi level, $g(E_F)$, according to the classical Drude model [51] $J = g(E_F)e^2\tau\varepsilon/m = \sigma\varepsilon$ and considering the Stoner exchange splitting as the origin to different conductivities for both spin channels then the diffusive current spin polarization can be written as

$$P_{diff} = \frac{J_\uparrow - J_\downarrow}{J_\uparrow + J_\downarrow} = \frac{\sigma_\uparrow - \sigma_\downarrow}{\sigma_\uparrow + \sigma_\downarrow} = \frac{\alpha-1}{\alpha+1} = \frac{g(E_F)_\uparrow \cdot v_{F,\uparrow}^2 \cdot \tau_\uparrow - g(E_F)_\downarrow \cdot v_{F,\downarrow}^2 \cdot \tau_\downarrow}{g(E_F)_\uparrow \cdot v_{F,\uparrow}^2 \cdot \tau_\uparrow + g(E_F)_\downarrow \cdot v_{F,\downarrow}^2 \cdot \tau_\downarrow} \quad \text{(II .5)}$$

as a function of the electron density of states at the Fermi level, the square of the Fermi velocity and the mean relaxation times for both spin channels.

II .1.2 Ballistic spin-polarization

The ballistic current spin polarization is entirely determined by the band structure $E(k_i)$ of the ferromagnet, as the spin coherence length is taken to

be considerably longer than the mean free path of the electron such that relaxation times become irrelevant. A quantitative analysis of the ballistic current spin polarization in a nonmagnet-superconductor contact is described by the Blonder-Tinkham-Klapwijk model [52, 53, 54], which has been modified by G.J. Strijkers et al. [55] to include the spin polarization P_{bal} of a ferromagnet-superconductor junction by decomposing the current $I = (1-P_{bal})I_n + P_{bal}I_P$ into a fully non-polarized and a fully polarized part. The excess current generated by Andreev reflection [56], i.e. the spindependent and coherent back reflection of a quasiparticle into the ferromagnet after the formation of a Cooper pair at the superconductor-ferromagnet interface, depends on the quasi-particle reflection probabilities for the fully non-polarized and the fully polarized part of the current. They are found by solving the Bogoluibov equations, a set of coupled Schrödinger equations in wavefunctions $f(x,t)$ and $g(x,t)$, which describe the reflection and transmission of a particle at a superconductor-nonsuperconductor interface with energy gap Δ and electrochemical potential μ

$$i\hbar\frac{\partial f}{\partial t} = \left(-\frac{\hbar^2\nabla^2}{2m} - \mu(x) + V(x)\right) f(x,t) + \triangle(x)g(x,t) \qquad \text{(II .6)}$$

and

$$i\hbar\frac{\partial g}{\partial t} = \left(-\frac{\hbar^2\nabla^2}{2m} - \mu(x) + V(x)\right) g(x,t) + \triangle(x)f(x,t). \qquad \text{(II .7)}$$

The Bogoluibov transformation functions γ_1, γ_2 and γ_3 for the Bardeen-Cooper-Schrieffer (BCS) quasi-particle states are given by

$$\gamma_1^2 = (u_{01}^2 + Z^2[u_{01}^2 - v_{01}^2]), \qquad \text{(II .8)}$$

$$\gamma_2^2 = (u_{01}^2 v_{01}^2 + (u_{02}^2 - v_{02}^2)[u_{02}^2 + Z^2 + (u_{02}^2 - v_{02}^2)Z^2(1+Z^2)], \qquad \text{(II .9)}$$

$$\gamma_3^2 = (u_{02}^2 - v_{02}^2)[u_{02}^2 + Z^2 + (u_{02}^2 - v_{02}^2)Z^2(1 + Z^2)], \qquad \text{(II .10)}$$

and provide for a consistent formal way to treat the interface of scattering strength Z for cases of clean metallic interface to a mere tunnel junction by matching quasi-particle wavefunctions to account for inelastic scattering at the superconductor-ferromagnet boundary. The Bogoluibov equations are essentially parameterized by the BCS coherence factors, which are given as

$$u_{01}^2 = 1 - v_{01}^2 = \frac{1}{2}\left\{1 + [(E^2 - \Delta_1^2)/E^2]^{1/2}\right\} \qquad \text{(II .11)}$$

$$u_{02}^2 = 1 - v_{02}^2 = \frac{1}{2}\left\{1 + [(E^2 - \Delta_2^2)/E^2]^{1/2}\right\} \qquad \text{(II .12)}$$

and are a function of the superconductor energy gap Δ_1 and an energy gap of a superconducting proximity layer Δ_2 forming inside the ferromagnet. It is pointed out, that in the data analysis of this work only the superconductor energy gap Δ_1 is employed as a fitting parameter, as no features in the conductance spectra taken experimentally indicated the formation of a proximity effect. E denotes the overall system energy and represents the sum of energy of ground state and all quasi-particle excitations.

The total current through the superconductor-ferromagnet junction as a function of bias voltage V is found by integrating the Andreev and normal reflection probabilities for the non-polarized and the polarized current over all energies weighted by the Fermi-Dirac distribution function $f(E,T)$

$$I = 2e \cdot \eta \cdot g(E_F) v_F \int_{-\infty}^{+\infty} [f(E - V, T) - f(E, T)][1 + A - B] dE. \qquad \text{(II .13)}$$

Herein, η denotes the effective cross-sectional area of the contact, $g(E_F)$ is the density of states at the Fermi energy level E_F, v_F is the Fermi velocity, A stands for the Andreev reflection probability coefficient, while B is

the ordinary reflection probability coefficient. The differential conductance $G(V) = \frac{\partial I}{\partial V}$ curves experimentally determined via point-contact Andreev reflection (PCAR) are then fitted employing Z, Δ_1, Δ_2, the temperature T and the current spin polarization P_{bal}. The size of superconductor-ferromagnet junctions $\sqrt{\eta}$ is required to be of the order or lower than the electron mean free path (Sharvin limit [57]) in order to ensure the ballistic nature of the electron/quasiparticle transport across the superconductor-ferromagnet interface. This becomes obvious by comparing the Landauer formula [58]

$$G_L = \frac{2e^2}{h} \cdot \sum_m \sum_l T_{ml} \tag{II .14}$$

for the transmission probability $T_{ml} \approx 1$ of all subband channels m, l with the Sharvin formula [57]

$$G_S = \frac{2e^2}{h} \pi \frac{\eta}{\lambda_F^2}, \tag{II .15}$$

where λ_F is the Fermi wavelength.

II .2 Micromagnetic simulations based on the Landau-Lifshitz-Gilbert equation

Due to limited time and resources available to fabricate and pattern nanoscale devices, micromagnetic simulations are an indispensible tool for the design and the interpretation of experiments and their results. Based on the Landau-Lifshitz-Gilbert equation (LLG) [59, 60]

$$\frac{d\overrightarrow{M}}{dt} = -|\overline{\gamma}|\overrightarrow{M} \times \overrightarrow{H_{eff}} - \frac{|\overline{\gamma}|\alpha_D}{M_S}\overrightarrow{M} \times \left(\overrightarrow{M} \times \overrightarrow{H_{eff}}\right), \tag{II .16}$$

which describes the response of a localized or pointwise magnetization, or more precisely, a magnetic moment $\overrightarrow{M} = (M_x, M_y, M_z)$ with $M_x = M\,(\sin\Theta\cos\Phi)$,

$M_y = M(\sin\Theta\sin\Phi)$ and $M_z = M(\cos\Theta)$ to a pointwise effective field $H_{eff} = -\frac{\overrightarrow{\nabla_m E_m}}{\mu}$. $\overline{\gamma}$ denotes the Landau-Lifshitz gyromagnetic ratio as the ratio of magnetic dipole moment to angular momentum, and α_D the dimensionless Gilbert damping coefficient. The localized spin dynamics comprise a continued precession around the z-direction of an effective field H_{eff} in case of no damping, and a decay of such precession until the localized spin points into the direction of H_{eff} in the presence of damping, which are described by the first and the second terms of the LLG equation. The average energy density E_m is a function of the pointwise magnetization (magnetic moment) $\overrightarrow{M}$ and consists of anisotropy, exchange, demagnetization and applied field terms [61]

$$E_m = \frac{A}{2}\left[(\nabla\Theta)^2 + \sin^2\Theta\,(\nabla\Phi)^2\right] - \frac{K_\perp}{2}\sin^2\Theta + \left(\overrightarrow{D}\cdot\overrightarrow{M}\right)\cdot\overrightarrow{M}\cdot\mu_0 - \mu_0\cdot M\cdot H\cos\Theta, \tag{II .17}$$

wherein A represents the exchange stiffness and $K_\perp$ the uniaxial anisotropy constant of the ferromagnet. $\overrightarrow{D}$ denotes the demagnetization field, μ_0 stands for the permeability constant, Θ and Φ are the zenith and azimuth angle coordinates of the orientation of the local magnetization $\overrightarrow{M}$ in the spherical coordinate system.

To compute the domain state of a magnetic material of known micromagnetic parameters, in an initial step and neglecting Gilbert damping ($\alpha_D = 0$), $\frac{d\overrightarrow{M}}{dt}$ is evaluated via $H_{eff} = -\frac{\overrightarrow{\nabla_m E_m}}{\mu}$ from

$$\frac{d\overrightarrow{M}}{dt} = -|\overline{\gamma}|\overrightarrow{M}\times\overrightarrow{H_{eff}}. \tag{II .18}$$

Subsequently, the micromagnetic Landau-Lifshitz-Gilbert simulation algorithm is initialized with the result of equation II .18

$$\frac{d\overrightarrow{M}}{dt} = -|\overline{\gamma}|\overrightarrow{M} \times \overrightarrow{H_{eff}} - \frac{\alpha_D}{M_S}\overrightarrow{M} \times \left(\frac{d\overrightarrow{M}}{dt}\right)' \qquad \text{(II .19)}$$

and then is integrated pointwise in an iterative process until $\frac{d\overrightarrow{M}}{dt} \approx 0$. This means, that the iteration of equation II .19 will be terminated once $\frac{d\overrightarrow{M}}{dt} < 10^{-5}$, which provides a sufficiently accurate domain state result. Usually, a six-nearest neighbour exchange interaction is employed to assess the average energy density E_m between adjacent cells in a 3-dimensional mesh of typically $1 \times 1 \times 15$ nm^3 sized individual cells for minimizing $\frac{d\overrightarrow{M}}{dt}$ iteratively.

II .3 Anomalous Hall effect

The anomalous or extraordinary Hall effect was first discovered by E. H. Hall in 1881 [45]. In ferromagnetic materials essentially two terms govern the Hall resistivity, observable as a transverse voltage signal upon the application of a longitudinal current. On the one hand there is the ordinary Hall effect dependent on the applied magnetic field H and the material specific ordinary Hall coefficient R_0 according to $\rho_{oH} = \mu_0 \cdot R_0 \cdot H$. On the other hand, an additional Hall component is given by a term directly proportional to the magnetization M of the respective material and its anomalous Hall coefficient R_S and is written as $\rho_{sH} = \mu_0 \cdot R_s \cdot M$. The anomalous Hall contribution essentially contains per definitionem all effects $\propto \overrightarrow{M}$, i.e. on the one hand the part of the Lorentz force proportional to the sample magnetization and on the other hand a contribution again proportional to sample magnetization based on spin-orbit interaction. Due to the equivalent symmetry of both Hall

effects one observes the Hall resistivity as the superposition of ordinary and anomalous Hall effect [62], i.e.

$$\rho_{aH} = \mu_0 \cdot R_0 \cdot H + \mu_0 \cdot R_s \cdot M. \qquad \text{(II .20)}$$

In both components, the anomalous and the ordinary Hall effect, the Lorentz force plays a decisive role in the charge carrier scattering leading to a build up of a transverse electric signal, the Hall voltage. The ordinary Hall effect is a direct consequence of the Lorentz force acting on a charge carrier, $\mathbf{F} = \mu_0 q(\mathbf{v} \times \mathbf{H})$ and similarly, in the case of the anomalous Hall effect the spin-orbit interaction $\mathbf{L} \cdot \mathbf{s}$ is directly related to the radial component of the Lorentz force in essence replacing $\mathbf{H}$ by $\mathbf{M}$. While the anomalous Hall coefficient is determined from the high-field resistivity extrapolated to zero-field, the ordinary Hall coefficient is exhibited in the high-field slope of the magnetization vs. applied field data.

Skew scattering and side jump scattering

The Hall effect in ferromagnetic material has been studied theoretically in terms of the magnitude of the effect as well as its strong temperature dependence based on the fundamental physical phenomenon of spin-orbit interaction [63]. While some theoretical investigations differentiate between the two mechanisms, i.e. skew scattering and side jump scattering, and regard side-jump scattering as the main mechanism in Fe or Ni and their alloys [64], it was J. Smit [65, 66] for the first time who performed a thorough overall comparison of experimental observations with theoretical considerations to explain the order of magnitude of the Hall angle due to anomalous Hall effect in a ferromagnetic material. However, theoretical predictions on the

anomalous Hall effect under consideration of crystallographic order within a ferromagnet as present in $L1_0$-material have only been available in the recent years [67, 68, 69].

One defines the anomalous Hall angle as the ratio between the resistivity due to the anomalous Hall effect ρ_{aH} and overall resistivity in the magnetically saturated state ρ_0, i.e. $\Phi_{aH} = \frac{\rho_{aH}}{\rho_0}$ and are consequently able to express the anomalous Hall angle as [62]

$$\Phi_{aH} = \frac{\rho_{aH}}{\rho_0} = \Phi_{SS} + \text{const} \cdot \rho_0. \qquad \text{(II .21)}$$

Herein, Φ_{SS} denotes the Hall angle caused by skew scattering, which is commonly understood to be the angle of deflection of the electron wave function after an individual scattering event. The microscopic picture of the anomalous Hall effect can be separated into two quantum mechanical mechanisms that give rise to the deflection of the electron trajectory, these are skew scattering and side jump scattering, see figure II .1. A plane electron wave of wave vector **k** being scattered at a central impurity potential gives rise to a spin-dependent anisotropy of the distribution of amplitude and a cascade of such scattering events consequently yields a deflection of the electron trajectory by an angle typically in the range of 10^{-2} radians (figure II .1 (a)). This mechanism is called skew scattering and is intrinsically different from the mechanism of side-jump scattering, which in turn corresponds to a lateral displacement of the center of the wave packet while scattering. The length scale of this lateral displacement is in the range of 10^{-11} m and both effects are a consequence of spin-orbit coupling and, as such are characteristic for the understanding of the anomalous Hall effect leading to a non-zero transverse spin current in addition to the transverse charge current. The expression for

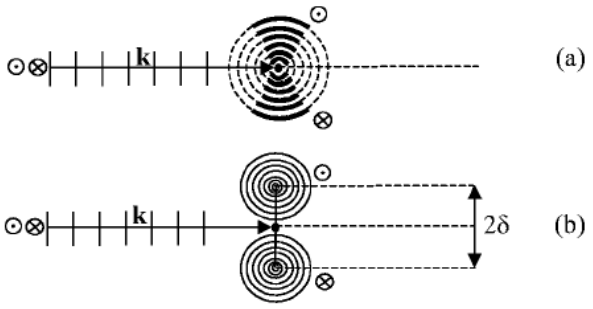

Figure II .1: Microscopic picture of electron wave-packets in the (a) skew-scattering and (b) side-jump scattering event. Both scattering events are spin-dependent leading to a non-zero spin current and a transverse charge current which is the origin of the anomalous Hall effect [67]. The encircled cross denotes the electron spin direction perpendicular into the plane, while the encircled dot marks the electron spin direction perpendicular out of the plane of the drawing. **k** is associated with the electron plane wave traveling from left to right to be scattered from the impurity center.

the Hall angle obtained in equation II .21 does not reveal a direct dependence of Φ_{aH} on the degree of ordering in the case of impurity scattering. To elucidate the fact that the mechanism of skew scattering dominates over side jump scattering in an ordered ferromagnet such as $L1_0$-FePt and -FePd, one turns to ab-initio derivation of A. Crépieux et al. [67].

The Hall angle is understood to be the angle between electric field and the charge current, i.e. for an applied magnetic field into the z-direction and applied electric field into the x-direction, the spin-dependent Hall angle is defined as

$$\tan(\Phi_{aH}^{\uparrow(\downarrow)}) = \frac{j_y^{\uparrow(\downarrow)}}{j_x^{\uparrow(\downarrow)}} = \frac{\tilde{\sigma}_{xy}^{\uparrow(\downarrow)}}{\tilde{\sigma}_{xx}^{\uparrow(\downarrow)}}. \qquad \text{(II .22)}$$

In this definition $j_x^{\uparrow(\downarrow)}$ and $j_y^{\uparrow(\downarrow)}$ denote the current density of the ↑- and ↓-channel for an applied electric field applied in x-direction and an effective magnetic field in the z-direction. $\tilde{\sigma}_{xy}^{\uparrow(\downarrow)}$ and $\tilde{\sigma}_{xx}^{\uparrow(\downarrow)}$ are in a first approximation the sums of conductivity contributions of ↑-electrons and ↓-electrons. The Dirac approach of first-order perturbation theory drawn up by Crépieux et al. [67] is particularly suitable as it yields the off diagonal elements $\tilde{\sigma}_{xy}^{SS}$ and $\tilde{\sigma}_{xy}^{SJ}$ of the anomalous Hall conductivity tensor of a ferromagnetic compound with magnetization into the z-direction

$$\tilde{\sigma} = \begin{pmatrix} \tilde{\sigma}_{xx} & \tilde{\sigma}_{xy} & 0 \\ -\tilde{\sigma}_{xy} & \tilde{\sigma}_{xx} & 0 \\ 0 & 0 & \tilde{\sigma}_{zz} \end{pmatrix} \tag{II .23}$$

for both, skew scattering,

$$\tilde{\sigma}_{xy}^{SS} = -\frac{\pi m^2 \lambda^2}{6\hbar^2} \frac{\langle V^3 \rangle_C}{\langle V^2 \rangle_C} [N_\uparrow \Omega_0 \tilde{\sigma}_{xx}^{\uparrow} (v_F^{\uparrow})^2 - N_\downarrow \Omega_0 \tilde{\sigma}_{xx}^{\downarrow} (v_F^{\downarrow})^2] \tag{II .24}$$

and side jump scattering

$$\tilde{\sigma}_{xy}^{SJ} = -e^2 N_\uparrow \frac{2\delta^{\uparrow} v_F^{\uparrow}}{3} + e^2 N_\downarrow \frac{2\delta^{\downarrow} v_F^{\downarrow}}{3} \tag{II .25}$$

from a true ab-initio scenario. Herein, $N_{\uparrow,\downarrow}$ denotes the density of states, $v_F^{\downarrow,\uparrow}$ the Fermi velocity, λ denotes a measure of the degree of spin-orbit coupling (i.e. λ^2) and corresponds to the Compton wavelength $\lambda_C = \frac{\hbar}{mc}$ in the case of free electrons. L. Berger [64, 70] has shown that λ^2 obeys a renormalization by band structure effects involving a factor $\nu \approx 10^4$, which relates the Compton wavelength and spin-orbit coupling as $\lambda^2 k_F/4 \approx \nu \lambda_C k_F/4 = \delta$ and gives a lateral displacement $\delta \approx 10^{-11}$ m per individual side jump event. $\langle V^n \rangle_C = \int P(V) V^n dV$ defines the distribution sum of the potential V and

probability distribution $P(V)$ in each cell of volume $\Omega_0 = a^3$. Accordingly, one obtains an expression for the Hall-angle for spin s from a first principles calculation

$$\Phi_{aH}^{S} \approx S\left[\frac{2\delta^{S}}{l^{S}} + \frac{\pi m^2 \lambda^2}{6\hbar^2}\frac{\langle V^3\rangle_c}{\langle V^2\rangle_c} N_S \Omega_0 (v_F^S)^2\right], \qquad \text{(II .26)}$$

wherein δ^S stands spin-dependent lateral displacement and $l^S = v_F^S \tau_F^S$ is the spin-dependent electron mean free path. Equation II .26 combines both effects, side-jump and skew-scattering mechanism. In the case of impurity scattering one gains insight into the interdependence of the skew scattering vs. side jump mechanism and disorder. In the weak-disorder limit or equivalently, in a stoichiometrically and crystallographically well ordered ferromagnetic system the magnitude of the Hall angle is reported to dominate over skew scattering by approximately one order of magnitude as shown in Reference [67], which is consistent with experimental results [15]. With increasing disorder, the mean free path l decreases significantly as does δ and equation II .26 does not yield a safe prediction of the dominating effect.

The anomalous Hall effect in general remains a rather controversial topic and the debate continues as to whether AHE is caused entirely by extrinsic scattering effects such as skew scattering or side jump scattering as described above or whether there is an intrinsic contribution due to the electronic band structure [71]. However, a unified theory satisfyingly describing both, extrinsic and intrinsic nature of AHE has not been reported so far. The intrinsic character of AHE in ferromagnets has first been devised as early as 1954 by Karplus and Luttinger [63] and takes into account the band structure and spin-orbit interaction of ferromagnets. Ab-initio band structure calculations are desired especially for the $L1_0$-phased class of materials such as the type of

FePd and FePt dealt with in this thesis, to further investigate and clarify the ongoing controversy over the intrinsic character of AHE. The introduction of disorder in $L1_0$-FePt and -FePd should then give a more reliable insight with respect to the interplay between extrinsic and intrinsic effects in AHE.

Chapter III

Experimental Methods

In the following chapter a short description of the experimental methods and techniques that were applied in order to fabricate $L1_0$-ordered thin films of the binary alloys FePt and FePd will be given. There will also be a short introduction to the methods utilized with regards to the characterization of the magnetic, crystallographic and electron transport properties of $L1_0$-ordered FePt thin films.

III .1 Magnetron sputtering

Over the past 20 years sputtering and sputtering processes have evolved into one of the most important techniques to deposit films of metals, alloys and various other compounds in high vaccuum. Typically, the target — a plate of the material to be deposited — is connected to a negative voltage supply dc or rf, while the substrate faces the target. The sample holder may be grounded or biased and in terms of temperature, which is often an important process parameter, heated or cooled respectively [72, 73]. A sputtering

gas, usually argon or argon mixtures of a pressure between a few millitorr to about 100 mTorr, is introduced to ignite and maintain a glow or a plasma discharge. Argon gas and its dilute mixtures, with only few percent hydrogen for example, is chosen for the fact that it is inert, affordable at high purity grades and provides for a good momentum transfer to the target material. Additional gases, as in this case hydrogen, are introduced to perform reactive sputtering. The positive argon ions generated in a glow or plasma discharge strike the target plate and remove mainly neutral target atoms by momentum transfer, which condense on the substrate into a thin film. The most fundamental parameter of a sputtering process is the sputtering yield, which is defined as the number of atoms ejected from a target surface per incident ion. The sputtering yield increases with incident ion energy and with ion mass, which dominate the deposition rate of sputtered films. At 500 eV incident argon ion energy the sputtering yield of Fe is 1.10, of Co it is 1.22 and of Pt 1.40 and of Pd 2.08 [74]. The sputtering yield depends on the energy of the incident ion, the target material binding energy and the atomic masses of the incident ion and the material of the target.

Magnetron sputter sources are diode sputtering sources utilizing magnetic electron traps to increase the ionization efficiency of the primary electrons. The active part of a typical magnetron sputter head is depicted in figure III .1 [1]. Magnetic fields in conjunction with the electric field at the cathode surface cause the $\overrightarrow{E} \times \overrightarrow{B}$ electron drift currents to close on themselves and therefore be confined to the immediate vicinity of the cathode, where the target is located. Primary electrons are injected into such traps by the electric field in the cathode dark space and can escape only by participating in

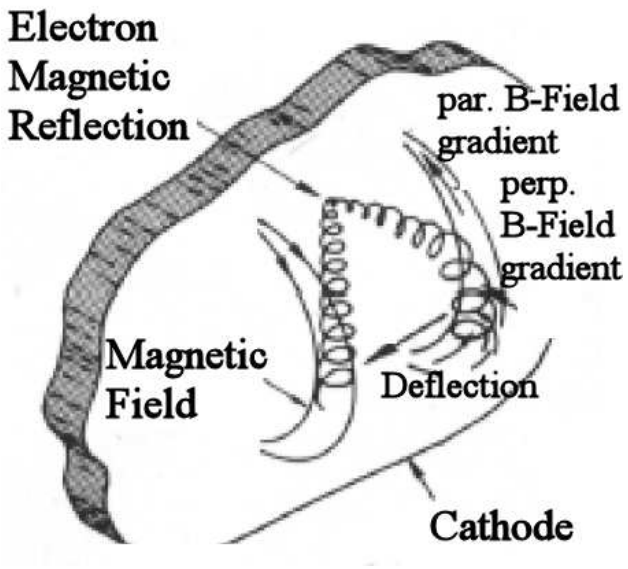

Figure III .1: Schematic of a part of a target surface in a magnetron sputter head as used to fabricate magnetic thin films on monocrystalline MgO(001) substrates [1].

energy exchange process required to sustain the discharge. Thus, the ionization process of the argon sputter gas is highly efficient and high currents and sputtering rates can be achieved at moderate and near constant voltages even at low argon gas pressures. Positive argon ions collide with the atoms of the target plate and transfer their kinetic energy. If this energy exceeds the binding energy, primary recoil atoms are generated and a collision cascade is launched. Sputtering of a surface atom takes place once the energy transferred normal to the surface is larger than the sublimation energy, which is about 3 times the surface binding energy. Apart from sputtering, the second most important process is the emission of secondary electrons from the target surface, which enable the glow discharge to be sustained.

The samples studied in this thesis were prepared by high vacuum magnetron-sputter deposition on polished MgO(001) substrates. Magnetron-sputtering a widely used vacuum deposition method for thin films, which utilizes the combination of an electric and a magnetic field perpendicular to each other that confines secondary electrons emitted from the target material after collision processes of ionized argon, the sputter gas, with the sputter target, the cathode. The electrons follow helical paths around the magnetic field lines and therefore undergo more ionizing collisions with neutral argon gas near the target than would otherwise occur. This enhances the ionization of the plasma near the target leading to a higher sputter rate and has the plasma can be sustained at a lower pressure. The sputtered atoms, which are emitted from the target solid by a momentum cascade, are neutrally charged and so are unaffected by the magnetic trap[73, 75]. A 4%-hydrogen-argon sputter gas mixture was used to prevent film oxidation during growth at high temperatures. The FePt and FePd magnetic thin films of a typical thickness of $\approx$ 30 nm were sputtered by co-deposition directly onto the substrates at a substrate temperature of 1000 K and at a deposition rate of $0.1 - 0.2$ $\text{Å}\text{s}^{-1}$. The typical direct-current power applied to the Fe magnetron sputter head lies at $P_{\text{Fe-M}} = 15$ W and for the Pt or Pd magnetron sputter head $P_{\text{Pt,Pd-M}} = 5 - 6$ W. Both, the magnetron sputter head for magnetic target material (Fe) and for the non-magnetic target material (Pd,Pt) are directed facing towards one substrate, i.e. are geometrically angled, and were run simultaneously with the MgO(001) substrate heated and stabilized to $T = 700$ °C. A thorough pre-sputtering for 10 min at a power of 50 Watts was performed prior to starting the actual deposition process. Both co-deposition

magnetron sputter heads were ignited at a 4%-hydrogen-in-argon gas flow of 50-75 sccm, and the shutters of both heads were opened simultaneously for $t = 750$ s, which yielded a overall film thickness of a desired thickness of ≈ 30 nm.

III .2 Vibrating sample magnetometry

The vibrating sample magnetometer was first described by Foner [76] in 1959. The VSM measures the difference in magnetic induction with and without the specimen and therefore gives a direct measure of the magnetization. A schematic of the experimental set-up is shown in figure III .2. The detected ac signal of fixed frequency is measured using a lock-in amplifier [77, 78]. The sample is oscillated vertically in a region of uniform field. Often, the sample is driven by a loudspeaker mechanism, the oscillating frequency is approximately 55 Hz and the amplitude is 0.1-0.2 mm. The great advantage of the VSM compared to other techniques to determine hysteretic loops of the magnetization of a sample like magneto-optical Kerr effect lies in its ease of operation at magnetic fields up to $B = 9$ T and in the convenience for measurements far below room temperature down to $T = 4.2$ K. The sample is mounted on a non-magnetic stick in the out-of-plane geometry and centered inbetween two induction coils by a measurement of magnetic moment vs. position inbetween both induction coils, i.e. the z-position. The z-position yielding the highest magnetic moment is chosen to measure the 5-arm hysteretic loop of the sample by sweeping the applied field by 2 Tesla into positive and negative direction. The magnetic moment is measured by two induction coils, between which the sample is vibrated at a frequency of

$f = 55$ Hz. At the same frequency an AC lock-in is operated to extract the magnetic moment measured while the applied field is ramped at a field ramp rate of 0.5 T/min. The data density measured per hysteretic arm comprised usually 200 data points with the AC lock-in sensitivity set to 200 μV and a lock-in time constant of 300 msec. Sample temperatures ranged in the interval $50 \leq T \leq 280$ K and were held constant using a temperature controlled liquid helium bath flow cryostat. Contrary to magnetotransport measurements, temperatures below $T = 50$ K were not accessible by VSM since paramagnetic impurities in the monocrystalline MgO(100) substrate contributed a large artefact signal and thus making quantitative data analysis impossible.

III .3 X-ray diffraction

The method of choice to determine the degree of chemical ordering of the $L1_0$ -materials presented in this work is x-ray diffractometry. Standard $\theta - 2\theta$ scans have been performed on the epitaxial thin films by aligning the diffractometer on the MgO(001) substrate peak $2\theta = 42.91°$. The watercooled x-ray tube delivers a Cu-K_α radiation of wavelength $\lambda = 1.54$ Å, which enables constructive interference of radiation reflected from adjacent lattice planes with Miller indices $\{hkl\}$ within the ordered film according to Bragg's law [51, 79]

$$2d_{hkl} \sin\theta = n\lambda \qquad \text{(III .1)}$$

An alternative expression describing the condition for constructive diffraction of x-rays can be deducted from the scattering amplitudes obtained by a

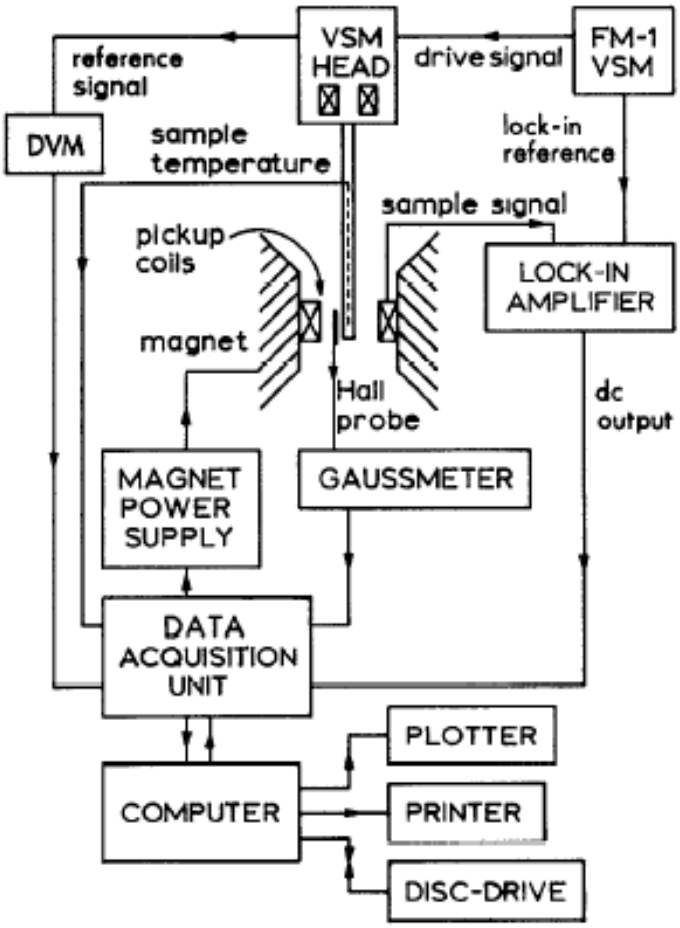

Figure III .2: Experimental setup of a vibrating sample magnetometer [2].

Fourier transformation of the periodic lattice

$$2\overrightarrow{k} \cdot \overrightarrow{G} = G^2, \qquad \text{(III .2)}$$

where $\overrightarrow{G}$ are reciprocal lattice vectors and $\overrightarrow{k}$ is an incident scattering vector.

All x-ray experiments were performed in the Bragg-Brentano-geometry as depicted in figure III .4. One measures the scattered intensity $I(2\theta)$ as a function of the varying incidence angle of the incoming x-ray beam, which is the angle between specimen surface and incoming beam axis. In the present

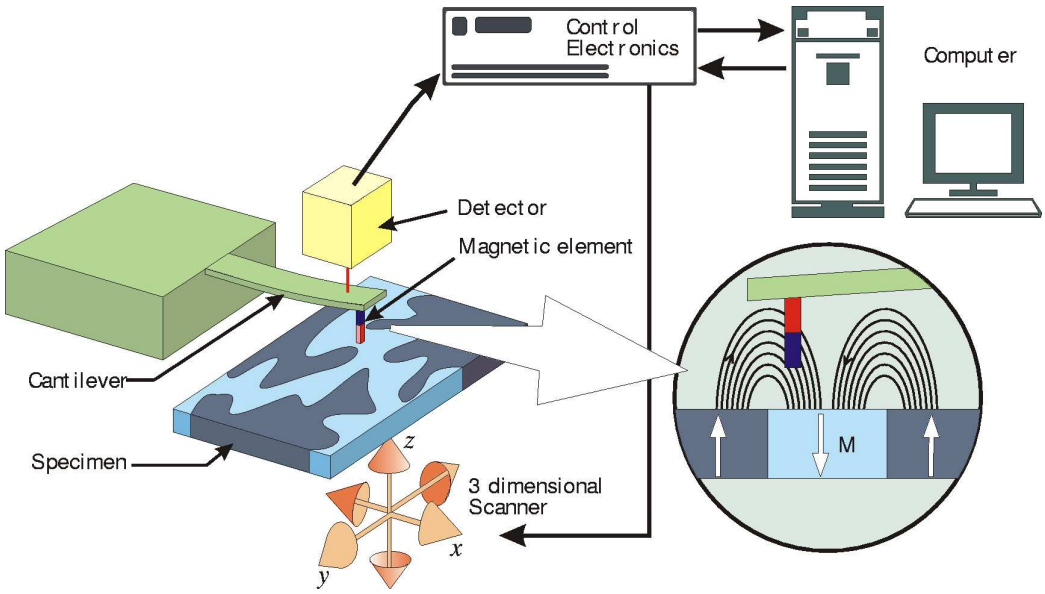

Figure III .3: Schematic of a magnetic force microscope [3].

case, no apertures for incoming and outgoing beam, denoted DS and AS were used. The diffractometer was aligned to the (100)-peak of the single-crystalline MgO substrate at $2\theta = 42.93°$, i.e. the angle 2θ set to 42.93° and the sample angle θ swept in $(\frac{42.93}{2} \pm 1)°$. The maximum of this alignment scan is set to $\theta = 0°$ and the x-ray diffraction spectrum collected in $(20 \leq 2\theta \leq 51)°$. A typical count time of 5 seconds per 0.01° in 2θ has been employed to obtain reliable $\theta - 2\theta$-scans for quantitative analysis of the chemical long range ordering within the magnetic thin film of a representative thickness of ≈ 30 nm.

The chemical ordering of a magnetron sputtered thin film can be determined by analyzing the occupation of each lattice site by an atom A (e.g. Fe) and B (e.g. Pt) in the face-centered tetragonal (fct) cell of a $L1_0$ -phase material. An entirely empirical expression for the chemical order parameter

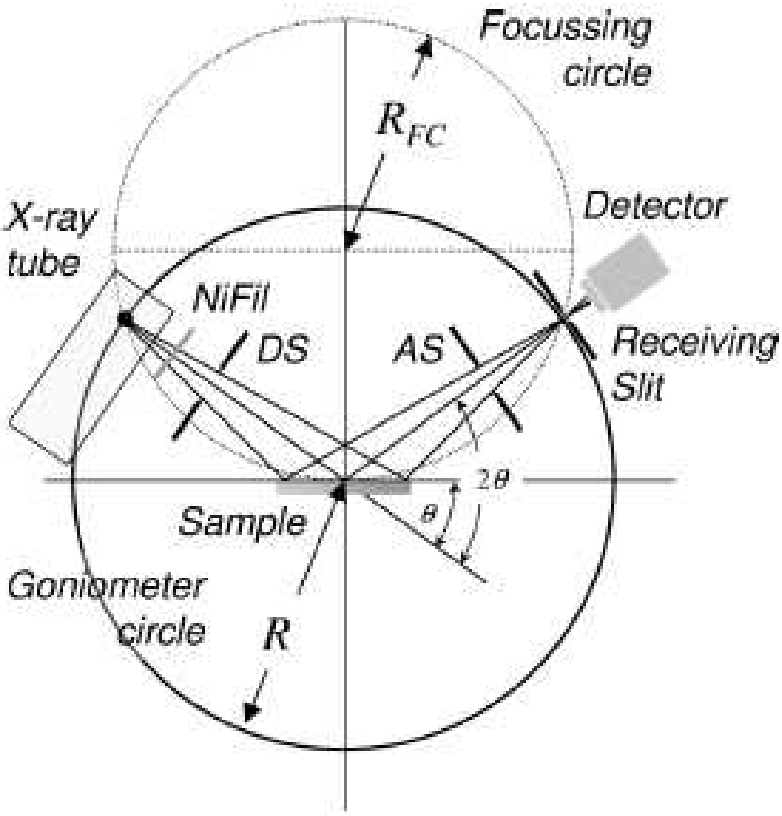

Figure III .4: Measurement principle of a $\theta-2\theta$-geometry for x-ray diffraction in the Bragg-Brentano geometry [4].

of a crystalline binary alloy is

$$S = r_\alpha + r_\beta - 1 = \frac{(r_\alpha - x_A)}{y_\beta} = \frac{(r_\beta - x_B)}{y_\alpha}. \qquad \text{(III .3)}$$

Herein are x_A and x_B the atom fractions of the two components, y_α and y_β are the fractions of the lattice site types α and β in the ordered structure, and r_α and r_β are the fractions of each type of lattice site occupied by the correct types of atoms, A on α and B on β [79, 80, 81]. For a perfectly ordered film $r_\alpha = 1$, $r_\beta = 1$, i.e. $S = 1$, while $S = 0$ means total disorder within the material.

More practically however, S is determined from integrated intensities and the positions of the (001)-peak and the (002)-peak obtained from $\theta - 2\theta$ scans. To compute the chemical order parameter S $(0 \leq S \leq 1)$ one has to relate the integrated intensities $\int I_{(001)}(\theta) \cdot d\theta$ and $\int I_{(002)}(\theta) \cdot d\theta$ as well as positions of the (001)-peak and the (002)-peak according to [79]

$$\begin{aligned} S^2 = \frac{\int I_{(001)}(\theta) \cdot d\theta}{\int I_{(002)}(\theta) \cdot d\theta} \cdot \frac{\frac{1+cos^2(2\theta_{(002)})}{2sin(2\theta_{(002)})}}{\frac{1+cos^2(2\theta_{(001)})}{2sin(2\theta_{(001)})}} \cdot \\ \cdot \frac{(4\sum_{i=1}^{4} a_i^{Fe} e^{-b_i^{Fe} sin^2(\theta_{(002)})/\lambda^2} + c^{Fe}) \cdot e^{-(B_0^{Fe} + B_{293}^{Fe}) sin(\theta_{(002)})/\lambda^2}}{(\sum_{i=1}^{4} a_i^{Fe} e^{-b_i^{Fe} sin^2(\theta_{(001)})/\lambda^2} + c^{Fe}) \cdot e^{-(B_0^{Fe} + B_{293}^{Fe}) sin(\theta_{(001)})/\lambda^2}} \cdot \\ \cdot \frac{(\sum_{i=1}^{4} a_i^{Pt} e^{-b_i^{Pt} sin^2(\theta_{(002)})/\lambda^2} + c^{Pt}) \cdot e^{-(B_0^{Pt} + B_{293}^{Pt}) sin(\theta_{(002)})/\lambda^2} + \ldots}{(\sum_{i=1}^{4} a_i^{Pt} e^{-b_i^{Pt} sin^2(\theta_{(001)})/\lambda^2} + c^{Pt}) \cdot e^{-(B_0^{Pt} + B_{293}^{Pt}) sin(\theta_{(001)})/\lambda^2} + \ldots} \\ \frac{\ldots + (\Delta_{(002)}^{Fe} \cdot e^{(-B_0^{Fe} + B_{293}^{Fe}) sin^2(\theta_{(002)})/\lambda^2)^2} + (\Delta_{(002)}^{Pt} \cdot e^{(-B_0^{Pt} + B_{293}^{Pt}) sin^2(\theta_{(002)})/\lambda^2)^2}}{\ldots + (\Delta_{(001)}^{Fe} \cdot e^{(-B_0^{Fe} + B_{293}^{Fe}) sin^2(\theta_{(001)})/\lambda^2)^2} + (\Delta_{(001)}^{Pt} \cdot e^{(-B_0^{Pt} + B_{293}^{Pt}) sin^2(\theta_{(001)})/\lambda^2)^2}}, \end{aligned} \qquad \text{(III .4)}$$

where a_i, b_i, c are the coefficients for the analytical approximation of the scattering factors for Pd and Fe [80] and B_0, B_{293} are the Debye parameters for Pd and Fe [81].

It is critical to know the precise film thickness of the deposited magnetic material in order to perform a quantitative data analysis, especially with respect to magnetotransport, as will follow later. X-ray reflectometry has been employed to determine the film thickness of the magnetron-sputter deposited $L1_0$-material. This method is based on the constructive and destructive interference of x-rays representing electromagnetic radiation, that is reflected from the top surface and the bottom interface of the film causing a typical intensity modulation as depicted in figure III .5 (a). This low-angle $\theta - 2\theta$ scan was taken in the interval $(1 \leq 2\theta \leq 5)^\circ$ with the sample aligned to $\theta = 1^\circ$ using a count time of 5 seconds per 0.01° in 2θ. To obtain intensity maxima, the path difference between reflected waves has to be an integral multiple $n + 1$ of the incident wave of wavelength λ and needs to satisfy the equation

$$(n + 1) \cdot \lambda = 2t\sqrt{\sin^2 \theta_{n+1} - \sin^2 \theta_n}, \qquad \text{(III .5)}$$

wherein θ_n denotes the critical angle of incidence for total reflection of x-rays at an interface, θ_{n+1} stands for the angle positions of the interference maxima, i.e. the Kiessig fringes, and t is the desired film thickness. Equation III .5 simplifies for small angles of incidence valid in x-ray reflectometry experiments as performed in this work to

$$\sin^2 \theta_{n+1} - \sin^2 \theta_n = (n + 1)^2 \frac{\lambda^2}{(4t)^2}, \qquad \text{(III .6)}$$

which allows for the extraction of the film thickness t from the slope of a plot of the right-hand-side versus left-hand-side of equation III .6 as shown in figure III .5 (b), wherein the red line represents a least-square fit ('Kiessig fit') to the data (circles) [82].

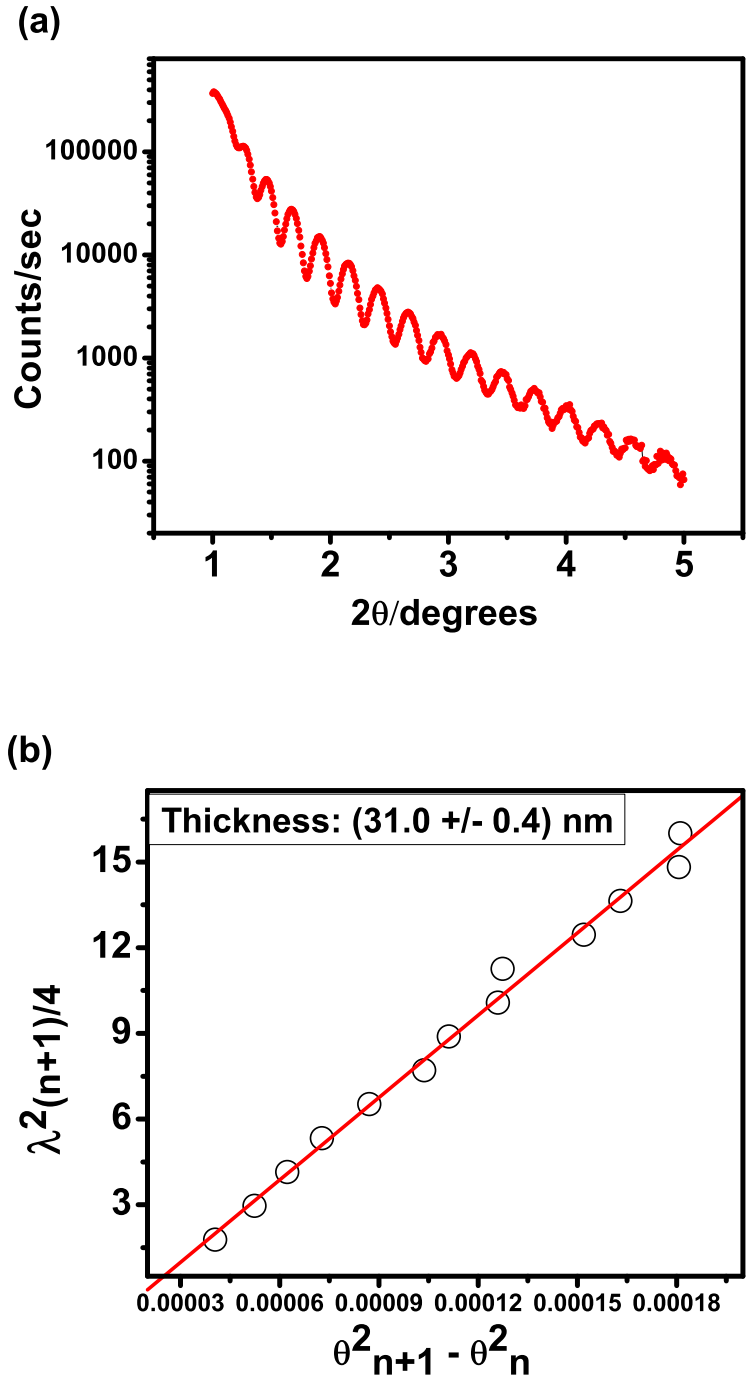

Figure III .5: X-ray reflectometry measurement (a) and Kiessig fit (b) to determine the film thickness of an epitaxial $L1_0$-FePt film.

III .4 Magnetic force microscopy

The magnetic force microscope (MFM) belongs to the family of scanning probe microscopes and is a variant of the atomic force microscope (AFM). A small ferromagnetic tip of a radius in the 10 nm range magnetized perpendicular to the tip axis is employed to record magnetostatic forces or force gradients of a magnetic sample [83]. Usually a CoCr deposited microetched Si tip serves as the nanoprobe for high resolution magnetic force microscopy. As in most force microscope techniques, the magnetostatic forces proportional to local field gradients are detected by the deflection of a flexible cantilever that carries the magnetized tip at its end while scanning over the surface of the specimen twice (figure III .3). First the surface profile is recorded by intermittently (tapping mode, trademarked by Veeco Instruments) measuring repulsive forces, then in a second retraced run the force gradients or forces are recorded at an adjustable distance above the previously measured topographic profile (lift mode). This distance usually ranges from 20 to 40 nm. Thus, the magnetic information is obtained by the subtraction of surface features from the total image recorded in the lift mode.

Three contrast mechanisms are identified in magnetic force microscopy, namely charge contrast, susceptibility contrast and hysteresis contrast. In the case of charge contrast, there is negligible interaction between tip and sample, i.e. neither the sample is modified by the probe nor the probe is modified by the sample. This condition leads to convincing domain images even from soft magnetic materials if weak, magnetically hard tips and a large tip sample separation are used. More specifically, MFM images are more closely related to the charge pattern related to magnetization or a stray field component

or the absolute value of the stray field and depict the interactions with the magnetic charges in the sample, as can be seen in

$$E_{interaction} = -\int_{surface} \lambda_{sample}\Phi_{tip}dV - \int_{surface} \sigma_{sample}\Phi_{tip}dS, \qquad \text{(III .7)}$$

wherein $\lambda_{sample} = -div\,\overrightarrow{J}_{sample}$ is the volume charge, $\sigma_{sample} = n \cdot \overrightarrow{J}_{sample}$ is the surface charge of the sample, while Φ_{tip} is the scalar potential of the probe stray field originating from $\overrightarrow{H}_{tip} = -grad\Phi_{tip}$. The force is obtained from equation III .7 by replacing Φ_{tip} by $d\Phi_{tip}/dz$ or the second derivative of Φ_{tip} in the presence of force gradients. Susceptibility contrast is a result of the influence of the sample magnetization by the probe stray field or vice versa, which is the case if soft magnetic tips are used to probe hard magnetic material. Neither the probe potentials nor the sample charges can always be considered rigid. Images that are influenced by irreversible magnetization processes are classified as hysteresis images. In this case, the stray field of the probe is too strong and irreversible reactions in the sample magnetization are observed. This can even lead to the unpinning of domain walls by the probe during the scanning process and is to be avoided, but limits sensitivity and lateral resolution at the same time.

The magnetic domain structure of $L1_0$-alloys investigated in this thesis was imaged by tapping-mode magnetic force microscopy (MFM) [84, 85] at room temperature and in zero field by employing the charge contrast mechanism. The tapping mode cantilevers had a resonant frequency of 65 kHz and a spring constant of 1-5 N/m. The CoCr-coated Si tip was vertically magnetized prior to imaging using a permanent magnet. The resonant frequency of the mounted tip was determined individually and as a operating frequency for scanning the surface in the tapping mode, a frequency 0.5-2 kHz below the

resonant frequency of respective tip was chosen. After approaching the tip to the sample surface, scanning operation was started with an initial scan width of typically 10 μm and a scan rate of $0.5-1$ Hz, i.e. $0.5-1$ full scan lengths per second. For optimal contrast the tip-surface distance was kept constant at 20 to 25 nm. Upon obtaining a clear domain image at a scan width of 10 μm the scan width was successively reduced down to a value of typically 3 μm. The average magnetic domain width of the demagnetized state was obtained by a power-spectrum analysis. The zero-field demagnetized domain state of each $L1_0$-thin film was obtained applying an alternating magnetic field of decreasing amplitude starting at 3 Tesla and sweeping this field alternatingly to zero field over many hundreds of cycles with asymptotically decreasing field amplitude. The VSM was used for this procedure.

III .5 X-ray magnetic circular dichroic photo-excitation electron microscopy - XMCD-PEEM

A method with the capability of imaging magnetic contrast based on the excitation of photoelectrons via circular polarized x-ray photons is presented in XMCD-PEEM. The x-ray magnetic circular dichroic effect (XMCD) is based on the photo-excitation process of secondary electrons by high energetic photons as shown in figure III .6. Here, a core level electron is excited initially III .6 (a), which is followed by the emission of an Auger electron III .6 (b) in combination with a non-radiative core hole decay. Consequently a cascade of secondary electrons is triggered in inelastic momentum transfer

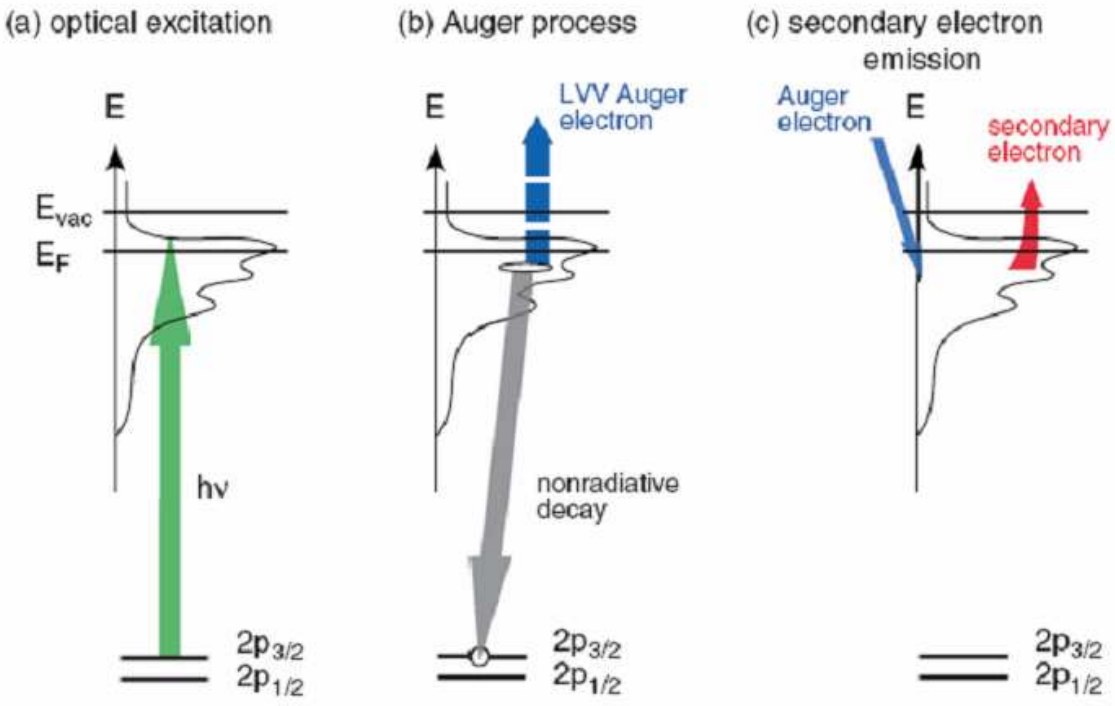

Figure III .6: (a) Excitation of a core level electron, (b) excitation of an Auger electron and (c) excitation of a secondary electron cascade as a consequence of an Auger process [5].

processes III .6 (c), which are utilized to build up an electron microscope image, once their kinetic energy is sufficient to overcome the work function of the respective material.

In the presence of circularly polarized x-ray photons as an excitation source one is able to address the Stoner exchange-split minority and majority electron density of states from the $2p_{3/2}$ and $2p_{1/2}$ core electron states separately as depicted in figure III .7 (a) due to quantum selection rules. In the case of samples containing $3d$ transition metals such as Fe, one tunes

the excitation x-ray photon energy to match the $L_{2,3}$ absorption edge which involves the spin-orbit split $2p_{3/2}$ and $2p_{1/2}$. For elemental Fe, this L_3 - absorption edge lies at $E_{L3} \approx 707$ eV. Consequently, photo-excitation into the unoccupied electron density of states (DOS) of the incompletely filled d-shell of the transition metal results in a strong spectral feature, which in turn provides for a good material contrast once the helicity of the x-ray photon is flipped. The Auger electron excitation process via a non-radiative core hole decay III .7 (b) and the consequent secondary electron cascade III .7 (c) is analog to the photo-excitation process described in the case of non-circularly polarized x-ray photons.

In the case of circular polarized light, the dependence of the photo-excited electron intensity I on incident x-ray photon helicity $\overrightarrow{\zeta}$ and the direction of magnetization $\overrightarrow{M}$ is termed magnetic circular dichroism

$$I = I(\overrightarrow{M}, \overrightarrow{\zeta}). \tag{III .8}$$

The strong exchange interaction in ferromagnets leads to spin-split valence states, i.e. more empty minority states than empty majority states are available above the Fermi energy level. This essentially causes the electron polarization $\overrightarrow{P}$ to be anti-parallel for $L + S$ spin-orbit coupling compared to $L - S$ spin-orbit coupling

$$\overrightarrow{P}(2p_{3/2}) = -k \cdot \overrightarrow{P}(2p_{1/2}) \tag{III .9}$$

in the $2p$ core levels, see figure III .7. The electron polarization $\overrightarrow{P}$ is anti-parallel for opposite helicity of the incident x-ray photons,

$$\overrightarrow{P}(\overrightarrow{\zeta}) = -\overrightarrow{P}(-\overrightarrow{\zeta}). \tag{III .10}$$

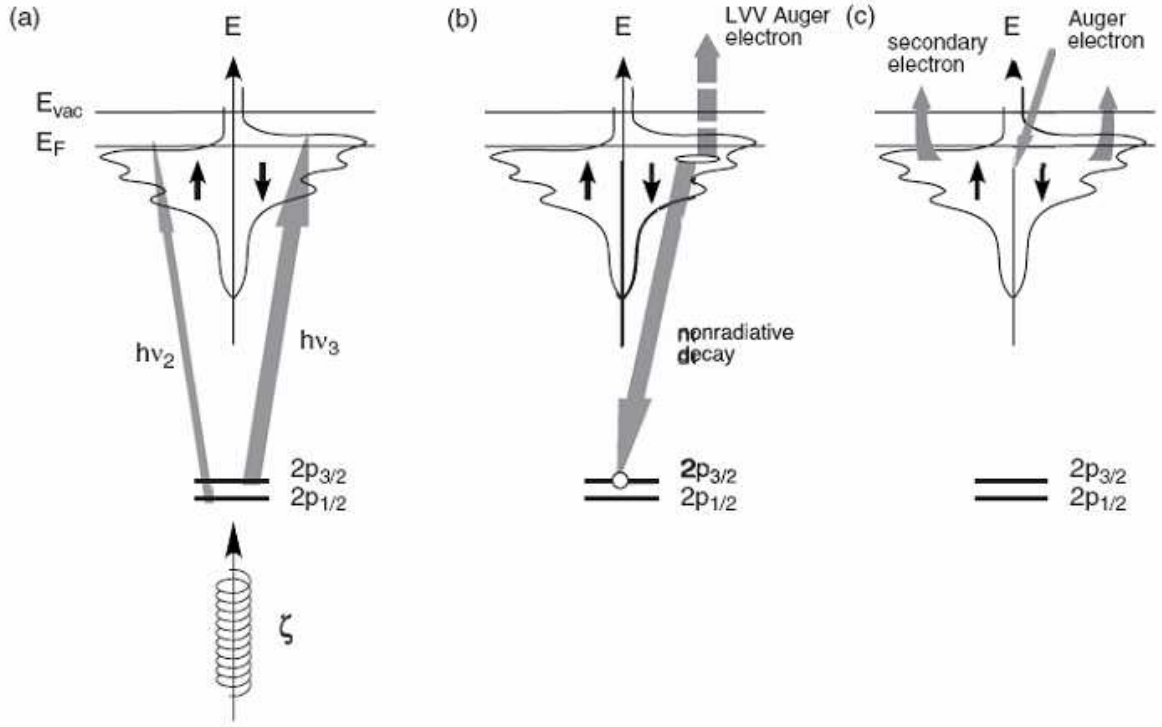

Figure III .7: Photo-excitation of electron in an $L_{2,3}$ absorption process of a circular polarized x-ray photon, (b) decay into a core hole by Auger electron emission and (c) emission of a secondary electron cascade by decay of an Auger electron[5].

Photo-excited secondary electrons are collected and collimated in a photo-electron emission microscope (PEEM) as schematically shown in figure III .8. Secondary electrons pass through a contrast aperture that bears a potential of several tens of kilovolts. Electrostatic stigmators and a field aperture form a first image and a second image after passing through a projective lenses. Finally, the imaged secondary electrons are focussed onto a multi-channel plate combined with scintillator crystal, often a Yttrium-Aluminium-Garnet (YAG) system, delivering the actual secondary electron map of the sample surface. This is an image conversion that transforms the initial 'electron'-image into a 'photon'-image which is realized outside the vacuum chamber by a CCD-camera system.

XMCD-PEEM is performed at a synchrotron facility which delivers a x-ray beam of high brilliance and at the same time provides for a circular polarization that can be flipped into the opposite direction, as outlined above, and tunable energy. The circular polarization is achieved by a so called undulator that causes the accelerated electrons of the synchrotron to deviate on a wave-like trajectory giving rise to the emission of circular polarized x-ray photons. The polarization of emitted x-ray photons is flipped in helicity $\overrightarrow{\zeta}$ by reverting the source electron trajectory via anti-tuning the electron undulator.

A lateral resolution in the range of 10-20 nm employing the PEEM-optics described above is considered achievable limited by diffraction at the contrast aperture. A lateral resolution of 50 nm is more reasonable and has its limits also in sample topography features such as crystalline facets, terrace edges, monatomic steps and similar surface defects, which give rise to electrostatic

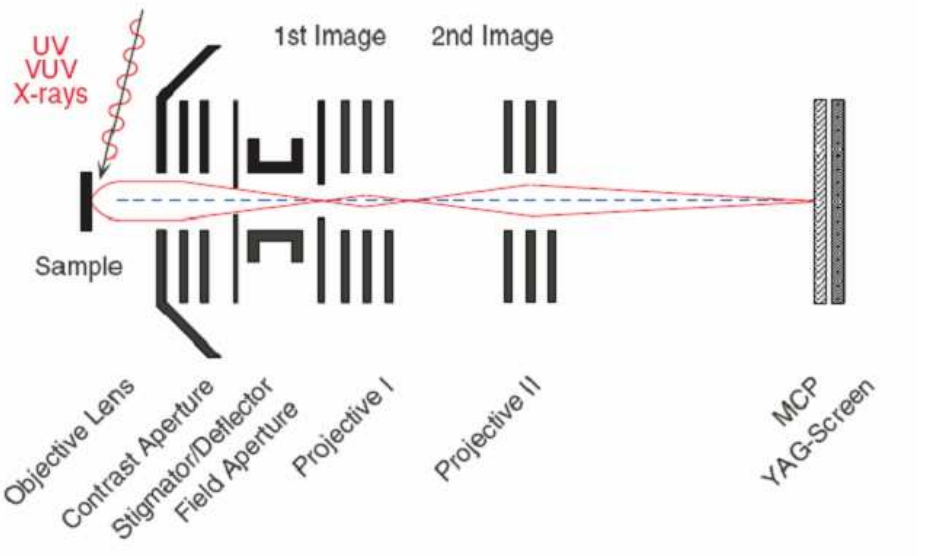

Figure III .8: Schematic of an electron emission microscope based on the photoexcitation effect[5].

microfields influencing the trajectories of the secondary electrons emitted. This in turn causes a distortion of the image and hence limits lateral resolution in XMCD-PEEM.

III .6 Diffusive electron transport - Domain wall resistance and Hall measurements

Electron transport studies have been performed in order to understand the resistance due to magnetic domain walls (DWR) in particular narrow Bloch domain walls of a width of approximately 10 nm inherent to epitaxial $L1_0$-ordered FePt and its isoelectronic relative $L1_0$-FePd. The second effect that has been studied in detail by electron transport experiments is the anomalous

Hall effect also known as the anomalous or spontaneous Hall effect (AHE). Both effects are very similar so assess quantitatively, DWR in longitudinal resistance measurements with field normal to the $x-y$-plane of the sample, i.e. in z-direction. AHE is accessed as a transverse resistance measurement with field applied in z-direction. In both cases, the resistance is measured in a 4-probe method sourcing a constant current between 1 μA up to 1 mA and simultaneously measuring the voltage drop of the sample within this current path using two separate voltage probes or contacts while sweeping a magnetic field normal to the $x-y$-plane of the sample. DWR as well as AHE experiments are performed in the variable temperature insert (VTI) of a liquid He bath flow cryostat with superconducting magnet in order to study the temperature dependence of both physical effects.

III .6.1 Measurement principle of resistance due to magnetic domain walls - DWR

The resistance contributions due to magnetic domain walls range between a couple of tenths of percent to a couple of percent in the best cases of the ordinary resistivity of a metal [86, 14, 87, 88] based on the interplay between impurity and thermal electron scattering mechanisms. This makes four-probe measurement techniques essential to safely isolate DWR from secondary resistance contributions like contact resistance as in the case of two-point resistance measurements. Four-probe resistance measurements can be performed on non-patterned sheet film material with four inline-pins sat onto the surface of the metallic film as shown in figure III .9. This is very advantageous whenever pristine magnetic material is to be analysed. Patterning

processes can alter intrinsic material parameters such as resistivity, crystallographic ordering or even coercivity field. Important however is in this case, that one corrects for the unconfined current path when determining the longitudinal resistivity. This is usually done using tabulated factors [89] known from sheet resistivity experiments or even electrodynamic computations of the electrostatic equipotential lines. Performing four-point measurements on specifically patterned Hall bar structures is a simple way of confining the current paths with the magnetic material. The resistivity can directly be determined from the dimensions of the bar structure and the voltage drop measured for a constant current sourced as shown in figure III .10. In four-probe resistance measurements the contact resistance between pins or wire bonds and the actual material does not play a role if a high-resistance voltmeter is used. In this case the input impedance of the Keithley 182 was > 10 GΩ.

The actual DWR measurement starts with a demagnetization procedure to create a demagnetized domain state in which the localized spins of the magnetic material are in total equilibrium leaving the magnetic structure globally without measurable moment. This is done by applying a magnetic field along the easy axis starting at $\mu_0 H = 3$ Tesla and ramping this field into the opposite direction in an alternating fashion with ever decreasing field amplitude a few hundred times until zero magnetic field is reached asymptotically. This procedure is particularly important for DWR measurements as the demagnetized and thus unperturbed domain state at zero-field yields the actual resistance contribution due to magnetic domain walls. This value is also used to further evaluate the spin-polarization of an electric direct

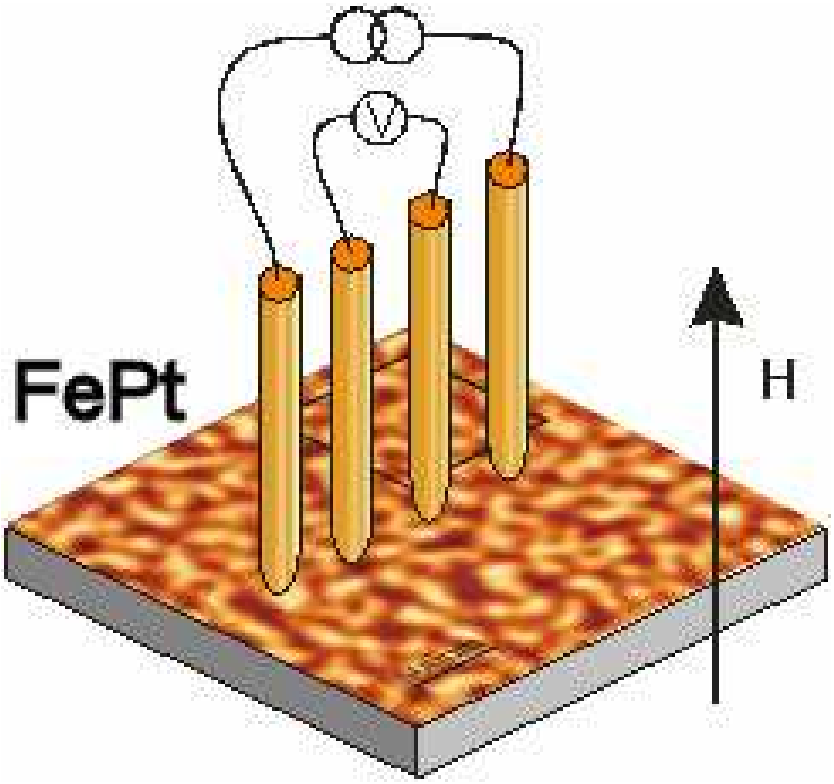

Figure III .9: Measurement principle of DWR experiments based on a non-patterned magnetic thin film (drawing courtesy of C. H. Marrows).

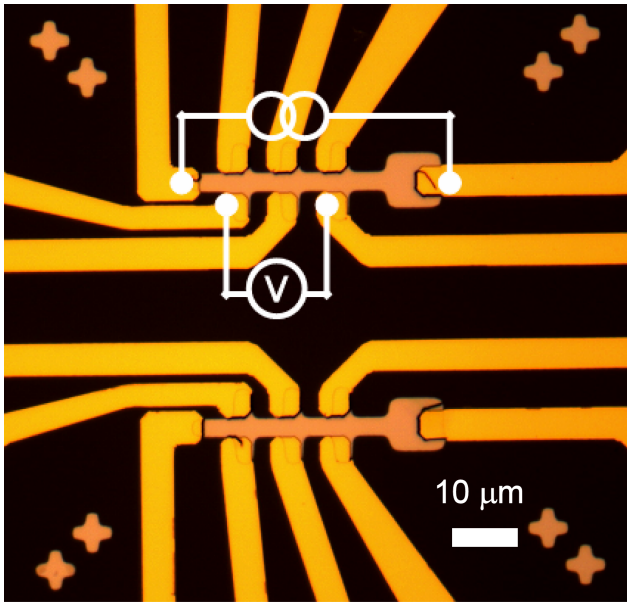

Figure III .10: Measurement principle of DWR experiments based on a patterned magnetic thin film in the form of a 5 micron wide Hall bar structure in epitaxial $L1_0$-FePt on single crystal MgO(100).

current, i.e. the current spin-polarization in the diffusive electron transport regime as described in section IV .2. The temperature dependence of DWR is measured at constant temperature starting from $T = 270$ K to $T = 4$ K in temperature intervals of 50 K to safely determine the gradual influence of electron-phonon scattering in DWR and furthermore in the current spin-polarization of a diffusive current $P(T)$. Sample temperature within the variable temperature insert of the helium gas flow cryostat is held constant at each target temperature point by a PID control unit.

III .6.2 Measurement principle of the anomalous Hall effect - AHE

The anomalous Hall effect is measured transverse to the current path. The measurement setup is identical to DWR measurements, a constant current typically ranging from 1 μA up to 1 mA is sourced along a Hall-bar structure as shown in figure III .11 while the transversal Hall voltage is measured simultaneously using a voltmeter with high input resistance. Suitable Hall-bars have dimensions ranging from a few microns up to approximately 100 microns. Au-bondwires connect the Hall-bar pattern to a chip carrier.

A magnetic field is applied perpendicular to the $x - y$-plane of the pattern starting with demagnetization as described in the case of DWR measurements above. The magnetic field is ramped along a five-arm hysteretic loop starting a zero-field gradually reaching full saturation beyond the coercive field H_c of the material, back into negative saturation and once more into the positive saturation to close the hysteretic loop. The sample demagnetization procedure is important to attain an appropriate domain state with zero

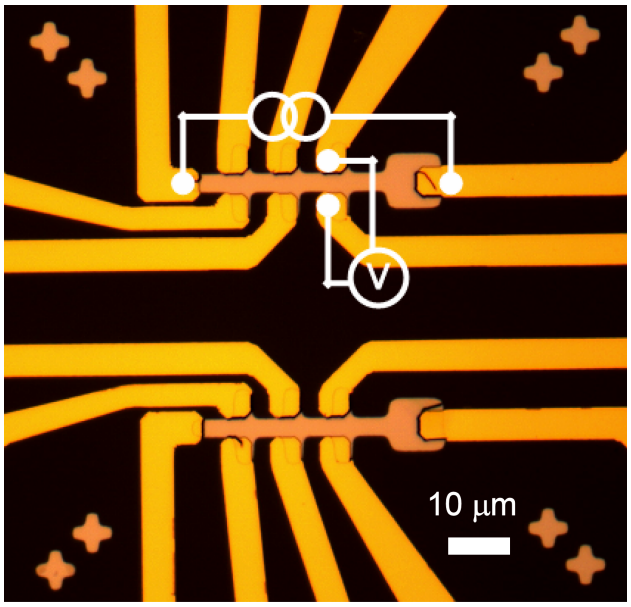

Figure III .11: Measurement principle of AHE experiments performed on a patterned Hall bar structure in epitaxial $L1_0$-FePt on single cystal MgO(100).

effective magnetization to start the AHE measurement from. Empirically, it is known from the second term in equation II .20, that AHE is proportional to the magnetization **M**, thus any possible AHE voltage offset for the demagnetized domain state at zero field points out a measurement artefact which needs to be explained and accounted for when quantifying the ordinary and anomalous Hall coefficients R_0 and R_s.

III .6.3 Fabrication of Hall bar structures

Hall bar structures of a critical dimension ranging from 5 microns to 100 microns are patterned using a dry etching process based on argon ion milling as schematically depicted in figure III .13. A patterning process has been devised specifically to avoid structuring hard masks into a titanium blanket sheet film prior to the ion milling step. Instead, a solvent removable negative tone resist with dual sensitivity to irradiation, i.e. sensitivity to ultraviolet light as facilitated in a mask aligner used for contact lithography as well as 10-30 kV electron irradiation typically employed in electron beam lithography. A negative tone resist with such properties is marketed by Microresist Technologies under the tradename maN2403 with respective developer solution maD539. Pre-cleaned $L1_0$-sheet films are spin-coated with maD2403 at 3000 rpm for 30 sec. The pre-cleaning consists of an ultrasonication step for 2 minutes in VLSI grade acetone at medium powers followed by an isopropanol bath for further 2 min. The sample surface is dried in a high purity nitrogen gas flow. The resist coating is soft-baked on a hotplate for 60 seconds at 90 degrees Celsius.

Exposure takes place in a electron beam lithography system (EBL) employing

a sequential writing process on a well-grounded sample to avoid electrostatic charging effects, see figure III .12(a). The typical exposure dose used ranges usually from 80-120 μC/cm^2. This is the patterning method of choice for micro- and nanostructures of a critical dimension of 100 nanometers to approximately 5 microns. For structures of a critical dimension ranging from 5 microns to 100 microns UV-contact-lithography using photolithography masks is employed. Illumination time at a wavelength of $\lambda = 254$ nm and an energy density of $240 - 280$ mJ/cm^2 usually ranges from 20 to 25 seconds. Electrostatic charging does not play a role in this case.

The developer solution maD539 is used regardless of the type of illumination. In general, bathing the sample in maD539 for 45 seconds is sufficient to remove all non-exposed resist. A subsequent rinse in de-ionized water fixates the resist patterns, see figure III .12(b).

The resist layer thickness of 300 nm is sufficient to serve as a mask for the argon ion milling process provided the $L1_0$-film thickness does not exceed 30 nm substantially (figure III .12(c)).

The argon-ion milling process using maN2403 as a mask is robust such that a comfortable milling time window is available in order to obtain well defined $L1_0$-patterns to a critical dimension of approximately 300 nm reproducibly. An ion current of 0.5 mA is required for a milling time of 60 sec to 3 min depending on the degree of crystallographic ordering of $L1_0$-sheet material. Argon ions of a kinetic energy of 0.6 keV transfer momentum into the $L1_0$-material by momentum cascade (figure III .13) akin to the magnetron sputter process described earlier. Material uncovered by resist is gradually removed from the solid. Different removal rates for exposed and developed maN2403

and bare $L1_0$-material give rise to a selective physical etching process, which leaves the patterned structures milled into the sheet film. The masking resist has to be removed by an ultrasonication step in VLSI grade acetone and isopropanol for 60 seconds each followed by drying in nitrogen gas flow as shown in figure III .12(d).

III .7 Ballistic electron transport - Point contact Andreev Reflection experiments

Point contact Andreev reflection (PCAR) measurements were used in order to directly probe for the ballistic current spin polarization of $L1_0$-ordered FePt [90, 54, 53, 55, 91, 92, 23]. Probing the current spin polarization of a specific material is usually carried out by PCAR experiments using a superconducting tip brought into contact with the surface of the material to be tested as schematically depicted in figure III .14. The concept of this method is based on the fact that for applied bias voltages within the gap of the superconductor, it is physically impossible to inject or extract single electrons, but only Cooper pairs. As the Andreev reflection process[56] is the coherent back reflection of a charge carrier hole into the ferromagnetic sample following the capturing of an opposite spin electron to form a Cooper pair inside the superconducting tip, one essentially probes for the number of unpaired electrons, straightforwardly giving the ballistic spin current polarization of the ferromagnet. The nature of the contact is to be considered to maintain the ballistic transport regime, i.e. the Sharvin criterion is to be maintained. Therefore the diameter of the point contact area between the surface of the

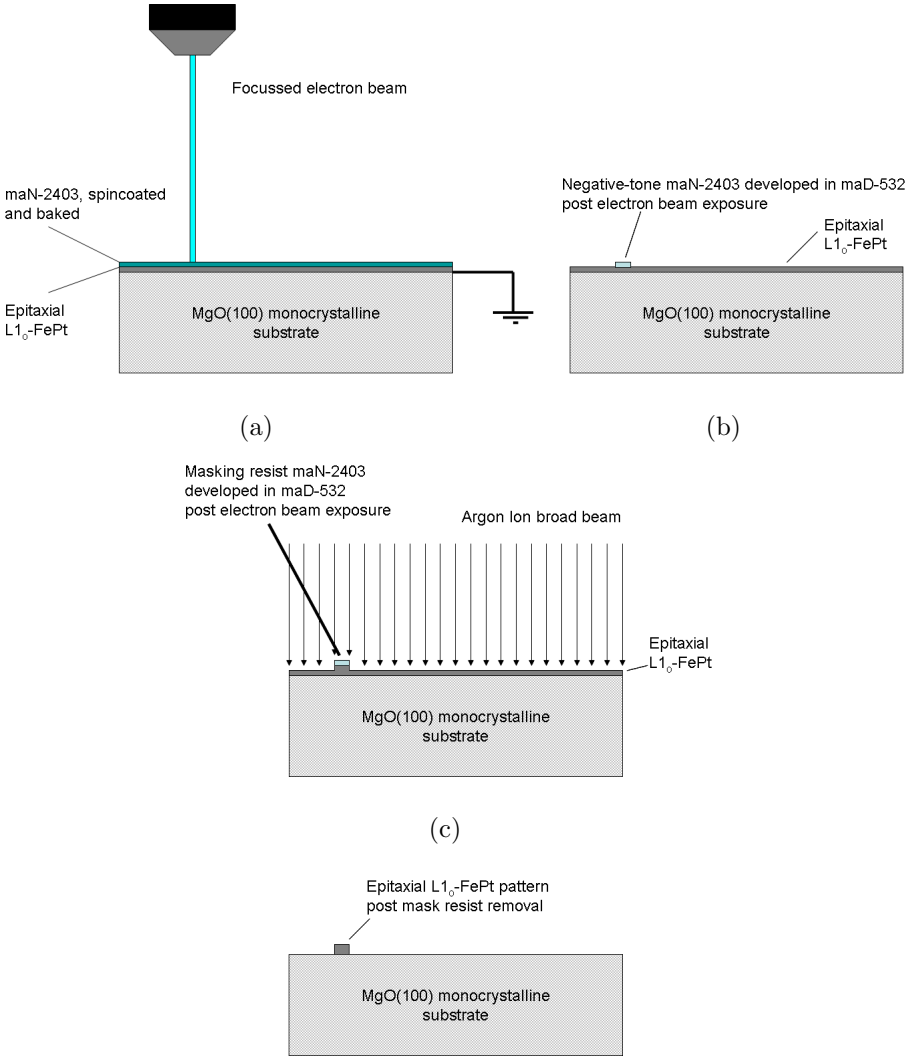

Figure III .12: Schematic of the patterning process of negative tone resist ma-N2403 by (a) electron beam lithography or ultraviolet light contact lithography and (b) treatment in developer solution ma-D539. Subsequent broad-beam argon ion milling (c) facilitates a selective physical dry etching process of the relevant sample structures out of sheet film material. A simple rinsing procedure in acetone and isopropanol (d) removes the masking resist and reveals the pattern.)

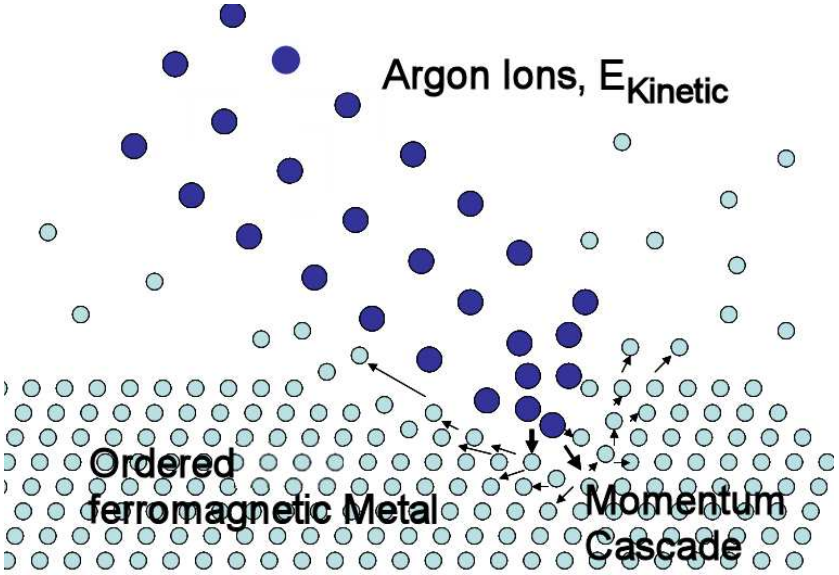

Figure III .13: Principle of the argon-ion milling process

ferromagnet and the superconducting niobium tip needs to be less than the mean free path of a conduction electron at the respective temperature, which are only a few tens of nanometers at liquid helium bath temperature. The point contact was controlled mechanically at 4.2K, in a liquid helium bath, between a superconducting niobium tip and the FePt thin film. The niobium wire of a diameter of 0.5 mm was sharpened by a slanted cut. The contact resistance reached by a sharpened tip on $L1_0$-FePt ranges from 8 Ω to approximately 15 Ω at $T = 4.2$ K. Employing the Sharvin formula this yields an effective point contact diameter of 5 nm to 15 nm [93, 94]. A bias voltage was applied across the point contact and the differential conductance was recorded via a four-probe technique. AC lock-in detection with a 0.1 mV amplitude and a 5 kHz frequency was used. A simple micrometer screw was used to press the niobium tip onto the sheet film material to reach an

ohmic and above all stable contact. Stable means, in this case, that the contact resistance measured by a dc voltmeter with a constant current of 1 mA sourced in the form of a 4-point resistance is measurement is invariant to 1-2 mΩ. The tips were repeatedly brought into contact with the sample and the dependency of the differential conductance on the sample-tip bias voltage were recorded for various contact resistances. The bias voltage was swept from typically $V = +15$ mV to $V = -15$ mV and the contact differential conductance $G(V)$ measured simultaneously using an alternating-current lock-in technique as outlined in figure III .15. The sample conductance was evaluated by measuring the voltage drop across a reference resistor $R_{\text{Reference}}$ in order to determine the current I flowing through the superconducting tip and sample. The lock-in frequency was set to the frequency of the AC-voltage sourced into the network additionally to a DC-voltage, see figure III .15. The conductance of the point contact is determined from a second AC-lock-in measurement of the voltage drop V across the point-contact. Upon reaching a stable ohmic contact between niobium tip and sheet film, the DC voltage is swept from approximately $V = +15$ mV to $V = -15$ mV and the differential conductance $G = \frac{dI}{dU}$ of the point-contact recorded simultaneously.

The direct comparison between the superconducting bandgap energy value $\Delta \approx 1.5$ eV of bulk niobium and the bias voltage necessary to induce a conductance suppression in a point contact with high interface transparency (low Z) and high spin-polarization (high P) yields a measure of goodness of the PCAR experiment. A series resistance that is non-negligible compared to the resistance value of the point contact itself e.g. by high-resistive sheet film

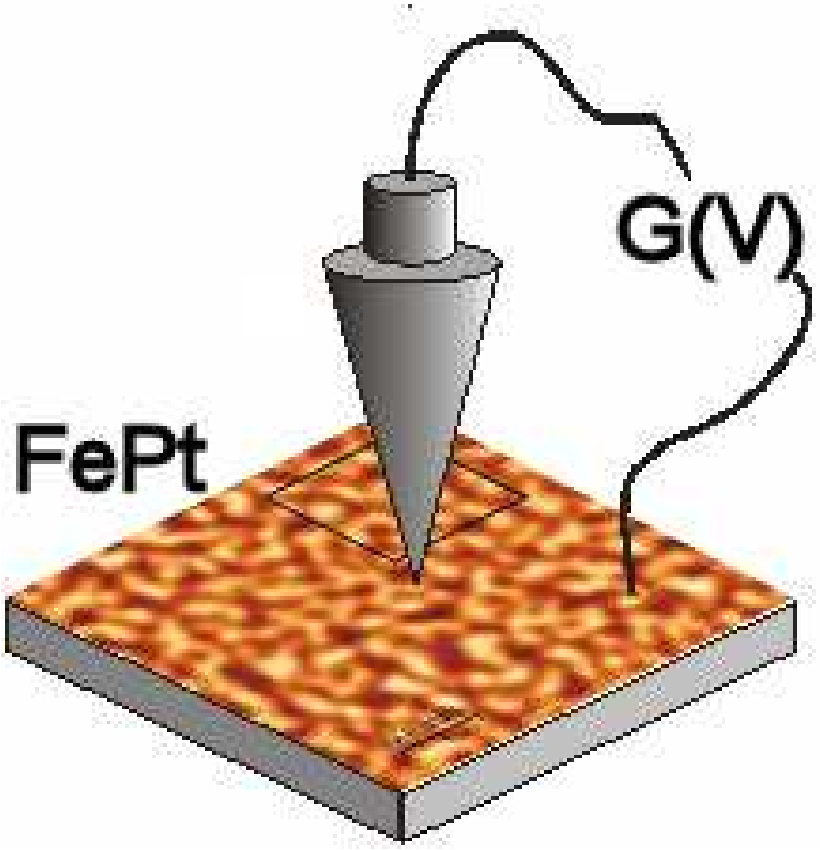

Figure III .14: Principle of the point-contact Andreev reflection experiments (Drawing courtesy of C.H. Marrows).

material, can pose a substantial expansion in the apparent superconducting band gap typically visible in G vs. V_{bias} for low Z and high P contacts. This additional series resistance is henceforth addressed as spreading resistance $R_{\text{spreading}}$, which is corrected for in the following chapter.

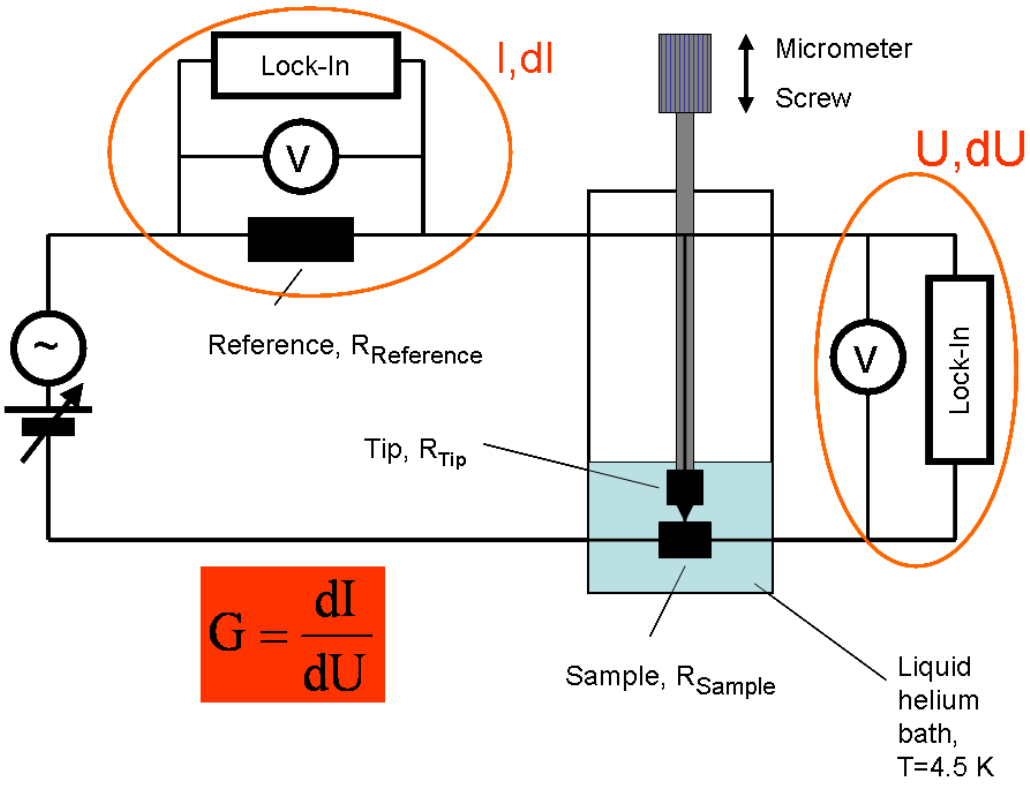

Figure III .15: The AC lock-in technique used in PCAR experiments to measure the differential point-contact conductance as a function of bias voltage.

Chapter IV

Experimental Results and Discussion

The following chapter will focus on quantitative experimental findings of fundamental electron transport properties in the epitaxial $L1_0$-ordered ferromagnets FePd and FePt. More precisely, the details of preparation and above all a thorough crystallographic magnetic and microstructural characterization to the thin films will be given. Subsequently, an investigation of the magnetoresistive properties of the $L1_0$-FePd and -FePt follows, which serves as the basis for evaluating the diffusive current spin polarization in both materials. A comparison with the ballistic current spin-polarization follows which is extracted from point-contact Andreev reflection spectroscopy. Finally, the anomalous Hall effect is accounted for quantitatively in both materials in the case of equal degree of long range ordering in FePt and FePd and a measure for the skew scattering Hall angle per individual electron scattering event is given.

IV .1 Preparation and characterization of $L1_0$-FePd and -FePt

High vacuum magnetron-sputter deposition was used to prepare the samples on polished MgO(001) substrates. A 4%-hydrogen-argon sputter gas mixture was used to prevent film oxidation during growth at high temperatures of $T = 700$ °C. The FePt and FePd magnetic thin films with a typical thickness of ≈ 30 nm were sputtered by co-deposition directly onto single crystal MgO(001) substrates at a deposition rate of $0.1 - 0.2$ Ås^{-1}. A film thickness of ≈ 30 nm provides enough $L1_0$-bilayers — FePt or FePd — for electron transport experiments to exhibit bulk-like features without surface or interface reflection features and artefacts.

For structural characterization of the epitaxial $L1_0$-ordered thin films, θ-2θ x-ray diffraction scans have been carried out using Cu-K_α radiation in order to determine the long range order parameter S ($0 \leq S \leq 1$), as described in III .3. A typical θ-2θ scan of $L1_0$-ordered FePt is depicted in figure IV .1. The (001)-peak and (002)-peaks, that occur due to Bragg diffraction of x-ray photons of a wavelength of 1.54Å from $< 001 >$- and $< 002 >$-lattice planes [79, 95], were fitted employing the Lorentz line shape, yielding a long range chemical order parameter of $S = 0.90 \pm 0.01$ at a film thickness of 31.0 nm. The main parameters determining the long range order parameter given in x-ray θ-2θ scans are the position, the intensity and the integrated intensity of the (001)-peaks and (002)-peaks. The film thickness were determined via Kiessig-fringes III .3 obtained in low-angle x-ray reflectometry measurements, see figure III .5.

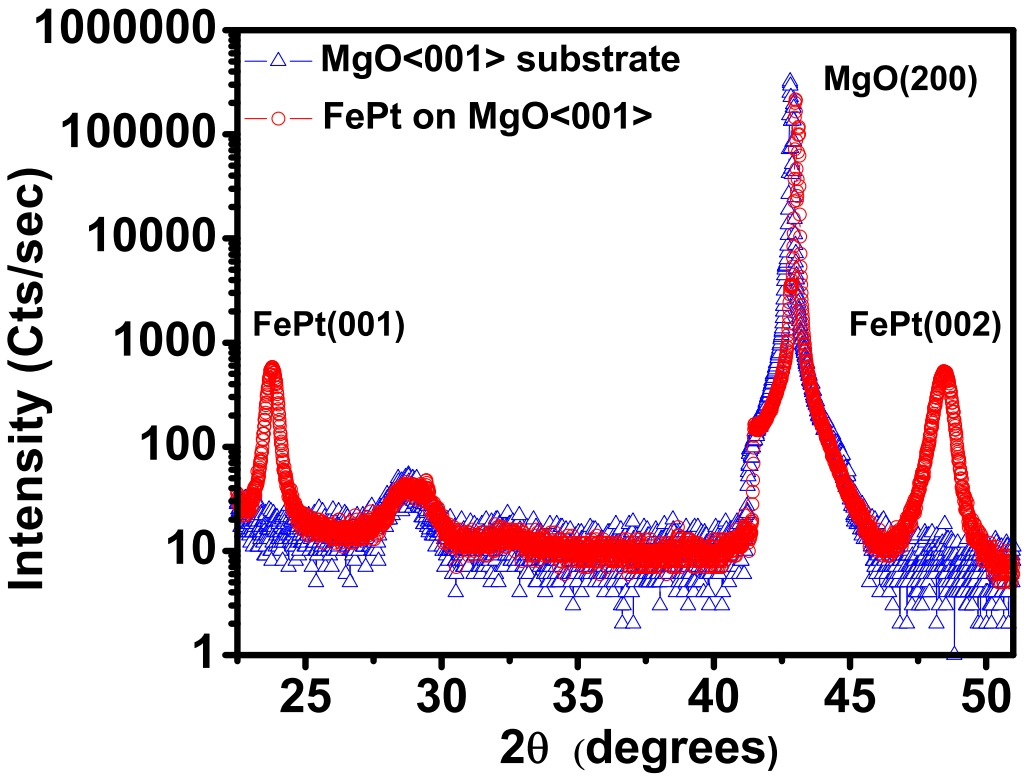

Figure IV .1: $\theta - 2\theta$ x-ray scans for $L1_0$-ordered FePt of a film thickness of 31 nm. The MgO(001) substrate scan is included for comparison.

A quantitative analysis of the strong out-of-plane magnetic anisotropy[96, 62, 97, 98, 99] of the $L1_0$-ordered films were carried out by vibrating-sample-magnetometry (VSM) in the out-of-plane geometry as well as the in-plane geometry, as shown in figure IV .2. The easy-axis magnetic anisotropy was calculated from[97]

$$K_{\perp} = \mu_0 \cdot \int_0^{M_{Sat}} (H_{hard-axis} - H_{easy-axis}) dM + K_{\mathrm{demag}}, \qquad \text{(IV .1)}$$

where the extra term $K_{\mathrm{demag}} = \frac{1}{2}\mu_0 M_{\mathrm{sat}}^2$ accounts for the demagnetization field within the sample. At $T = 276$ K, one finds for the $L1_0$-FePt film investigated further by electron transport experiments in sections IV .2.1 and IV .3.1 the values for the micromagnetic parameters $K_{\perp} = 1.9 \pm 0.2$ MJm^{-3}, $M_{\mathrm{sat}} = 1.0 \pm 0.1$ MAm^{-1}, and $A = 14.2 \pm 4$ pJm^{-1}. The exchange stiffness was deduced from a $T^{\frac{3}{2}}$-Bloch law fit of the temperature dependence of the saturation magnetization [51]. These values compare reasonably well with the micro-magnetic parameters recently reported for $L1_0$-ordered FePt thin films grown by molecular beam epitaxy and magnetron-sputtering of other groups. [100, 101, 12, 13, 102, 103].

The magnetic domain structure of FePt was imaged by magnetic force microscopy (MFM)[84, 85], at room temperature in zero field, as shown in figure IV .3(a) and IV .3(b). The sample was demagnetized using an alternating magnetic field of decreasing amplitude. The cantilevers had a resonant frequency of 65 kHz and a spring constant of 1-5 N/m. The CoCr-coated Si tip was vertically magnetized prior to imaging. For optimal contrast the tip-surface distance was kept constant at 20 to 25 nm. The average magnetic domain width of the demagnetized state was obtained by a power-spectrum analysis and resulted in a domain width of $D = (170 \pm 15)$ nm for the 31.0

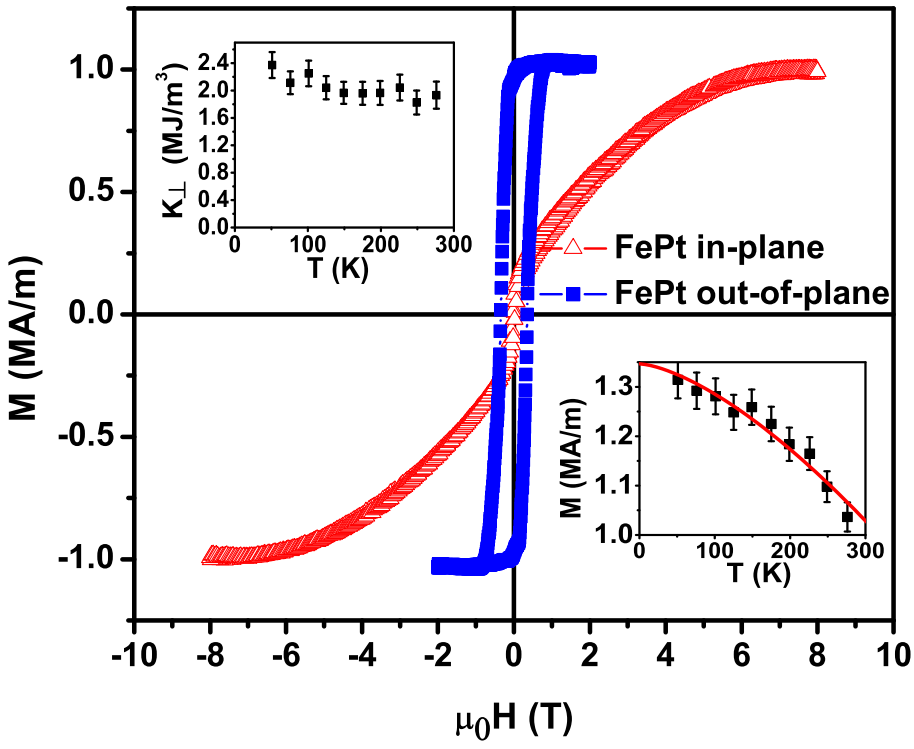

Figure IV .2: Hysteresis loops for the 31 nm thick $L1_0$-ordered FePt film obtained by vibrating-sample-magnetometry in the in-plane and out-of-plane geometry at $T = 276$ K. The two insets depict the uniaxial anisotropy constant $K_\perp$ and the saturation magnetization together with a Bloch-law fit as a function of temperature. Paramagnetic impurities within the MgO substrate make assessment of hysteretic properties unreliable at temperatures below 50 K such that magnetic parameters are only shown for temperatures above 50 K.

nm thick sample.

A micromagnetic simulation of this domain structure was carried out using the OOMMF code as described in section II .2, the results of which is shown in figure IV .3 (c). The cell size used was (1×1) nm^2 within the film plane and 15 nm perpendicular to the film plane, and a six-nearest-neighbor exchange interaction for the magnetic energy terms of adjacent cells was employed. This simulation yields an average domain width of $D \approx 150$ nm for room temperature values of the micromagnetic parameters for a 30 nm thick film and corresponds very well with the average domain width of approximately 170 nm experimentally determined from magnetic force microscopy MFM, see figure IV .3 (a) and (b). The average domain width was obtained from a Fourier analysis of the OOMMF output shown in figure IV .3 (c). The domain structure exhibits the typical interconnected dense stripe domain structure known from $L1_0$-ordered binary iron alloys [21, 12, 104, 104]. Furthermore, the average width of an individual domain wall has been calculated from

$$\delta_W \simeq \pi \sqrt{\left(\frac{A}{K_\perp}\right)}. \qquad \text{(IV .2)}$$

From equation IV .2, one thus calculates $\delta_{\mathrm{W}} \simeq 9$ nm for temperatures ranging from $T = 50$ K up to $T = 200$ K, while it increases gradually to $\delta_{\mathrm{W}} \simeq 11$ nm by $T = 280$ K. Such narrow Bloch-type domain walls are rarely achieved in other magnetic materials since they are caused by the very high magneto-crystalline anisotropy in $L1_0$-FePt and their effect on the electron transport properties such as domain wall resistance and spin polarization of a magnetic metal is therefore particularly interesting.

Transmission electron microscopy (TEM) imaging experiments have been performed on an FEI Tecnai F20 by M. MacKenzie at the University of Glas-

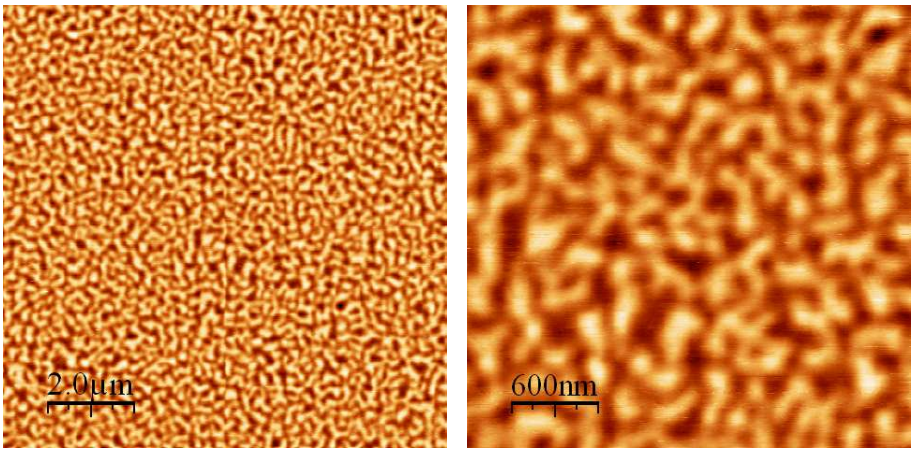

(a) (b)

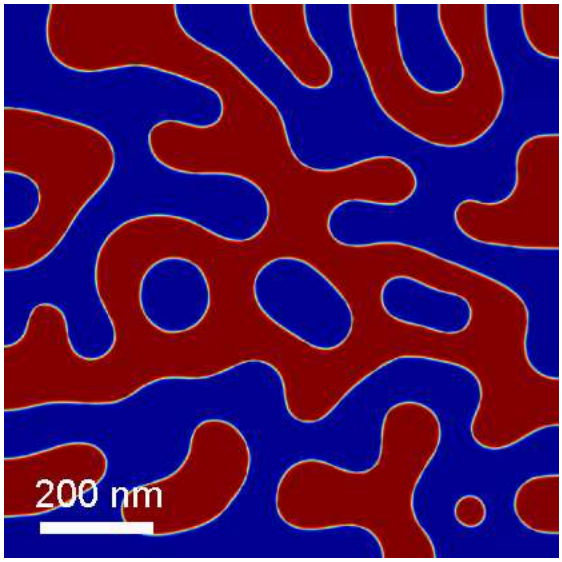

(c)

Figure IV .3: Magnetic force image showing the typical maze structure of a demagnetized $L1_0$-ordered FePt film in zero magnetic field at different scales (a) and (b). The bright and dark areas mark magnetic domains of opposite perpendicular magnetization. Micromagnetic simulation (c) of the domain structure of a $1\mu m \times 1\mu m$ FePt thin film of 30 nm thickness using the OOMMF code and experimentally determined micromagnetic parameters. The red and blue (bright and dark) regions mark areas of opposite perpendicular magnetization.

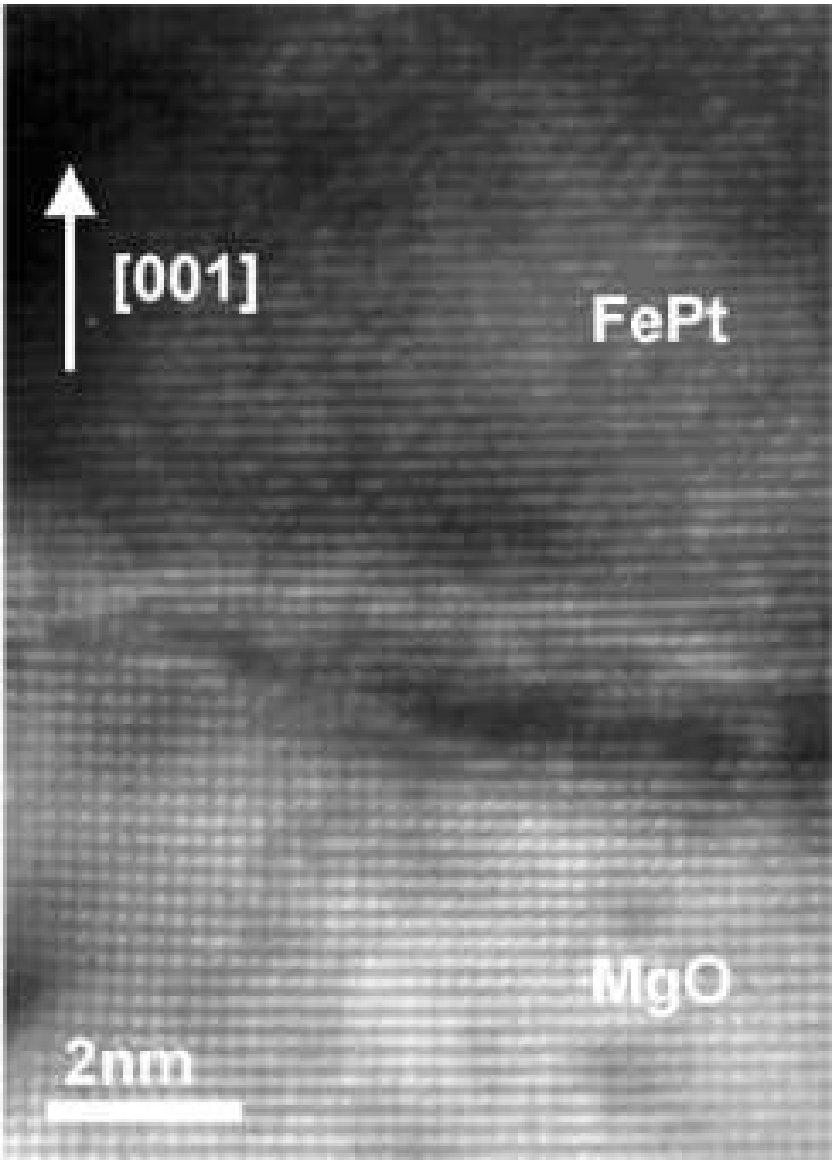

Figure IV .4: Lattice structure as obtained from HRTEM of the $L1_0$-ordered FePt thin film grown on MgO(001). The [001] direction is the growth direction within the epitaxial film (Image courtesy of M. MacKenzie and J.N. Chapman).

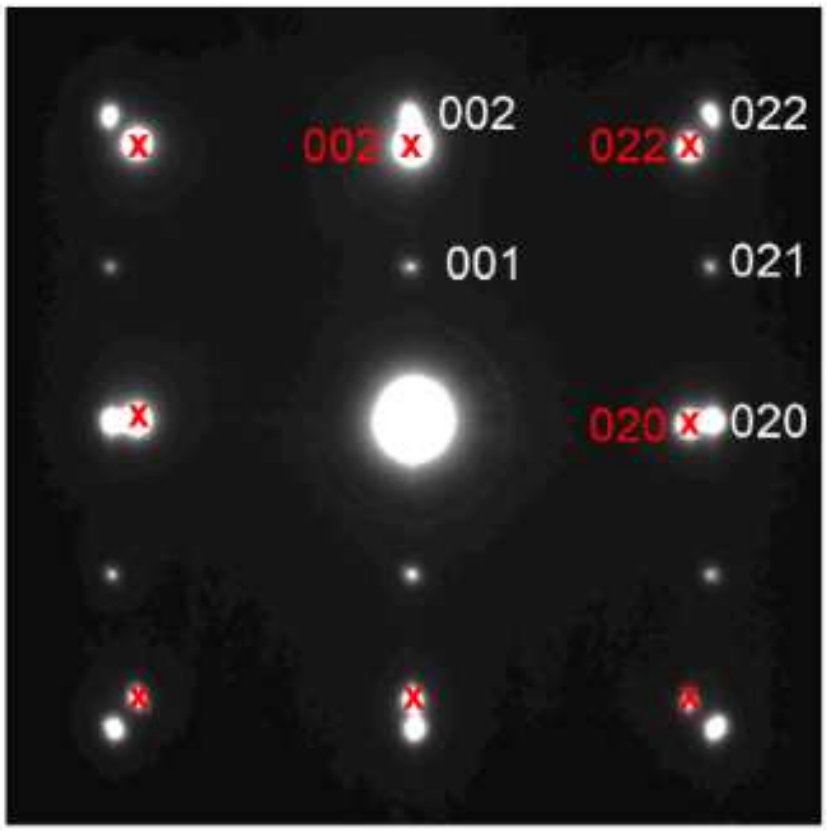

Figure IV .5: Selected area electron diffraction pattern from a cross-sectional TEM sample of FePt on MgO(001). The (001) superlattice spots confirm the $L1_0$-ordered FePt structure of the FePt thin film. The diffracted spots associated with the MgO(001) substrate are marked with crosses (Image courtesy of M. MacKenzie and J.N. Chapman).

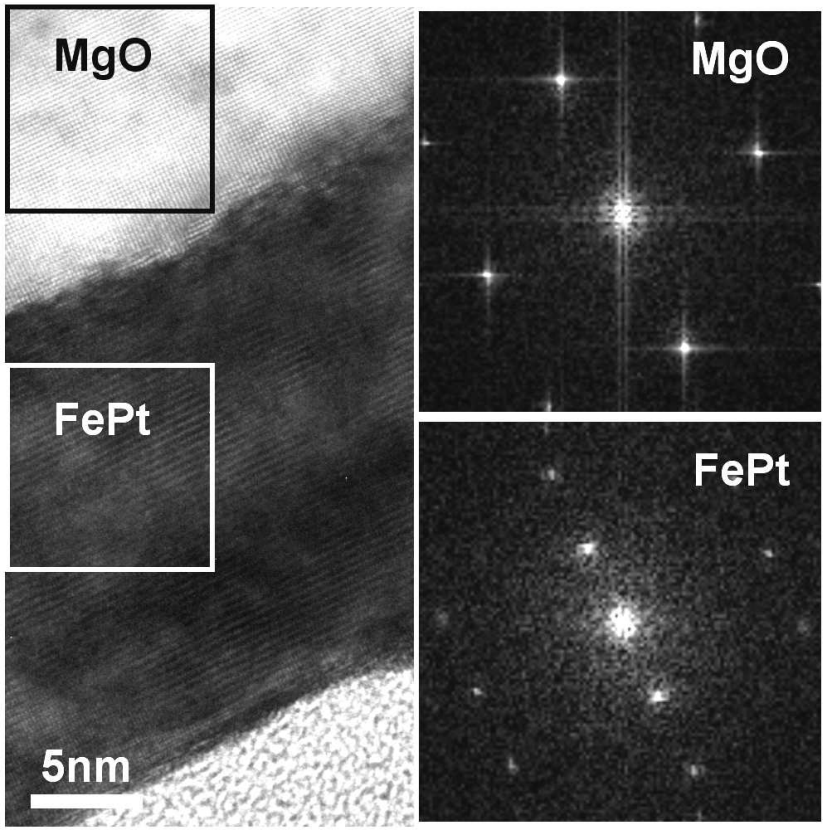

Figure IV .6: HRTEM image of an $L1_0$-ordered FePt thin film grown on MgO(001). Inset are FFT patterns obtained from the regions of the single crystal MgO substrate and the epitaxial FePt layer marked with boxes. It can be seen that the superlattice spots are associated with the FePt layer (Image courtesy of M. MacKenzie and J.N. Chapman).

gow to provide structural information on the material investigated [105]. The cross-sectional high-resolution transmission electron microscopy (HRTEM) image in figure IV .4 from a comparable sample, taken with the electron beam aligned parallel to the [100] or [010] zone axis of the MgO substrate confirms the high quality of the epitaxial FePt layers on the MgO(001) substrates. The $L1_0$-ordering of the FePt was verified by selected area electron diffraction, see figure IV .5, which shows the diffraction pattern from a cross-sectional TEM of the same sample of FePt on MgO(001). The high degree of alignment between the MgO and FePt structures is clearly depicted. The {002} and {022} reflections from the face-centered cubic MgO substrate are marked with red crosses and show the expected four-fold symmetry associated with the [100] zone axis. The remaining reflections are from the FePt layer and index as the [100] zone axis of $L1_0$-ordered face-centered tetragonal FePt. The presence of the (001)-superlattice spots confirms the $L1_0$-ordering of FePt. In figure IV .6 another image is shown with a larger field of view. Fast Fourier Transform (FFT) patterns obtained from the boxed areas in figure IV .6, and shown as insets, confirm that the superlattice spots seen in the electron diffraction pattern are associated with the $L1_0$-order in the FePt layer. Using a lattice parameter of 4.21 Å for MgO as a calibration, one obtains $a = 3.85$ Å and $c = 3.76$ Å for the FePt structure. This gives a lattice mismatch of 8.5 % between the MgO substrate and FePt layer. Hence, one would expect a misfit dislocation at the interface roughly every eleven atomic spacings, and a careful examination of a Fourier filtered image (not shown) reveals these. One also observes a much smaller number of dislocations in the bulk of the film, at roughly the same density as in the MgO substrate. These

filtered HRTEM images also reveal that the $L1_0$-FePt film relaxes the strain arising from the lattice mismatch within the first ten FePt atomic bilayers, see figure IV .7(a) and IV .7(b).

IV .2 Diffusive electron transport properties

Including the spin degree of freedom in electronic devices is the central concept of spintronics. The proposal of the spin field-effect transistor by Datta and Das [106], which relies on generating, manipulating, and detecting spin-polarized currents, triggered enormous activity and effort to understand and control spin-transport [6]. An area of active interest at present is domain wall (DW) spintronics [23], where spin-polarized currents interact with local magnetization gradients, giving rise to additional resistance[27, 26] and spin-transfer torques [107, 108]. A key parameter here is the degree of spin-polarization P of the current that flows, and so a proper definition of P in the appropriate transport regime is required [109, 87].

P is defined as the unpaired fraction of the current when resolved into the contributions to the current density J carried by the spin-$\uparrow$ and spin-$\downarrow$ carrier populations, $P = (J_\uparrow - J_\downarrow)/(J_\uparrow + J_\downarrow)$. Since these current densities are driven by the same electric field $\mathcal{E}$, one can use Ohm's law $J = \sigma\mathcal{E}$ to write the formula in terms of spin-resolved conductivities, $P = (\sigma_\uparrow - \sigma_\downarrow)/(\sigma_\uparrow + \sigma_\downarrow)$. Determining P now amounts to finding an expression, appropriate to the transport regime in question, for these conductivities. In a ballistic experiment, such as point contact Andreev spectroscopy (PCAR) [54, 53], these will be determined solely by the electronic structure. In the diffusive regime the spin-dependent scattering rates $1/\tau_{\uparrow(\downarrow)}$ will also play a role. Examples

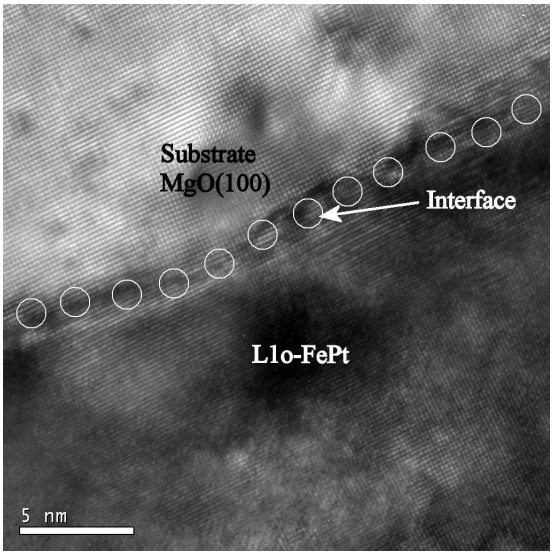

(a)

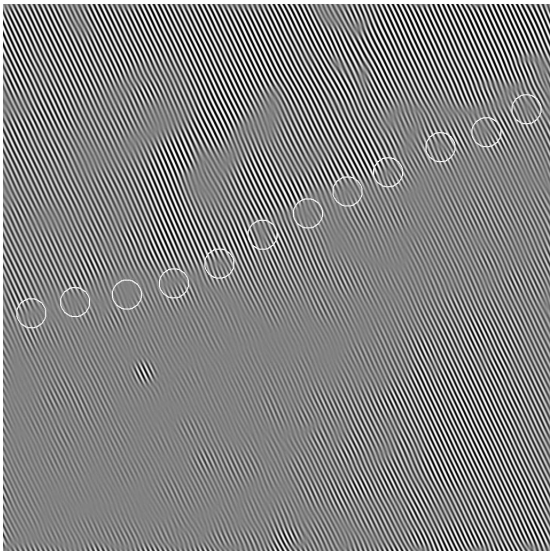

(b)

Figure IV .7: High resolution TEM micrograph of the $L1_0$-FePt/MgO(100) interface (a), the encircled dislocations appear on average at every 11th atomic plane facilitating strain relaxation due to lattice mismatch between the monocrystalline MgO substrate and the $L1_0$-FePt film, see Fourier-filtered image in (b). The core of the dislocation appears within the first ten atomic planes of the $L1_0$-FePt film, i.e. close to the interface itself (Image courtesy of M. MacKenzie and J.N. Chapman).

of explicit expressions for P will be given below and may also be found in references [109], [23] and [87].

The Levy-Zhang (LZ) theory of DW resistance for diffusive transport [26] parameterizes the transport in terms of a spin-asymmetry in conductance $\alpha = \sigma_\uparrow/\sigma_\downarrow$, directly related to the current polarization by [109, 14]

$$P = \frac{g_\uparrow(E_\mathrm{F})v_{F,\uparrow}^2\tau_\uparrow - g_\downarrow(E_\mathrm{F})v_{F,\downarrow}^2\tau_\downarrow}{g_\uparrow(E_\mathrm{F})v_{F,\uparrow}^2\tau_\uparrow + g_\downarrow(E_\mathrm{F})v_{F,\downarrow}^2\tau_\downarrow} = \frac{(\alpha_\mathrm{diffusive}-1)}{(\alpha_\mathrm{diffusive}+1)}, \qquad \text{(IV .3)}$$

where $\sigma \propto g(E_\mathrm{F})v_F^2\tau$ is expressed within the Drude formalism based on bandstructure characteristics. Accordingly, one writes the spin-asymmetry in conductance for diffusive electron transport

$$\alpha_\mathrm{diffusive} = \frac{\sigma_\uparrow}{\sigma_\downarrow} = \frac{g_\uparrow(E_\mathrm{F})v_{F,\uparrow}^2\tau_\uparrow}{g_\downarrow(E_\mathrm{F})v_{F,\downarrow}^2\tau_\downarrow}. \qquad \text{(IV .4)}$$

On the other hand, a common method of measuring spin-polarization is to use point contact Andreev spectroscopy (PCAR) [54, 53], where the polarization of a ballistic current crossing an interface from the ferromagnet into a superconductor is measured. Following I. Mazin [109], by analogy one defines in the ballistic case

$$\alpha_\mathrm{ballistic} = \frac{g_\uparrow(E_\mathrm{F})v_{F,\uparrow}}{g_\downarrow(E_\mathrm{F})v_{F,\downarrow}}, \qquad \text{(IV .5)}$$

where there is no dependence on the spin-dependent relaxation times $\tau_{\uparrow,\downarrow}$, which will play a role in the diffusive regime however as can be seen in equation IV .3 and IV .4. In both cases, $g_{\uparrow,\downarrow}(E_\mathrm{F})$ and $v_{F,\uparrow,\downarrow}$ are the spin-dependent densities of states at the Fermi level and Fermi velocities, respectively.

IV .2.1 Transport in the diffusive regime $L1_0$-ordered FePt

First, the diffusive transport properties of $L1_0$-ordered FePt are described. Magnetotransport measurements at temperatures ranging from 2 K to 258 K have been performed using an in-line 4-terminal set-up with the magnetic field applied normal to the film plane. One finds a hysteretic part of the magnetoresistance of $MR_{\mathrm{Domain}} = 0.55$ % at 2 K and $MR_{\mathrm{Domain}} = 0.26$ % at 258 K, associated with the creation and annihilation of domain walls as the film switches its magnetization direction. A typical MR hysteresis loop is shown in figure IV .8. From previous studies on $L1_0$-ordered FePd thin films [14], one knows that a sufficiently high quality factor $Q = 2K_{\perp}/\mu_0 M^2$ as similarly in this case, $Q \approx 2.2$, is a good indication that the anisotropy magnetoresistance (AMR) contribution of Néel closure caps on the domain walls cannot account for this effect and is small enough to be neglected. The asymmetry of the MR loops arises through the anomalous Hall effect, caused by large spin-orbit interaction in FePt, and the minute misalignment of the voltage probes. This effect can be easily subtracted to give the true domain wall MR. The anomalous Hall effect in films such as these will be discussed in the last chapter. One finds the domain wall MR to be approximately twice as large as compared to those reported on $L1_0$-ordered FePt films grown by molecular beam epitaxy [110], even though the film had a rather high electrical resistivity of $\rho = 35$ $\mu\Omega$ cm (at 2 K), which implies that the mean free path is in the nanometer regime. The residual resistivity ratio is $RRR = 2.4$. The temperature dependence of the domain wall MR is shown in figure IV .9 (a) and exhibits an almost linear behavior with temperature.

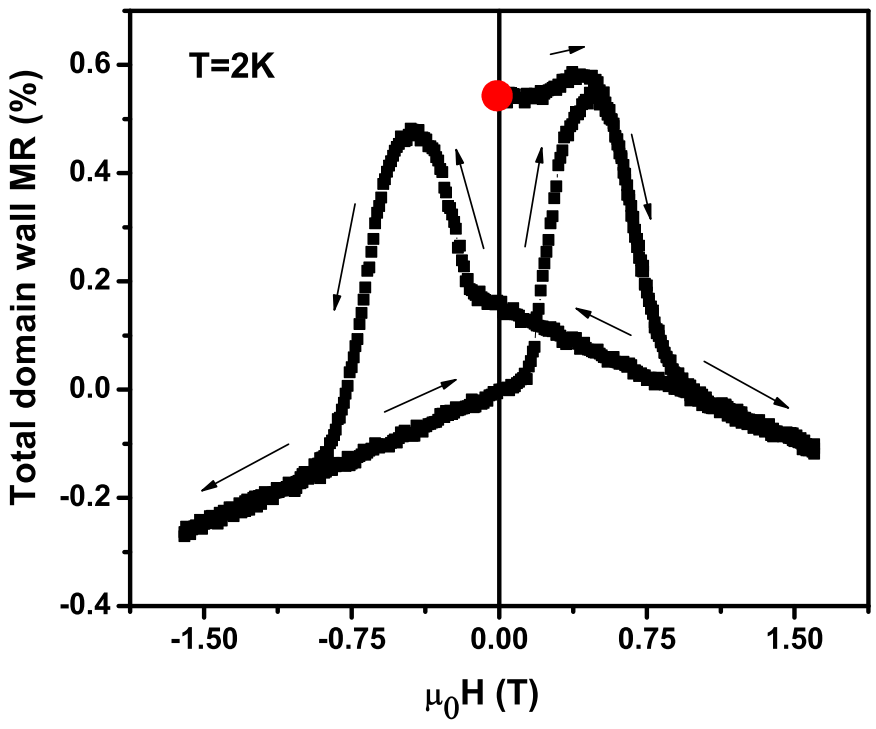

Figure IV .8: Magnetoresistance vs. applied field of $L1_0$-ordered FePt obtained by a DC in-line 4-terminal measurement at $T = 2$ K in the perpendicular field geometry.The dot marks the resistance in the demagnetized state of the sample, at the start of the virgin branch of the hysteresis loop. The asymmetry in the hysteretic loop is due to the anomalous Hall effect (AHE) which will be a topic in chapter IV .4.

In addition to the hysteretic part of the MR one observes a reversible linear part at high fields. The high field MR slopes $\partial(\Delta\rho/\rho)/\partial B$ have been extracted at an applied magnetic field of 5 T at various temperatures (figure IV .9 (b)). In Fe, Co, and Ni, such a negative and linear MR was found by Raquet et al. [111] to be caused by the influence of a magnetic field on the spin mixing resistivity due to magnons. As the introduction of a magnetic field causes a gap in the magnon spectrum, the main role is played by spin-flip *s-d* inter-band and intra-band scattering due to electron-magnon scattering. The data in figure IV .9 (b) can be fitted with the expression

$$\frac{\partial(\Delta\rho/\rho)}{\partial B} = \frac{T(\ln T + \text{const.})}{1 + d_1 T^2} \qquad \text{(IV .6)}$$

given by Raquet et al. [112] quite well, with the exception that a substantial linear MR ($\partial(\Delta\rho/\rho)/\partial B = -0.0054$ T^{-1}) remains even at the lowest temperatures in this film, which must be added as an additional constant term. (A negligibly small contribution $\propto B^2$ as was the case in FePd [14] was observed.) In equation IV .6, d_1 denotes the ratio of the T^2 coefficient in the temperature dependence to the low temperature value [112, 113, 14]. Subsequently, it was possible to fit the temperature dependence of the high-field MR slope (figure IV .9 (b)) according to Raquet et al. [112]. This procedure yields a magnon mass renormalization constant of $d_1 \approx -6.0 \times 10^{-7}$, which is comparable with that of pure $3d$ metals [113], and less negative than that found previously in MBE-grown FePd [14]. There is no simple explanation for the temperature independent part of the high-field linear MR, although one has to note that magnetoresistances in thin films can take on a variety of unexpected forms [114].

Furthermore, magnetoresistance data were used to compute the spin-current

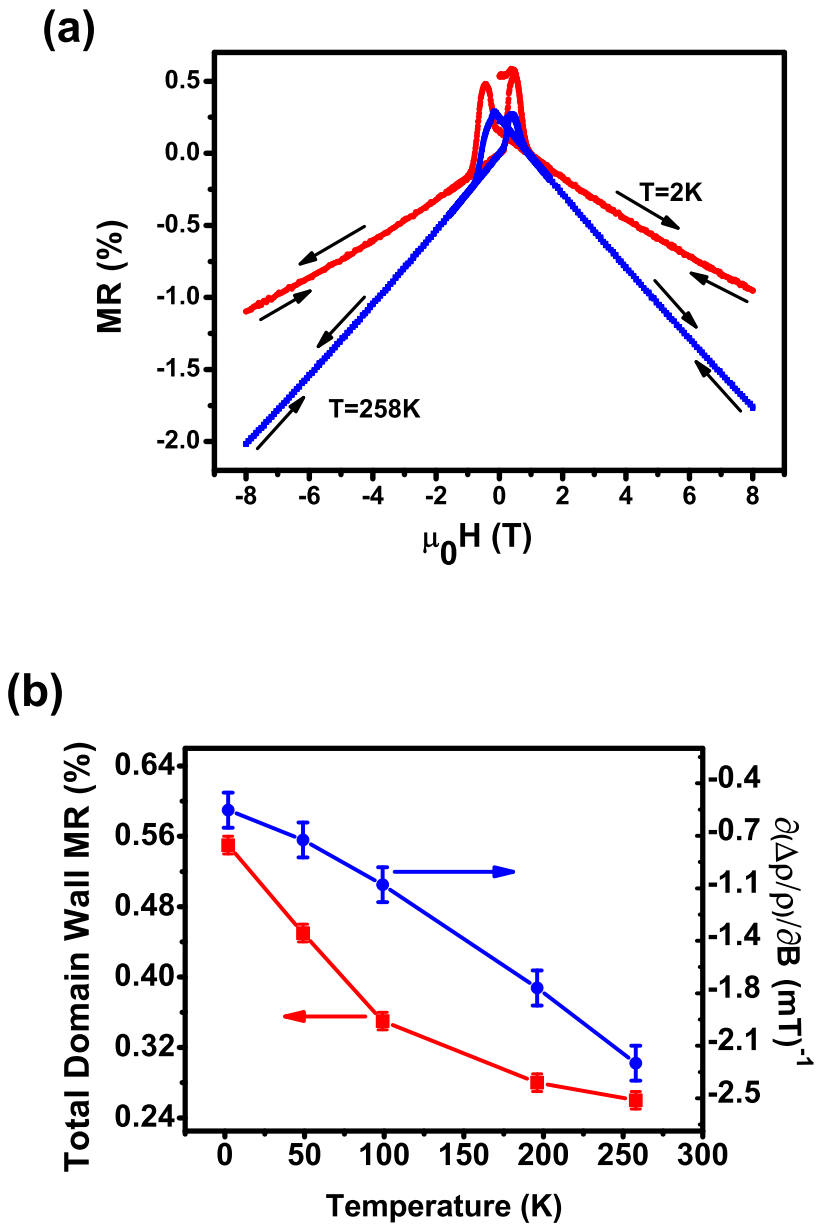

Figure IV .9: (a) The hysteretic MR loops obtained for $L1_0$-ordered FePt at $T = 2$ K and $T = 258$ K in the perpendicular field geometry. A strong linear high field magnetoresistance is evident in both cases. (b) Total domain wall MR (squares) and high field MR slope (circles) vs. temperature for a $L1_0$-ordered FePt thin film of a thickness of 31 nm. The solid line is a fit to the data as described in the text.

asymmetry parameter α in $L1_0$-ordered FePt based on the Levy-Zhang spin-mistracking model [26]. The spin asymmetry of the current depends on the spin-resolved conductivities $\sigma_\uparrow$, $\sigma_\downarrow$ (or spin-resolved resistivities $\rho_\uparrow$, $\rho_\downarrow$) of the majority and minority spin channels and is given by $\alpha = \sigma_\uparrow/\sigma_\downarrow = \rho_\downarrow/\rho_\uparrow$. The Levy-Zhang model describes the MR only in the wall region, whereas in this case the entire film was measured. One estimates the volume fraction of walls by measuring the total wall length λ_W in the MFM image of scan width Λ and multiplying this by the wall thickness δ_W to obtain the total area occupied by of walls, out of a total area of Λ^2. This procedure yields a volume fraction accounting for the fact that there is no parallel stripe domain state present, but rather a labyrinth structure, and yields a value approximately 1.3 times greater than the ideal stripe domain value δ_W/D. Thus one obtains for an isotropic labyrinth domain state a domain wall magnetoresistance of[14]

$$\frac{\Delta\rho}{\rho} = \frac{1}{5}\left(\frac{\lambda_W \delta_W}{\Lambda^2}\right)\left(\frac{\pi\hbar^2 k_F}{4mJ\delta_W}\right)^2 \frac{(\alpha-1)^2}{2\alpha}\left(4 + \frac{10\sqrt{\alpha}}{\alpha+1}\right), \qquad \text{(IV .7)}$$

where k_F is the Fermi wave vector, m is the effective electron mass and J is the Stoner exchange-splitting energy. It is to be noted that this formula yields the same $\Delta\rho/\rho$ for both α and $1/\alpha$, equivalent to saying that there is no sensitivity to the sign of the polarization. Based on the assumption that the majority carriers are s-like, one takes m to be equal to the free electron mass, assume the value of k_F to be 2 Å^{-1} (a typical value for a metal), and take a value for the Stoner exchange splitting to be $J = 2.0$ eV based on the splitting of the density of states seen in the results of band structure calculations [115]. The domain wall volume fraction was scaled appropriately based on the analytical values for δ_W and D for different temperatures. Figure IV .10 (a) shows the spin current asymmetry α of $L1_0$-ordered FePt calculated

according to equation IV .7. A strong temperature dependence of α is clearly visible, with a decay of the spin current asymmetry from $\alpha = 16$ to $\alpha = 10$ in the temperature range between 2 K and 258 K. It is then straightforward to obtain the diffusive current spin polarization of $L1_0$-ordered FePt from

$$P_{\text{diffusive}} = \left(\frac{\sigma_\uparrow - \sigma_\downarrow}{\sigma_\uparrow + \sigma_\downarrow}\right) = \left(\frac{\alpha - 1}{\alpha + 1}\right), \qquad \text{(IV .8)}$$

which is shown in figure IV .10 (b). For a temperature of 258 K, one finds a diffusive spin current polarization of $P_{\text{diffusive}} = 0.82 \pm 0.04$, whereas $P_{\text{diffusive}} = 0.88 \pm 0.02$ at $T = 4.2$ K. The uncertainties in these polarization values are determined from the uncertainties in the α-values, which in turn were computed using equation IV .7, and also taking into account the uncertainties of the micromagnetic parameters $K_\perp$, M and A taken to evaluate the domain wall dilution. The final uncertainties are small since the diffusive polarization is rather insensitive to the value of α when $\alpha \gg 1$. The values obtained for the diffusive current spin-polarization $P^{\text{FePt}}_{\text{diffusive}}$ are considerably higher than one might expect at first glance considering the current spin polarization values reported for elemental Fe for example obtained by conventional point contact Andreev reflection spectroscopy technique (PCAR), i.e. $P^{\text{Fe}}_{\text{ballistic}} = 0.46 \pm 0.03$ [116]. Moreover, $P^{\text{FePt}}_{\text{diffusive}}$ does not exhibit a very strong temperature dependence and even near room temperature at $T = 258$ K the diffusive current spin polarization $P^{\text{FePt}}_{\text{diffusive}}$ lies beyond 80 %. However, spin-dependent scattering rates differing for minority and majority spin carriers in the diffusive electron transport regime seem to be decisive in a large spin-channel resistivity asymmetry α and hence a large diffusive current spin polarization. The direct comparison with PCAR results for $L1_0$-material will follow in IV .3.1 and V .

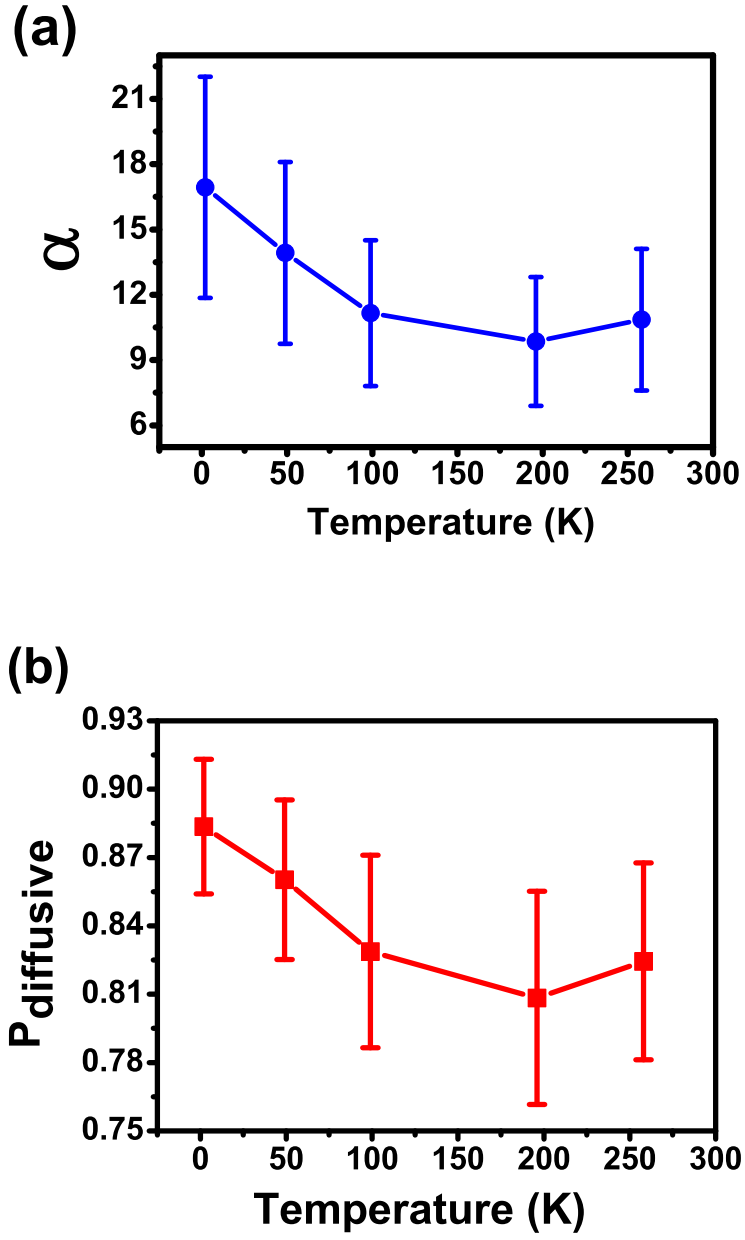

Figure IV .10: The T dependence of the spin resistivity asymmetry α (a) and the diffusive current spin polarization $P_{\text{diffusive}}$ (b).

IV .2.2 Transport in the diffusive regime $L1_0$-ordered FePd

In the following, the diffusive electron transport properties in $L1_0$-FePd thin films with varying crystallographic long range order parameter are accounted for. The varying ordering of the magnetic films is manifested in terms of changing the content in Pd atoms, the non-magnetic element in the binary FePd alloy. While maintaining the $L1_0$-phase, the degree of crystallographic long range ordering is tuned with Pd content in the $L1_0$-phase which in turn has the interesting consequence that the magnetotransport varies significantly as well.

The role of spin-dependent impurity scattering in the spin-polarization of a diffusive current $P_{\text{diffusive}}$ in ferromagnetic $L1_0$-ordered $Fe_{(1-x)}Pd_x$ epilayers is elucidated, whose crystal structure gives rise to a strong magnetic easy axis that is oriented perpendicular to the film plane, yielding dense, narrow DWs. The chemical order parameter S was reduced by varying x. The extra Pd atoms act as spin-dependent scattering centers, changing the scattering rates $1/\tau_{\uparrow(\downarrow)}$, in such a way as to give both higher resistivity and DW magnetoresistance (MR). The DW MR was measured to quantify the resulting rise in $P_{\text{diffusive}}$ [14], while PCAR conductance spectroscopy was used to address the ballistic case. As might be expected, the PCAR results are unaffected by the changes in $\tau_{\uparrow(\downarrow)}$.

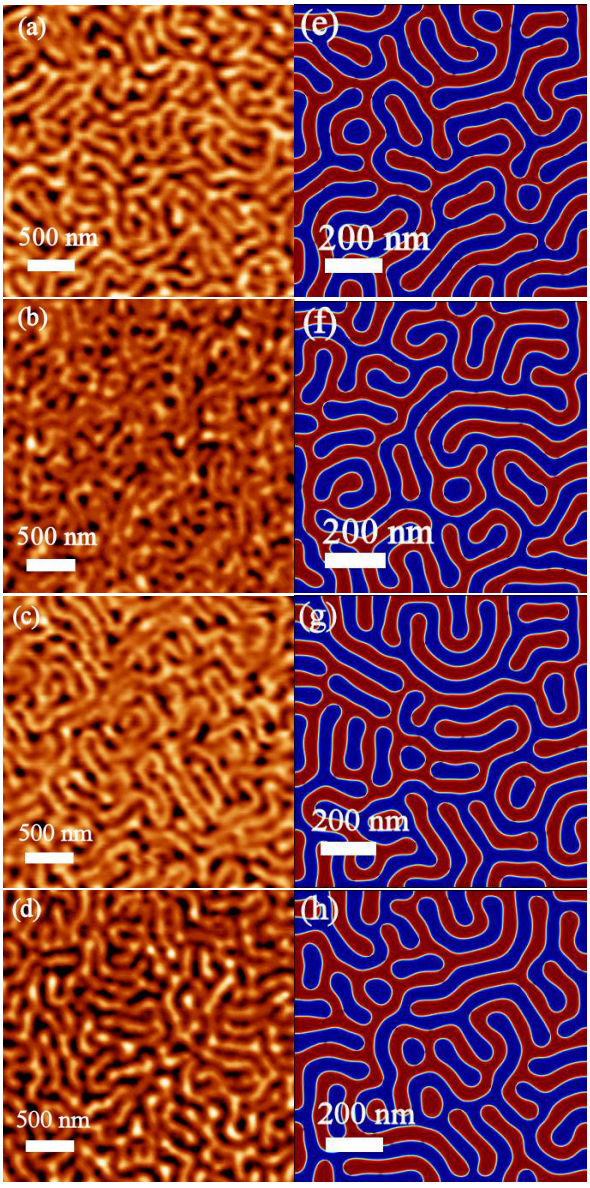

Figure IV .11: Magnetic force micrographs of the $L1_0$-$Fe_{(1-x)}Pd_x$ samples (a) corresponding to $S = 0.39$, (b) $S = 0.52$, (c) $S = 0.72$ and (d) $S = 0.80$ illustrating the labyrinth domain pattern typical for this magnetic material at the demagnetized state in zero applied field and at room temperature. For purposes of direct comparison, this domain state was simulated micromagnetically (e) corresponding to $S = 0.39$, (f) $S = 0.52$, (g) $S = 0.72$ and (h) $S = 0.80$ employing sample specific magnetic parameters such as saturation magnetization $M(T)$, exchange stiffness constant $A(T)$ and uniaxial anisotropy constant $K(T)$ determined from variable temperature vibrating sample magnetometry.

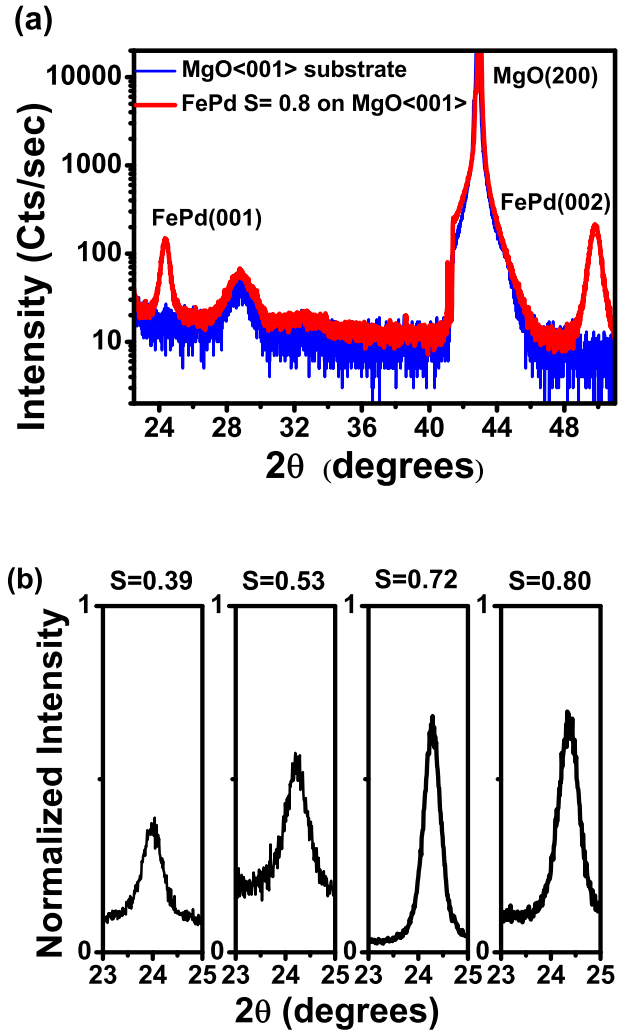

Figure IV .12: (a) θ-2θ x-ray crystallography scan for $L1_0$-ordered FePd of a film in the thickness range of 30 nm (red graph) showing pronounced (001)- and (002)- peaks yielding a chemical long range order parameter of $S = 0.8$. The MgO(001) substrate scan is included for comparison (blue graph) and allows the identification of all other features in this x-ray scan such as the (200) MgO substrate peak as pointed out. (b) The (001) superlattice x-ray diffraction peaks of each sample normalized to a common (002) peak. The maximal peak height is one indicator for the chemical ordering of the film, the exact chemical order parameter S determined as described in the text is denoted in each case ranging from $S = 0.39$ to $S = 0.8$.

Table IV .1: Magnetic properties, such as the micromagnetic parameters A, $K_\perp$ and M_s, the average domain width as determined from MFM experiments $\overline{D}_\mathrm{MFM}$ and Oommf simulations $\overline{D}_\mathrm{Oommf}$ and the resistance due to magnetic domain walls DW MR of the four $Fe_{1-x}Pd_x$ epilayers studied. The crystallographic long range ordering S was determined as described in the text. Tabulated is also an estimated domain wall width δ_W, the sheet film resistivity ρ at $T = 4.5$ K and the DW MR ratio at $T = 4.5$ K.

S	A (pJ/m)	$K_\perp$ (MJ/m^3)	M_s (MA/m)	$\overline{D}_\mathrm{MFM}$ (nm)	$\overline{D}_\mathrm{Oommf}$ (nm)	δ_W (nm)	ρ ($\mu\Omega$cm)	DW MR (%)
0.39 ± 0.05	8.1 ± 0.4	0.8 ± 0.1	1.1 ± 0.1	95 ± 10	88 ± 10	10.0 ± 0.9	17 ± 3	2.0 ± 0.1
0.53 ± 0.05	10.0 ± 0.1	0.9 ± 0.1	1.2 ± 0.1	93 ± 10	85 ± 10	10.4 ± 0.8	18 ± 4	1.3 ± 0.1
0.72 ± 0.05	13.2 ± 0.1	1.2 ± 0.1	1.4 ± 0.1	96 ± 10	83 ± 10	10.4 ± 0.6	9 ± 3	1.1 ± 0.1
0.80 ± 0.05	16.0 ± 0.6	1.5 ± 0.1	1.5 ± 0.1	91 ± 10	89 ± 10	10.2 ± 0.5	9 ± 2	1.0 ± 0.1

IV .2.2.1 Magnetic properties and domain wall magnetoresistance in $L1_0$-$Fe_{(1-x)}Pd_x$

A careful characterization of all $L1_0$-FePd samples has been performed with respect to the magnetic and crystallographic properties. Specifically, magnetic force microscopy has been employed to show the topological labyrinth domain state so typical for this magnetic material. Additionally, a thorough magnetometric investigation was carried out to quantitatively account for the micromagnetic parameters, which were directly fed into computer simulations to reconstruct the experimentally observed domain states. Subsequently, magneto-transport experiments lie at the heart of investigations towards the diffusive current spin polarization in $L1_0$-$Fe_{(1-x)}Pd_x$.

The samples were prepared by conventional dc magnetron sputter co-deposition on polished MgO(001) substrates, i.e., Fe and Pd were deposited simultaneously onto one target. The Pd content x in the $L1_0$-$Fe_{(1-x)}Pd_x$ films was varied by applying powers to the Pd-magnetron-head which deviate by merely $1-3$ Watts from those applied in order to fabricate the equi-stoichiometric sample. All other sputtering parameters are identical to the ones used for $L1_0$-FePt, which are outlined in III .1 and IV .1. All films are in the thickness range of (30 ± 5) nm, whose magnetic and magneto-resistive properties we will describe in the following. Magnetic force microscopy (MFM) was employed to image the magnetic domain structure of the $L1_0$-$Fe_{(1-x)}Pd_x$ films at room temperature in zero field, as shown in figure IV .11 (a)-(d). All four samples show clear out-of-plane anisotropy leading to dense labyrinth domain patterns typical for $L1_0$ -ordered binary iron alloys[21, 12, 104]. The average magnetic domain width of the demagnetized state was deduced by a power-

spectrum analysis, the average domain widths of all four samples $\overline{D}_{\mathrm{MFM}}$ are listed in table IV .1. The magnetic force micrographs shown in figure IV .11 (a)-(d), which verify the $L1_0$-phase of all films contemplated in this work independently from other methods of characterization, are depicted with the chemical long range ordering in the films increasing successively from (a)-(d). A precise description of the evaluation of the degree of crystallographic ordering within the films is given in section III .3.

First however, it is necessary to turn to the magnetic properties of the FePd films. The exchange stiffness constant $A(T)$, the uniaxial anisotropy constant $K(T)$ and the saturation magnetization $M(T)$ were determined for each of the four films investigated from variable temperature vibrating-sample-magnetometry, performed in the same way as described in detail in III .2 and Ref. [87]. These magnetic parameters were employed to carry out micromagnetic simulations of the domain structures in each sample using the OOMMF code [117], the results of which are shown in figure IV .11 (e)-(h), again listed with the degree of crystallographic long range ordering increasing stepwise. The cell size used was (1×1) nm^2 within the film plane and 15 nm perpendicular to the film plane, and a six-nearest-neighbor exchange interaction for the magnetic energy terms of adjacent cells was employed. Although thermal activation effects are not taken into account in this type of micromagnetic code, one was nevertheless able to simulate the domain structures in our material at finite temperatures using the appropriate values of the micromagnetic parameters $A(T)$, $K(T)$ and $M(T)$ as determined from vibrating-sample-magnetometry. As might be expected, the Pd enrichment and concomitant loss of chemical order reduced the exchange stiffness

constant A, anisotropy constant $K_\perp$, and saturation magnetization M_s as measured by vibrating sample magnetometry (VSM), with all three quantities shown in relation to S in table IV .1. This provides confidence in the average domain width $\overline{D}_{\mathrm{Oommf}}$ in each of the four FePd samples as listed in table IV .1 obtained from a Fourier analysis of the OOMMF simulation output. Moreover, the average domain width evaluated from MFM images of all four samples $\overline{D}_{\mathrm{MFM}}$ agree very well with $\overline{D}_{\mathrm{Oommf}}$, see table IV .1. This is to be regarded as evidence that our experimentally determined micromagnetic parameters $A(T)$, $K(T)$ and $M(T)$ are correct in the sense that their utilization in simulating the zero-field domain pattern of all four of the samples lead to a result that one is able to verify by MFM experiments remarkably well.

Whilst the changes in A and $K_\perp$ are substantial, the DW thickness $\delta_\mathrm{W} \sim \pi\sqrt{\mathrm{A/K_\perp}} \approx 10$ nm has virtually no dependence on the crystallographic long range order parameter S (see table IV .1). Such narrow Bloch walls are characteristic for systems with high $K_\perp$ and our values relate closely to those obtained before [14, 87] those of other groups [86, 118].

Central to this work is a precise understanding of the crystallographic long range ordering in the $\mathrm{Fe}_{1-x}\mathrm{Pd}_x$ films upon enrichment with Pd. θ-2θ scans were carried out for each sample using Cu-K_α radiation, i.e. $\lambda = 1.541$ Å. The θ-2θ x-ray diffraction scan of the FePd film with atomic composition nominally at an equi-stoichiometric level is exemplified in figure IV .12 (a) together with a scan of the bare MgO(001) substrate in order to identify diffraction peaks of the epitaxial thin film unambiguously. Both (001)-peak as well as (002)-peak are pronounced and are regarded as the hallmark for

the face-centered tetragonal $L1_0$-phase of FePd. The presence of the (001)-peak is normally forbidden by the structure factor for face-centered crystal lattices, and so its observation here confirms that there is preferential ordering on the alternating α and β planes.

Figure IV .12 (b) illustrates the (001)-superlattice x-ray diffraction peaks of each sample normalized to a common (002)-peak, i.e. the (002)-peaks of all four samples have been scaled to one and the same height. Then the maximal (001)-peak height serves as one indicator for the chemical ordering of the film. Employing equation III .4 yields the exact crystallographic long range order parameter S for each sample, more precisely $S \in \{0.39, 0.53, 0.72, 0.80\}$, which represents a rather reasonable spread for the degree of crystallographic long range ordering feasible by magnetron sputter deposition. This enables us to attribute the electron transport parameters, which will be discussed further below, directly to the degree of crystallographic long range ordering in each sample. Low-angle x-ray reflectometry measurements served as the basis for evaluating the film thicknesses by the Kiessig-method which was kept to $t = 30 \pm 5$ nm for all four samples.

The diffusive electron transport properties of the sheet films were measured at 4.5 K using a standard 4-probe dc technique. The film resistivity ρ depends strongly on S, as might be expected, with data as measured at 1.5 T -a single domain state- given in table IV .1. Hence it is clear that the additional Pd atoms that disrupt the chemical ordering act effectively as scattering centers, and shorten the overall relaxation time of the electrons. However, it is remarkable that the total DW MR $\Delta\rho/\rho$ exhibits a strong enhancement with decreasing S in the FePd films, as shown in figure IV .13.

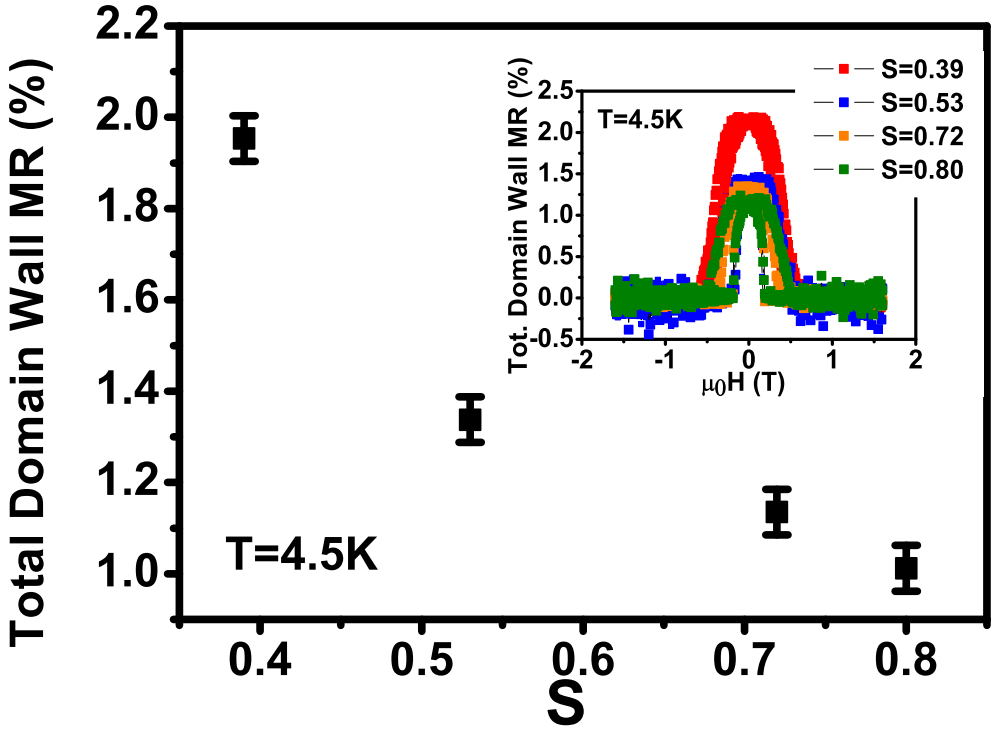

Figure IV .13: Total magnetoresistance due to Bloch type domain walls for various chemical order parameters in $L1_0$-ordered epitaxial FePd films of approximately 30 nm thickness. The inset shows the typical hysteretic behaviour of the magnetoresistance obtained by a 4-probe DC measurement on a sheet film at $T = 4.5$ K.

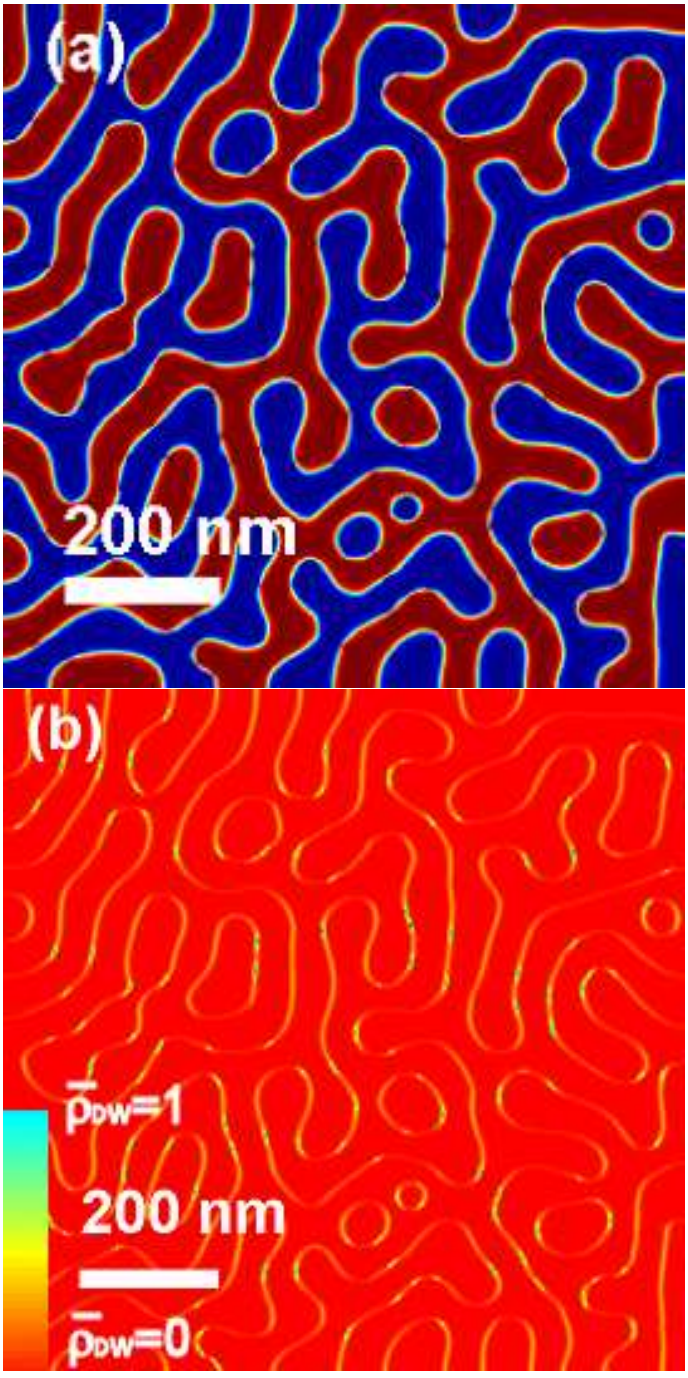

Figure IV .14: (a) Micromagnetic simulation of the stripe domain structure of a 1×1 μm^2 slab of the $S_{\text{order}} = 0.39$ film. The dark and bright areas depict regions of opposite magnetization oriented perpendicular to the film plane and separated by Bloch DWs. (b) Local DW resistance for the simulated domain state depicted in (a), assuming a current flow from left to right in straight and direct paths.

The inset to figure IV .13 shows some example MR data, the DWs give rise to the hysteretic part. The measured MR data were also corrected for 12% of the total signal which was attributable to anisotropic MR arising from the Néel caps of the Bloch DWs, based on micromagnetic modelling described below [14]. Hence, the additional resistance presented by a DW has increased by a greater proportion than the saturated ρ. It is worthwhile contrasting these data with those of Yu et al., who studied FePt films grown by molecular beam epitaxy [110]. In that experiment S was decreased by lowering the substrate temperature during growth, maintaining the values of M_{s} and A, whilst $K_{\perp}$ dropped precipitously. This led to a marked expansion in wall thickness and a loss of DW MR, the opposite trend with S to that in the samples presented here.

IV .2.2.2 Spin-dependent scattering and diffusive current spin polarization

The DW MR data were treated within the LZ spin-mixing model[26]. In this model the resistivity due to DW scattering for both current-perpendicular and current-parallel to the Bloch-type DW is expressed explicitly as a function of the spin-asymmetry parameter α, [26, 87, 20, 86, 14, 22] and spin mistracking parameter ξ, defined below. It uses the same Hamiltonian that governs giant magnetoresistance as outlined in section II .1.1 and employs a scattering potential

$$V_{\mathrm{scattering}}(\mathbf{r}) = \sum_{i} \left[v(\mathbf{r}) + j(\mathbf{r}) \sigma \cdot \hat{\mathbf{M}}(\mathbf{r}) \right] \delta(\mathbf{r} - \mathbf{r}_i) \qquad \text{(IV .9)}$$

to describe the spin-dependent electron scattering, with impurity potential $v(\mathbf{r})$ at position $\mathbf{r}_i$, where $j(\mathbf{r})$ denotes the spin dependence of the electron

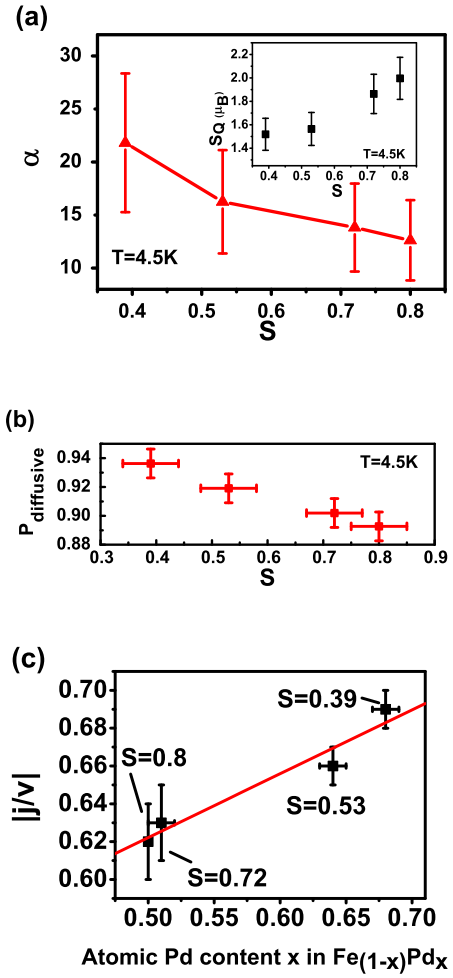

Figure IV .15: The diffusive spin asymmetry parameter α vs. chemical long range order parameter S (a) from DWR data and OOMMF simulations. The inset shows the dependence of the average moment per atom S_{Q} on the order parameter S. The diffusive spin asymmetry parameter α was converted directly into a current spin polarization valid for the diffusive electron transport regime (b) as outlined in equation IV .3 in the text. Despite high diffusive spin polarizations $P_{\mathrm{diffusive}}$ one obtains an increasing trend with lower chemical long range ordering parameter S reflecting the α dependency shown in (a). Figure (c) depicts the evolution of the spin dependent exchange scattering of a conduction electron normalized to its Coulomb scattering j/v on elemental Pd content in $\mathrm{L1_0\text{-}Fe_{(1-x)}Pd_x}$ as detailed in the spin dependent scattering potential used in the Levy-Zhang theory Equation IV .9. The ratio $|j/v|$ was evaluated from α and Equation IV .16.

scattering, σ represents the Pauli-matrices and $\hat{\mathbf{M}}(\mathbf{r})$ is the unit vector along the direction of the local magnetization. Henceforth, for simplicity in notation we write α for the diffusive spin-asymmetry in conductance.

While one measures the MR of the entire film, the LZ model describes the MR only where magnetization gradients exist, i.e. the DWs. Hence it is necessary to account for the domain pattern of the films. The OOMMF micromagnetics code [117] was used to calculate a representative distribution of $\hat{\mathbf{M}}(\mathbf{r})$ from the experimental values of A, $K_\perp$, and M_s for a 1×1 μm^2 slab representing each of the four samples. The mesh used had cells 1 nm $\times$ 1 nm in the plane and 15 nm deep. An example of a simulated domain pattern is shown in figure IV .14(a). From this we calculate $\Theta = \arccos(M_z/M)$ and the local magnetization gradient $\nabla\Theta$, which determines the local strength of the spin mistracking $\xi = \hbar^2 \nabla\Theta \cdot \mathbf{k}_\mathrm{F}/4mJ$, where $\mathbf{k}_\mathrm{F} \approx 2$ Å^{-1} is the Fermi wavevector, J is the Stoner exchange splitting, and m the free electron mass as an approximation for the effective electron mass. The direction of electric current represented by $\mathbf{k}_\mathrm{F}$ was used in order to decompose the current into components that are parallel (CIW) and perpendicular (CPW) to the magnetic domain wall as it meanders in order to calculate the local DW MR for a 1×1 μm^2 slab according to

$$\frac{\Delta\rho}{\rho} = \frac{(\xi)^2}{5}\cos^2(\beta)F_\mathrm{CPW}(\alpha) + \frac{(\xi)^2}{5}\sin^2(\beta)F_\mathrm{CIW}(\alpha), \qquad \text{(IV .10)}$$

where β is the angle between $\nabla\Theta$ and $\mathbf{k}_\mathrm{F}$. This type of angular dependence was recently confirmed experimentally by Aziz et al. [22]. $F_\mathrm{CIW}(\alpha)$ and $F_\mathrm{CPW}(\alpha)$ describe the α-dependence of the DW resistivity, and were taken as defined by Levy and Zhang [26, 14].

A computational result of the local DW MR determined based on equation

Table IV .2: Spin conductance asymmetry parameter α and the diffusive current spin polarization $P_{\text{diffusive}}$ in direct comparison to the absolute value of the normalized conduction electron exchange scattering j/v for the four $L1_0$-$Fe_{1-x}Pd_x$ epilayers studied. The stoichiometric Pd content x was determined from XPS analysis and related to the crystallographic long range order parameter S. The ballistic current spin polarization $P_{\text{ballistic}}$ as evaluated in Andreev point contact spectroscopy is tabulated as well for reasons of completeness.

S	x	α	$P_{\text{diffusive}}$	$\lvert j/v \rvert$	$P_{\text{ballistic}}$
0.39 ± 0.05	0.68 ± 0.01	22 ± 6	0.94 ± 0.05	0.69 ± 0.01	0.50 ± 0.05
0.53 ± 0.05	0.64 ± 0.01	16 ± 5	0.92 ± 0.05	0.66 ± 0.01	0.53 ± 0.05
0.72 ± 0.05	0.51 ± 0.01	14 ± 4	0.90 ± 0.04	0.63 ± 0.02	0.50 ± 0.05
0.80 ± 0.05	0.5	13 ± 4	0.89 ± 0.04	0.62 ± 0.02	0.49 ± 0.11

IV .10 and the local magnetization of figure IV .14 (a) is shown in figure IV .14(b) and this procedure was performed for all four samples (see figure IV .15 (a)) based on the micromagnetic simulation results shown in figure IV .11 (e)-(h). The lateral resolution of this DW MR map is equivalent to the micromagnetic simulation which is based on the Landau-Lifshitz-Gilbert formalism and shown in (a) of the same figure, i.e. 1 nm $\times$ 1 nm. The darker contrast outlines the magnetic domain walls representing significantly enhanced local resistivity due to the process of spin-mixing in the region of rotating localized spins of a magnetic domain wall. Integrating over the entire region according to an equipotential summation algorithm (analogous to the mean of the Voigt and Reuss averages in the Young's modulus of a composite [119]), with ρ fixed to the value for the film of interest, yielded the total simulated DW MR. The value of α was varied in an iterative process until the overall DW MR matched the measured value, see figure IV .15 (a). For the best ordered sample one obtains a value of $\alpha \approx 12$ similar to those found previously in both MBE-grown FePd [14] and sputtered FePt as discussed in IV .2.1 and [87]. The value of α rises as the Pd enrichment degrades the $L1_0$-ordering, roughly to about 21. It is pointed out that in literature obtainable on similar systems, values for α for scattering from Pd impurities in Fe are not available, although the isoelectronic elements Ni and Pt show values of $\alpha \approx$ 7-8 [120].

Whilst elemental Fe is a weak ferromagnet, FePd has enough electrons to be a strong ferromagnet, consistent with higher values of α. Adding Pd in turn adds electrons, pushing the Fermi level higher still above the top of the majority *d*-band. Accounting for the DW dilution on the approximate basis as

used in references [87] and [14] returned values of α indistinguishable within the error bar, which was based on propagating any relative uncertainties in all the input parameters. A uniform current distribution has been assumed with the current flowing from left to right in straight and direct paths with the momentum relaxation occurring much faster than the process of spin mixing. Here, the value of $J = 1$ eV from a band structure calculation of a perfect crystal [121] was used. The inset to figure IV .15 (a) shows S_{Q}, the average moment per atom derived from the low temperature M_{s} data vs. S indicating that additional Pd atoms do not exert their spin dependence of scattering via an enhanced localized moment.

One proceeds to compute the current spin polarizations of the diffusive transport regime from $P_{\mathrm{diffusive}} = \frac{\alpha-1}{\alpha+1}$ (see also equation IV .3), and the results are plotted in figure IV .15 (b). All the samples have $P_{\mathrm{diffusive}} \sim$ 90-95 %, with the more highly polarized currents flowing in the less ordered samples. However, $P_{\mathrm{diffusive}}$ depends only weakly on S.

To understand the effect of excess Pd scattering centers one directly derives an expression for α in terms of the spin dependence of scattering j from the LZ model. Essentially, the spin-channel conductivity ρ^{σ} representing $\rho^{\uparrow(\downarrow)}$ is a function of the spin-dependent scattering time $[\tau^{\sigma}(\mathbf{k})]^{-1}$ considering that the spin-dependent Fermi $\mathbf{k}$-vectors do not differ in absolute value in a first order approximation. Hence, $\rho^{\sigma} \propto [\tau^{\sigma}(\mathbf{k})]^{-1}$ and one can resort to evaluating the ratio of the spin-dependent scattering rates in order to obtain the ratio α of the resistivities in both Mott channels. The conductance of the magnetic domain wall in the current-in-wall (CIW) geometry, i.e., the current flows

parallel to the wall, is expressed as

$$\sigma = \frac{e}{8\pi^3}\sum_{\sigma}\int \frac{n^{\sigma}(\mathbf{k})}{|\mathbf{E}|}\frac{\hbar k_y}{m^*}\delta(E_F-\epsilon_{\mathbf{k}\sigma})d^3\mathbf{k} \quad \text{(IV .11)}$$

$$= \frac{e^2}{16\pi^3}\sum_{\sigma}\int \left(\frac{\hbar k_y}{m^*}\right)^2 \tau^{\sigma}(\mathbf{k})\delta(E_F-\epsilon_{\mathbf{k}})d^3\mathbf{k}, \quad \text{(IV .12)}$$

with $n^{\sigma}(\mathbf{k})$ denoting the spin density of states and m^* the effective electron mass.

One then evaluates the spin-scattering rates in the limit of an infinite magnetic wall thickness by solving the Boltzmann equation[122] from

$$[\tau^{\sigma}(\mathbf{k})]^{-1} = \frac{\Omega n^{\sigma}(\mathbf{k}')}{4\hbar\pi^2}\int d^3\mathbf{k}'|V^{\sigma\sigma}_{\mathbf{k}'k}|^2\delta(\epsilon_F-\epsilon_{\mathbf{k}'\sigma})+\ldots$$
$$\ldots+|V^{\sigma-\sigma}_{\mathbf{k}\mathbf{k}'}|^2\delta(\epsilon_F-\epsilon_{\mathbf{k}'-\sigma}), \quad \text{(IV .13)}$$

based on the matrix elements of the scattering potentials $V^{\sigma\sigma}_{\mathbf{k}'\mathbf{k}}$ and $V^{\sigma-\sigma}_{\mathbf{k}\mathbf{k}'}$. This yields an expression in terms of the spin-dependent Fermi vector $k_{F\sigma}$ and the electron density of states of the spin-split Fermi surface $N_{\sigma}(E_F)$ that reads $[\tau^{\sigma}(\mathbf{k})]^{-1} = \frac{1}{3}k^2_{F\sigma}N_{\sigma}(E_F)$.

Integration over reciprocal space gives

$$[\tau^{\sigma}(\mathbf{k})]^{-1} = c_i\frac{2\pi}{\hbar}\left((v+\sigma j)^2\left((1-\frac{\xi^2}{k_F^2}k_x^2)N_{\sigma}(E_F)-\frac{\xi^2}{k_F^2}\frac{1}{3}k^2_{F\sigma}N_{\sigma}(E_F)\right)\right)+\ldots$$
$$\ldots+c_i\frac{2\pi}{\hbar}\left(\frac{\xi^2}{k_F^2}\left((v+\sigma j)^2\frac{1}{3}k^2_{F-\sigma}N_{-\sigma}(E_F)+(v-\sigma j)^2k_x^2N_{-\sigma}(E_F)\right)\right)\cdot$$
$$\cdot\frac{c_i2\pi}{\hbar}\left((v+\sigma j)^2N_{\sigma}(E_F)\cdot\left(1-\frac{\xi^2}{k_F^2}(k_x^2+\frac{1}{3}k^2_{F\sigma})+\frac{\xi^2}{k_F^2}+\ldots\right.\right.$$
$$\left.\left.\ldots+\frac{\xi^2}{k_F^2}\left(\frac{1}{3}k^2_{F-\sigma}+\frac{(v-\sigma j)^2}{(v+\sigma j)^2}k_x^2\right)\frac{N_{-\sigma}(E_F)}{N_{\sigma}(E_F)}\right)\right). \quad \text{(IV .14)}$$

Here c_i refers to the concentration of impurity sites and $c_i\Omega = \sum_i 1 + \sum_{i\neq j}e^{i(\mathbf{k}'-\mathbf{k})\cdot(\mathbf{r}_i-\mathbf{r}_j)}$ is an average counting over all of the impurity sites where

each site is taken to be of equivalent weighting. Taking the limit for infinite wall width, which amounts to taking the limit of $\xi \to 0$, one finds the ratio in the unperturbed spin-dependent resistivities, the quantity relating to the Mott spin-channel conductance asymmetry α as the ratio of ρ_0^{σ}. Consequently, one obtains the expression

$$\left(\frac{v-\sigma j}{v+\sigma j}\right)^2 = \frac{\rho_0^{-\sigma} k_{F-\sigma}^2}{\rho_0^{\sigma} k_{F\sigma}^2} = \alpha, \qquad \text{(IV .15)}$$

directly leading us to a closed form of α in terms of the spin-dependent exchange scattering of a conduction electron passing through a magnetic domain wall normalized to the strength of pure Coulomb scattering,

$$\alpha = \left(\frac{(j/v)-1}{(j/v)+1}\right)^2, \qquad \text{(IV .16)}$$

where v and j are as defined for equation IV .9 [122]. Essentially, the rise in DW MR with increased disorder is due to a rise in α as elaborated above. Simultaneously, equation IV .16 means that a change in $|j/v|$ - the ratio of exchange scattering strength to Coulomb scattering strength ensemble averaged over the film - causes α to vary accordingly.

To gain further insight into the microscopic picture of this phenomenon, it was resorted to x-ray photoelectron spectroscopy (XPS) analysis of the $L1_0$-$Fe_{(1-x)}Pd_x$ films. Furthermore, the atomic Pd fraction x was related to the crystallographic long range ordering in the four samples S. Evaluating the average of $|j/v|$ from α determined for each sample, see table IV .1, the fractional change of $|j/v|$ with S agrees very well with the change in the ratio of Pd to Fe content as illustrated in figure IV .16. In first approximation, the absolute value of j/v exhibits a linear dependence on the stoechiometric Pd fraction x in the binary alloy $Fe_{(1-x)}Pd_x$ providing strong evidence that

atomic Pd enhances the spin dependent scattering strength in the samples, see figure IV .15 (c). More precisely, excess Pd atoms in the form of interstitial impurities or anti-site defects act as additional spin-dependent scattering centres that essentially spin-polarize the current.

IV .3 Ballistic electron transport properties

IV .3.1 Transport in the ballistic regime $L1_0$-ordered FePt

A common method in order to determine the current spin polarization of a metallic material is to perform point contact Andreev reflection spectroscopy measurements (PCAR)[56]. Central in this electron transport measurement is that for applied bias voltages within the energy gap of the superconductor, it is physically impossible to inject or extract single electrons, but only Cooper pairs. More precisely, it is the coherent back reflection of a charge carrier hole into the ferromagnetic sample upon forming a Cooper electron pair of opposite spin orientations inside the superconducting Nb tip, and hence, the number of unpaired electrons in the ferromagnet in the immediate vicinity of the ferromagnetic material around the superconducting tip, that makes feasible the direct probing for the ballistic current spin polarization of the ferromagnetic metal under consideration. One then applies the modified Blonder-Tinkham-Klapwijk theory [52, 55] to evaluate a bulk material value of the current spin polarization in the ballistic electron transport regime. A typical conductance spectrum taken by PCAR on $L1_0$-FePt is shown in figure IV .16. As also displayed in figure IV .16, the data were corrected

from the contribution of spreading resistances within the film, as deduced from measurements. Spreading resistances are commonly found when the resistances of the point contact (of around 10 Ω in this case) are of the same order of magnitude as the resistance of the film (here around 3.5 Ω), and a strong indicator thereof is that the superconducting gap is significantly expanded. It is then necessary to correct both voltage bias and differential conductance data for this additional series resistance [93]. However, the effect of correction on polarization is not large in the present case, since the ratio of sub-gap to quasi-particle conductance never strays too far from unity at any value of bias, due to the polarization is being close to 50 %. From the typical resistances of the point contacts ranging between 4 and 15 Ω, and using the Sharvin formula, an effective point contact characteristic size of around 5 to 15 nm [94, 93] was calculated. Such a value is much smaller than the characteristic micron-size of the terminated apex of the tip, as measured by scanning electron microscopy. Indeed, as it is usually the case, the contact results in multiple effective nanometric point contacts [94], where electron transport across the ferromagnet-superconductor interface is ballistic. The conductance vs. bias voltage data were fitted in the standard way, employing a modified Blonder-Tinkham-Klapwijk (BTK) model [52], which describes the crossover from metallic to tunnel junction behavior of a micro-constriction contact between a semiconductor and a superconductor based on the Bogoliubov equations. Four numerical fitting parameters[55, 94] are employed to fit the measured conductance curves and thus determine the bulk current spin polarization of the sample: the effective temperature, T_{eff}; the barrier strength, Z, which accounts for the cleanness of the interface (e.g.

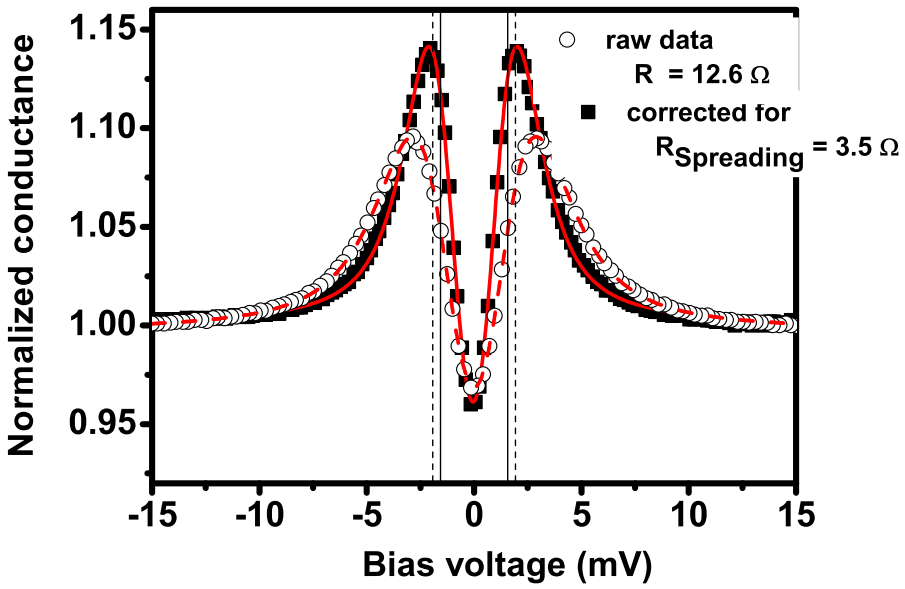

Figure IV .16: Normalized conductance vs. bias voltage as obtained by point contact Andreev reflection (PCAR) at $T = 4.2$ K before (circles) and after (squares) correction from the spreading resistance as defined in the text, together with the respective fits according to the modified BTK model (dashed and continuous lines). The fitting parameters are discussed in the text and given in the following figure. The vertical lines indicate the values of the deduced gaps before (dashed line) and after (continuous line) correction (graph courtesy of V. Baltz).

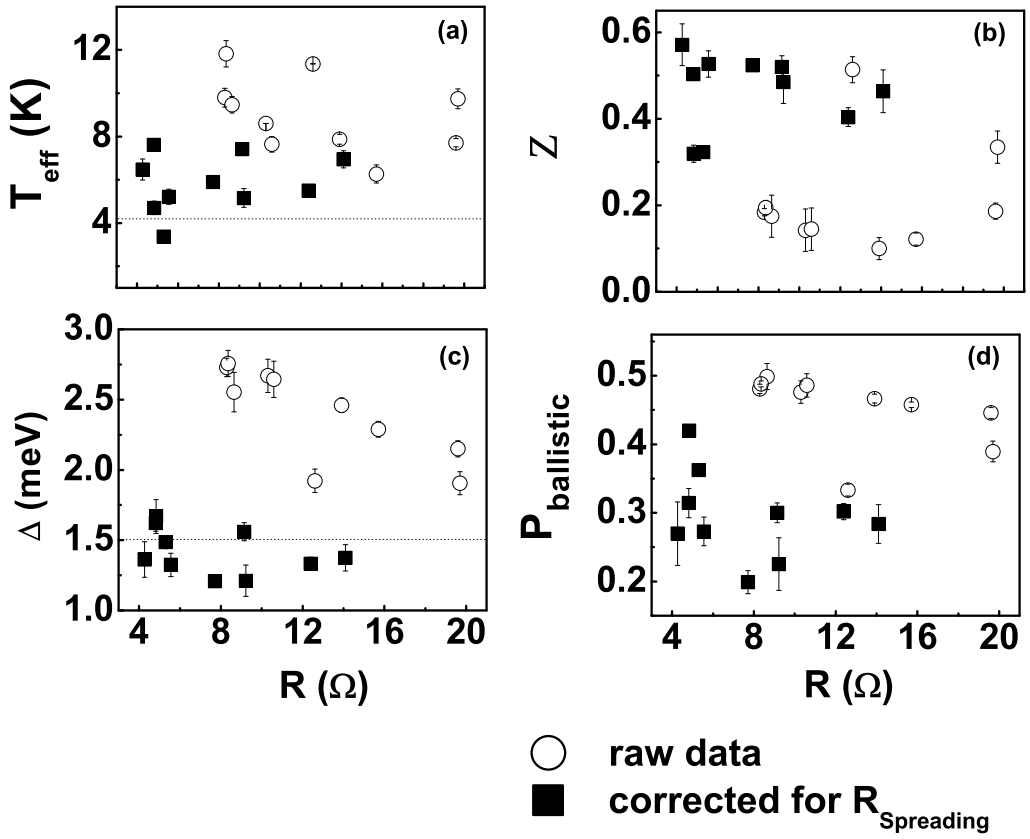

Figure IV .17: Dependence of the fitting parameters employed in the modified BTK model, and described in the text, with the point contact resistance. The dashed line in (a) points out the boiling point of liquid helium at $T = 4.2$ K. The dashed line (c) marks the superconducting gap parameter $\Delta \approx 1.5$ meV of bulk niobium (graph courtesy of V. Baltz).

an infinite Z accounts for a tunnel transport regime); the superconducting gap, Δ ($\sim$ 1.5 meV for elemental bulk niobium); and the spin polarization $P_{\text{ballistic}}$. The dependence of the fitting parameters on the point contact resistance (R) are plotted in figure IV .17, among with the resulting fits of the raw data, for comparison. From the data shown in figure IV .17(a), it can be seen that on average T_{eff} is larger than the 4.2 K real temperature of the experiment. Such differences between effective and real temperatures have been reported before [55, 116, 94] and are ascribed to weaknesses in the model since T_{eff} not only accounts for thermal activation but also includes other effects that result in a broadening of the Fermi-Dirac function such as the electron Fermi velocity mismatch between the tip and the sample or the presence of a thin remaining oxide layer at the surface. Moreover, this can also represent any spread in the properties of different parallel nanocontacts formed by the tip and sample. To avoid confusion, T_{eff} is sometimes referred to in the literature as a broadening factor. From the data shown in figure IV .17(b), it can be seen that for a given tip, there is no clear correlation between the point contact resistance and Z. It had been ascribed to the fact that for contacts of the same nature, R is mainly determined by the size of the contact rather than its cleanness [55]. As observed in figure IV .17(c), the values of the tips' superconducting gaps are in agreement with those of the bulk Nb. Note that the initial large values of the superconducting gap as deduced from fits of the raw data are indeed the signature of spreading resistances. Figure IV .17(d) shows that the spin polarization does not depend on R in an easily observable way. Rather note that the fitted spin polarization seems to systematically depend on Z. Here one finds an acceptable

agreement with a quadratic reduction in $P_{\text{ballistic}}$ with Z [55, 92], as shown in figure IV .18. The relevant value of the spin polarization is known to be the one extrapolated in the case of a perfectly transparent interface (i. e. when $Z = 0$). One finds a ballistic spin polarization of $P_{\text{ballistic}} = (0.42 \pm 0.05)$ for the $L1_0$-FePt film under investigation. This value serves as a reference obtained by a conventional tool to asses the spin polarization of a current, i.e. the ballistic version of the current spin polarization. Comparing $P_{\text{ballistic}}$ directly with $P_{\text{diffusive}} = 0.88 \pm 0.02$ determined at $T = 4.2$ K by DWR measurements in conjunction with the L-Z model, one notices a discrepancy of approximately a factor of 2. Both values were evaluated on one and the same $L1_0$-FePt sample. A more thorough discussion of the underlying physical aspects of this phenomenon is given in chapter V . It is emphasized that one obtains similar values of the polarization when one does not apply any correction for the spreading resistance in the FePt film [93]. This value is moreover close to that reported for elemental iron using the same technique, i.e. $P_{\text{ballistic}} = 0.46 \pm 0.03$ [116]. A very similar value was measured for a pure Fe film explicitly using the very same experimental set-up as in this study, and also shown that it yields a polarization of zero for nonmagnetic materials such as Au. It is also pointed out, that one obtains the same value, to well within the error bar, when analyzing data taken on the sample in the remanent state or in the ac demagnetized state (PCAR data not shown). As the contact areas are ~ 10 nm and the domains are ~ 170 nm of width, the likelihood of any given contact touching a wall in the demagnetized film is rather low. Hence most of the data points that have been used to perform the extrapolation are made to uniformly magnetized regions in both cases, and

one would not expect any significant difference arising by this means. Moreover, this method is sensitive only to the magnitude and not the direction of the spin polarization. What is important to notice is that this comparison shows that the effect of any stray fields due to the domain structure on the superconductivity of the tip is negligible.

IV .3.2 Transport in the ballistic regime $L1_0$-ordered FePd

The same set of $L1_0$-$Fe_{(1-x)}Pd_x$ samples used to study the domain wall magnetoresistance and the diffusive current spin polarization as described in IV .2.2.1 and in IV .2.2.2 was also employed to investigate the ballistic current spin polarization by conventional point contact Andreev spectroscopy (PCAR). The experiments on $L1_0$-$Fe_{(1-x)}Pd_x$ samples were performed in an identical manner as in the case of $L1_0$-FePt described in the previous section IV .3.1, Methodic details are described in III .7.

Figure IV .19 illustrates the ballistic current spin polarizations $P_{\text{ballistic}}$ obtained from PCAR measurements using a Nb tip at 4.2 K, the boiling point of liquid helium, interpreted within the usual extended Blonder-Tinkham-Klapwijk (BTK) model. It details the interdependence of two of the fitting parameters $P_{\text{ballistic}}$ and the interface transparency parameter Z^2 for sequential contacts on all four FePd films. The extrapolation of the least-square fit to the case of a transparent interface ($Z^2 = 0$) yields the value of the bulk spin polarization, approximately $P_{\text{ballistic}} = 0.5$ for all four samples, with no noticeable trend with S[90, 54, 53, 55, 91, 92, 23]. For the accurate values of $P_{\text{ballistic}}$ for each sample of varying degree of crystallographic

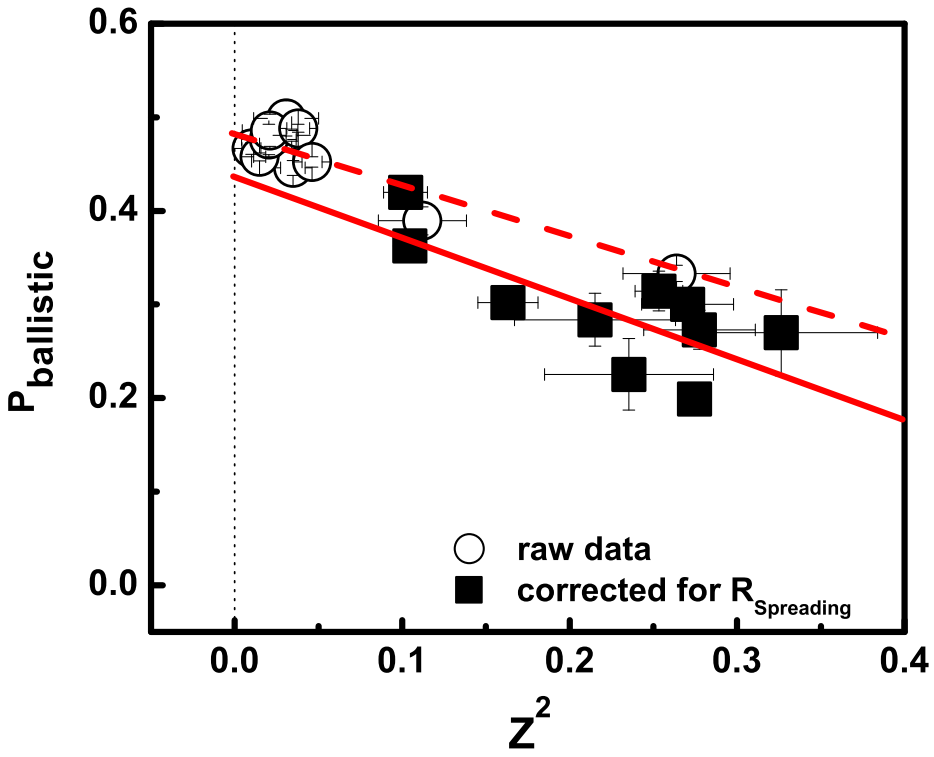

Figure IV .18: Ballistic current spin polarization vs. square of the superconductor-ferromagnet interface transparency parameter Z for $L1_0$-ordered FePt. The extrapolation of the least-squares fit (lines) onto the ordinate gives the bulk spin polarization of the current (graph courtesy of V. Baltz).

ordering see table IV .2. A scattering barrier at the metal/superconductor interface, which causes additional interfacial spin-scattering effects and thus diminishes the intrinsic polarization of the bulk material, accounts for the decreasing tendency of $P_{\text{ballistic}}$ with Z [55]. The details of the experimental and fitting procedures are identical to those described in III .7, IV .3.1 and Ref. [87]. The basis for the BTK fitting procedures is depicted in the inset of figure IV .19 as an example of a typical conductance curve obtained in a PCAR measurement after correction for a spreading resistance, an parasitic ohmic resistance contribution arising from the sheet film resistivity intrinsic to the $L1_0$-$Fe_{(1-x)}Pd_x$ samples [93]. Multiple PCAR spectra of this sort were collected for each of the samples with the resistance of the nano-sized contact between superconducting niobium tip and the ferromagnetic film ranging from 3-9 Ω. All four BTK fitting parameters are depicted as a function of the point contact resistance (R), also serving as a feature to distinguish between the individual contacts achieved, are plotted in figure IV .20 in separate panels (a), (b), (c) and (d) as an example for the $L1_0$-FePd sample with crystallographic long range order parameter $S = 0.53$. The broadening energy parameter ω is consequently larger than $\omega \approx 0.36$ meV, the energy equivalent to the boiling temperature of liquid helium $T = 4.2$ K, held as the real temperature of the experiment as illustrated in figure IV .20 (a) [55, 116]. This is due to thermal activation but also includes other effects that result in a broadening of the Fermi-Dirac function such as the electron Fermi velocity mismatch between the tip and the sample or the enhanced interface scattering based on the presence of a thin remaining oxide layer at the surface. Secondly, a spread in the properties can arise also from different

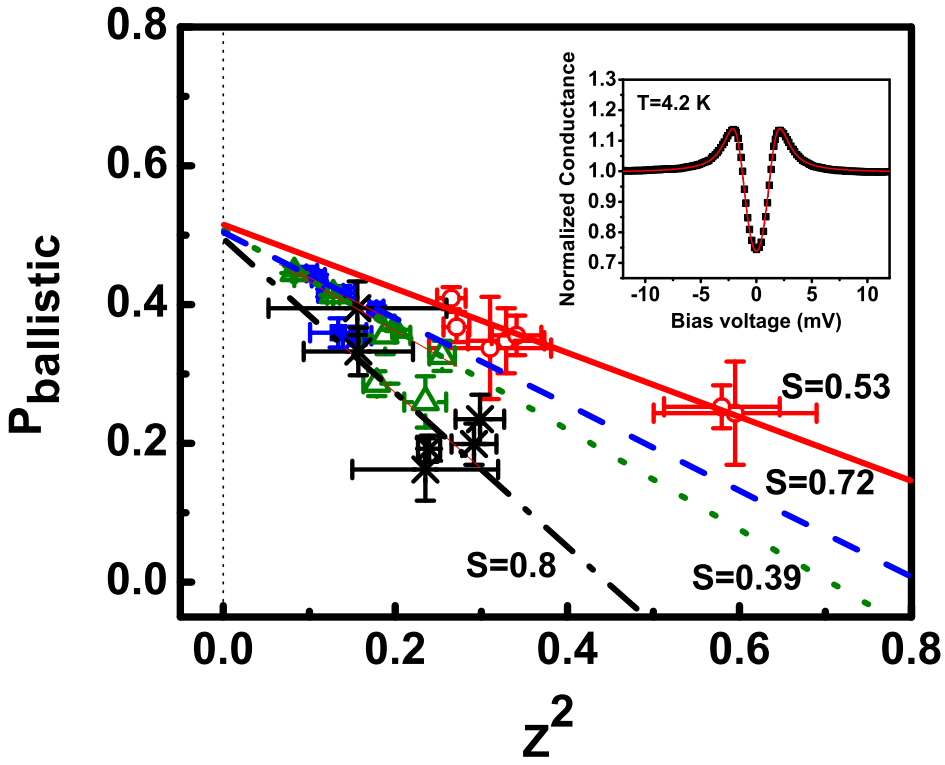

Figure IV .19: Ballistic current spin polarization vs. square of the superconductor-ferromagnet interface transparency parameter Z for $L1_0$-ordered FePd. The extrapolation of the least-squares fit (lines) onto the ordinate gives the bulk spin polarization of the current. The inset shows the normalized conductance vs. bias voltage spectrum as obtained by point contact Andreev reflection (PCAR) at $T = 4.2$ K together with the respective fit according to the modified BTK model. The fitting parameters are discussed in the text and one example of a set BTK-fitting parameters is given in the following figure (graph courtesy of V. Baltz).

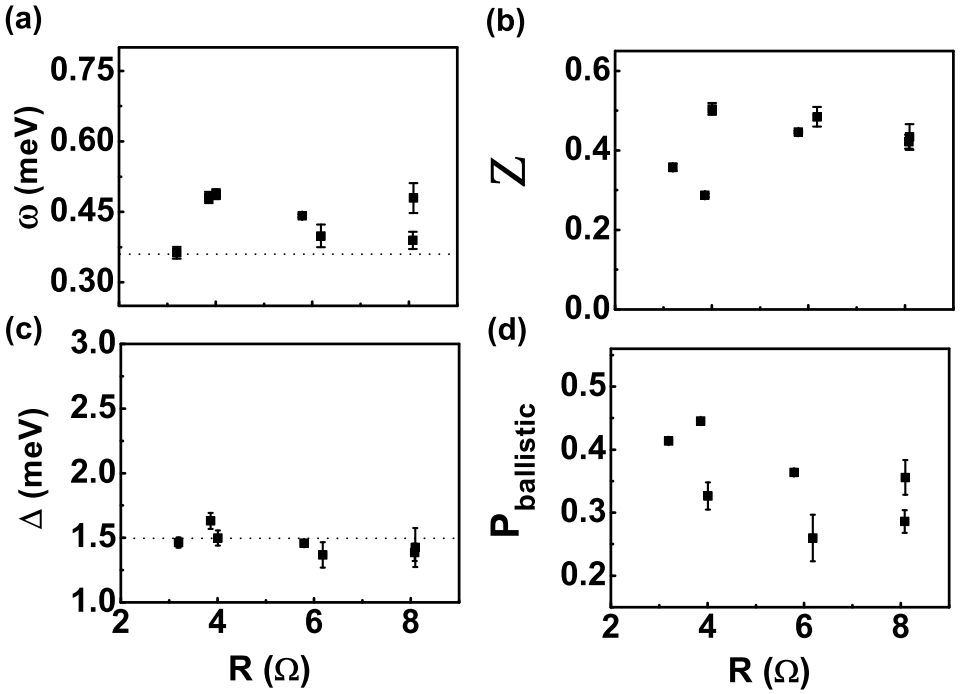

Figure IV .20: Dependance of the fitting parameters employed in the modified BTK model on the point contact resistance., i.e., the broadening energy parameter ω shown in (a), the barrier strength Z in (b), the superconducting gap parameter Δ (c) and $P_{\text{ballistic}}$ plotted in (d) as further described in the text. The dashed line in (a) points out $\omega \approx 0.36$ meV equivalent to the boiling point of liquid helium at $T = 4.2$ K. The dashed line (c) marks the superconducting gap parameter $\Delta \approx 1.5$ meV of bulk niobium (graph courtesy of V. Baltz).

parallel nanocontacts formed by the tip and sample. Moreover, according to the data shown in figure IV .20(b), for one and the same niobium tip, there is no clear dependence of the point contact resistance R and Z. This indicates that R is mainly determined by the size of the contact rather than its interfacial scattering strength as long as the contact size ranges within the Sharvin limit [55, 87]. The most prominent parameter and as such a hallmark for an appropriate application of the modified BTK model to the conductance spectra collected by PCAR experiments is the superconducting gap Δ, which typically yields approximately $\Delta = 1.5$ meV for a superconducting tip made from elemental niobium. Figure IV .20(c) illustrates that the values of superconducting energy gaps presented are in very good agreement with those of the bulk Nb (dashed line) after subtracting the parasitic sheet film resistance intrinsic to the FePd material. It is noteworthy, that the initial large values of the superconducting gap as deduced from fits of the raw data are indeed the signature of spreading resistances. Finally, turning to the value of the ballistic current spin polarization itself as detailed in Figure IV .20(d), it is obvious that spin polarization exhibits a non-trivial dependence the contact resistance R between tip and sample. However, the contact resistance translated into a interface scattering strength Z in conjunction with the obtained spin polarization values $P_{\text{ballistic}}$ for each contact of an individual FePd sample yield a systematic dependence on Z. Especially a quadratic reduction in $P_{\text{ballistic}}$ with Z [55, 92] as shown in figure IV .19 results in an easily extrapolated function to $Z = 0$ in order to obtain the bulk value of $P_{\text{ballistic}}$ for each of the four $L1_0$-$Fe_{(1-x)}Pd_x$ samples as listed in table IV .2 together with $P_{\text{diffusive}}$. Figure IV .21 visualizes the current spin polariza-

tions for both transport regimes investigated in this work, i.e. the diffusive (a) and the ballistic electron transport regime (b) as a function of crystallographic long range ordering within the $L1_0$-$Fe_{(1-x)}Pd_x$ films studied. On the one hand, $P_{\text{ballistic}}$ does not exhibit any dependence on the crystallographic long range ordering S in $L1_0$-$Fe_{(1-x)}Pd_x$ films within the error considerations. This is also not expected as the $L1_0$-phase was maintained in all four samples such that $L1_0$-$Fe_{(1-x)}Pd_x$ remains a strong ferromagnet. Consequently no significant change in band structure properties are at stake to give rise to a change in $P_{\text{ballistic}}$. However, a trend in $P_{\text{diffusive}}$ with S is observed indeed as additional scattering centres are introduced that enhance spin-dependent scattering but lower S, visible in figure IV .15 (b) or in figure IV .21 (a). It is also striking that, as in the case of $L1_0$-FePt discussed in IV .3.1, the discrepancy between diffusive and ballistic current spin polarization amounts approximately to a factor of 2. PCAR in conjunction with the BTK-model is generally accepted as a standard method to determine the current spin polarization of a conducting material, i.e. the ballistic version of the current spin polarization. Hence, the difference between $P_{\text{ballistic}}$ and $P_{\text{diffusive}}$ must be explained by spin-dependent electron scattering involving a discrepancy in the product of spin-relaxation time and Fermi-velocity for each Mott spin-channel $v_{\text{F}}^{\uparrow(\downarrow)} \cdot \tau_{\uparrow(\downarrow)}$, see also equations IV .3, IV .4 and IV .5. It is important to note at this point, that a direct comparison between both polarization values is appropriate in this case, as DW magneto-transport as well as PCAR experiments have been performed at the very same temperature $T = 4.5$ K.

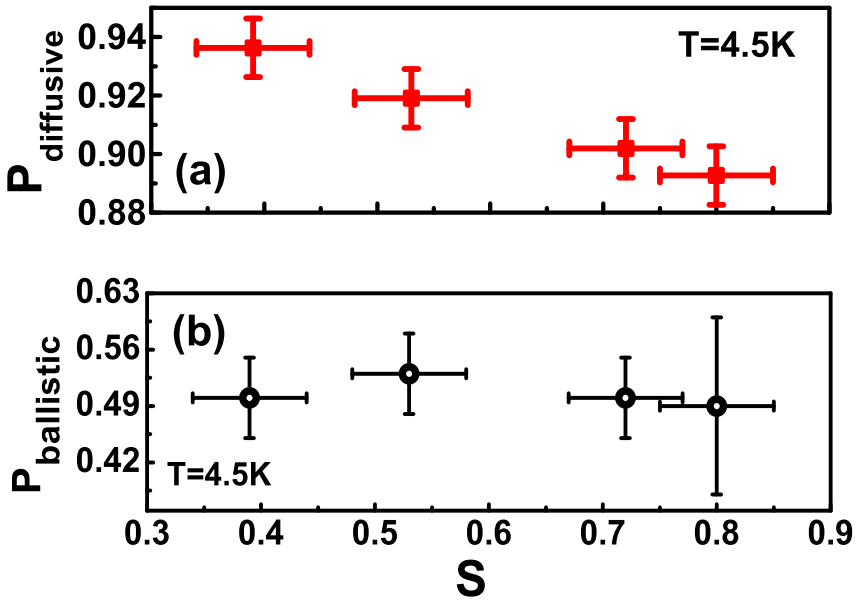

Figure IV .21: Comparison of the current spin polarization for various chemical order parameters of $L1_0$-phase FePd in both the diffusive (a) and the ballistic (b) transport regimes. Error bars in S are derived from the analysis of the x-ray diffraction data. The data in (a) are derived from α values, error bars arising from the propagation of errors through the data analysis. The data in (b) are derived from PCAR measurements, the error bars representing the typical sample-to-sample spread for the PCAR apparatus as derived from measurements of a series of nominally identical Fe samples.

IV .4 Anomalous Hall effect in epitaxial $L1_0$-ordered FePd and the isoelectronic compound FePt

The anomalous or spontaneous Hall effect (AHE) [45] in a ferromagnetic material has the most remarkable property, that it increases strongly with temperature. The two basic but in their nature different effects leading to AHE are side-jump and skew scattering mechanism, yet both are commonly understood to be a consequence of the spin-orbit interaction acting on a conduction band electron[63, 65, 66, 64]. While there are theoretical predictions [123] that both mechanisms, side-jump scattering and skew scattering are present in a conventional ferromagnetic material such as Fe, experimental evidence is provided in this work, that in an epitaxially ordered metallic system of high diffusive current spin polarization effectively only skew scattering contributes to AHE.

Other physical phenomena such as domain wall resistance[14, 23] of $L1_0$-ordered FePt and FePd have received in-depth investigation before, see IV .2.1 and IV .2.2. However a direct comparison between $L1_0$-ordered FePt and FePd with respect to AHE has not been undertaken, although this effect was a research topic in the past [124, 110, 19, 125]. In this work, the underlying physical effect of spin-orbit scattering in $L1_0$-ordered FePt and FePd is investigated, especially the elucidation of the role of the non-ferromagnetic but otherwise isoelectronic atomic species Pd and Pt with respect to the strength of spin-orbit interaction within these binary and monocrystalline alloys is of interest. According to J. Smit [66], but also A. Crépieux et al. [67] the

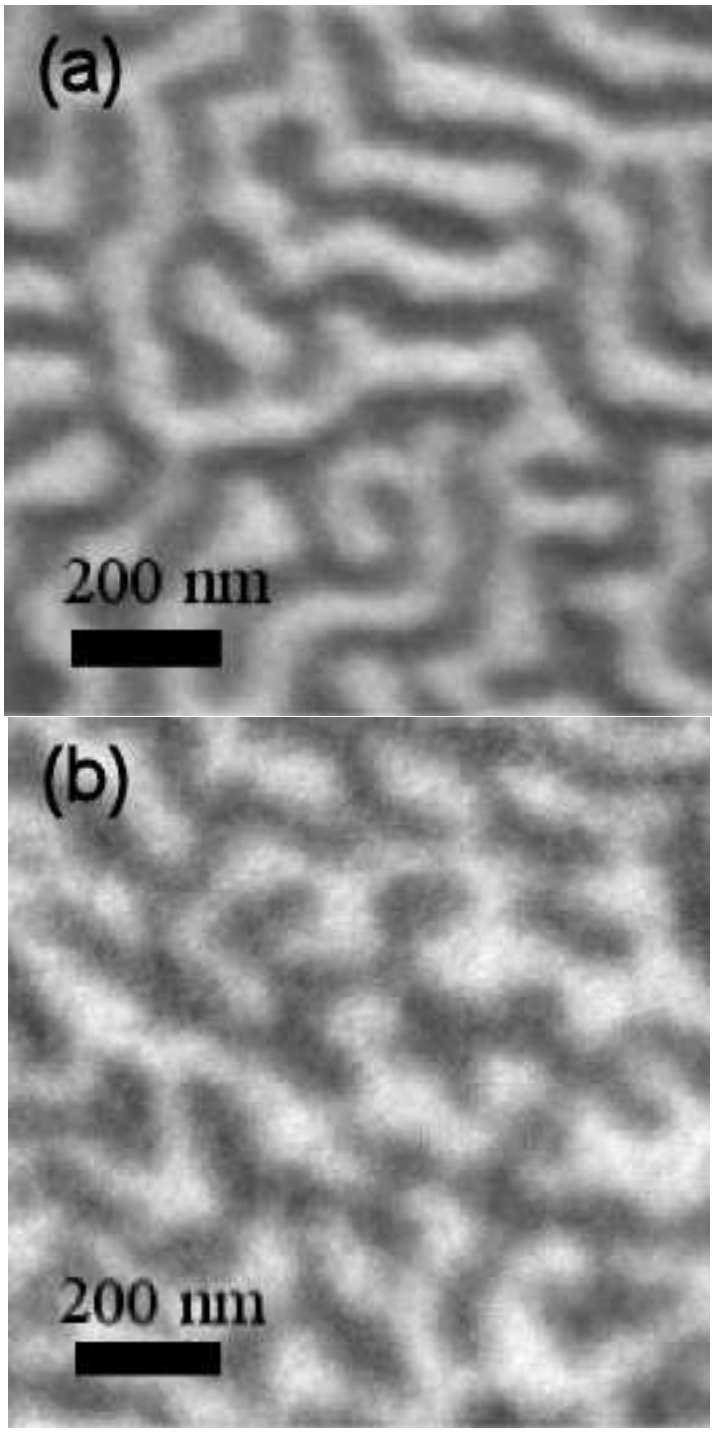

Figure IV .22: 1 μm $\times$ 1 μm area XMCD-PEEM images (top view) of the room temperature demagnetized domain state of (a) $L1_0$-ordered FePd and (b) FePt films in zero magnetic field. Dark and bright areas depict magnetic domains of opposite orientated magnetization perpendicular to the film plane (XMCD-PEEM images courtesy of J. Miguel, F.Kronast and W. Kuch, BESSY Berlin).

spin-orbit perturbation Hamiltonian describes the spin-orbit interaction of a conduction electron in the presence of a perturbation potential V with atomic spin-orbit energy λ as decribed in equations II .24, II .26 and equation IV .17 respectively. As V and λ are expected to increase substantially with a heavier atomic scattering center, the exchange of Pd (average atomic mass $Z_{Pd} = 106$) with the isoelectronic atomic species Pt (average atomic mass $Z_{Pt} = 195$) is expected to increase spin-orbit scattering and consequently should also enhance the resulting spontaneous Hall voltage.

Hall experiments were performed which revealed an absence of the electronic side-jump mechanism. Thus one is able to directly determine the angle of deflection of the electron trajectories in a single spin-orbit scattering event, i.e. the skew scattering angle Φ_{SK}.

The basis for these experiments are epitaxial thin films of both binary ferromagnetic alloys $L1_0$-ordered FePd and FePt which were deposited onto polished single crystalline MgO(100) substrates by d.c. magnetron co-sputtering as described in III .1. The epitaxial quality, i.e. the degree of chemical long range ordering S ($0 < S < 1$) was determined by x-ray diffraction using a diffractometer in the Bragg-Brentano geometry with Cu-K_α radiation as done before [79, 80, 81]. Both samples had a well ordered $L1_0$-phase with $S = 0.8$.

To corroborate the magnetic properties of the epitaxial thin films beyond their crystallinity, the zero-field domain state in the demagnetized state has been imaged by means of x-ray magnetic circular dichroism-photoelectron emission microscopy (XMCD-PEEM) [126]. XMCD is the dependence of the absorption cross section of circularly polarized x-rays on the relative orien-

tation of helicity and the magnetization direction of the absorbing sample [127]. The XMCD effect has been employed at the Fe L_3-absorption edge at 707 eV to image the magnetic domains of the FePt and FePd thin films. These experiments were performed at the UE49-PGM, a microfocus beamline of the Berlin synchrotron radiation facility BESSY using circular polarization from the third harmonic of the helical undulator with a degree of polarization of about 85%. The optics of the beamline delivers light with a spot size of 5×8 μm^2, which is incident under an angle of 16° to the surface, so that a 34×8 μm^2 (FWHM) area of the sample is illuminated. A commercial PEEM (Elmitec PEEM-2) as described in section III .5 with magnetic lenses and electron energy filtering was used. The photon energy resolution of the beamline was approximately 200 meV at the Fe L_3-edge, with a dispersion of less than 9 $\frac{\text{meV}}{\mu\text{m}}$ within the field of view. The imaging energy filter of the instrument was set to an electron energy resolution of 0.5 eV, centered at the peak of the secondary electron distribution ($\approx$ 1 eV). Monochromating the electrons used for the laterally resolved detection of the absorption reduces the chromatic aberration of the electron optics, thus enhancing the lateral resolution. A resolution of about 40 nm could be achieved for the images presented in figure IV .22 (a) and (b). The images were recorded by a 12-bit CCD camera with 1024×1024 pixels using a binning of 2×2 pixels. The XMCD-PEEM images are represented as greyscale coded absorption asymmetry for opposite helicities of the circularly polarized x-rays, $A_{\text{XMCD-PEEM}} = \frac{I_+ - I_-}{I_+ + I_-}$, i.e. the difference of absorption images acquired with opposite helicities divided by their sum. The asymmetry is proportional to the projection of the local magnetization on the direction of incidence of the

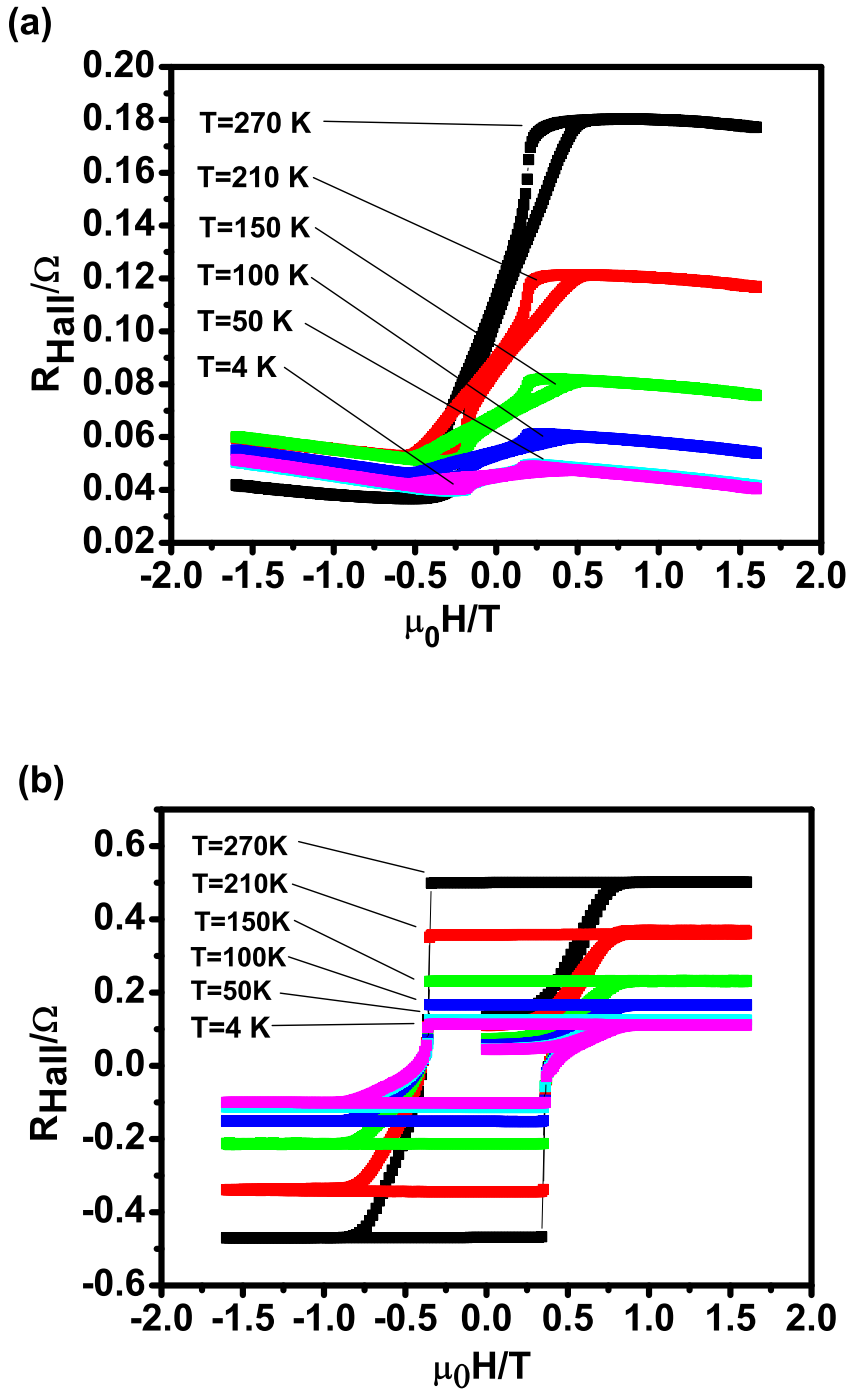

Figure IV .23: Anomalous Hall resistance R_{Hall} measured for various temperatures ranging between T = 4 K to T = 270 K. While one obtains asymmetric hysteretic Hall loops in the case of $L1_0$-FePd (a), the Hall signal of equally ordered $L1_0$-FePt shows very symmetric and even hysteresis (b).

	t nm	$0 < S < 1$	$\overline{D}_{\mathrm{PEEM}}$ nm	R_0 (50 K) $\frac{\mathrm{n\Omega cm}}{\mathrm{T}}$	R_0 (270 K) $\frac{\mathrm{n\Omega cm}}{\mathrm{T}}$	R_{S} (50 K) $\frac{\mu\mathrm{\Omega cm}}{\mathrm{T}}$	R_{S} (270 K) $\frac{\mu\mathrm{\Omega cm}}{\mathrm{T}}$	Φ_{SK} mrad
FePd	31 ± 1	0.8 ± 0.1	69 ± 20	-28.0 ± 3.0	-16.0 ± 2.0	0.01 ± 0.01	0.14 ± 0.05	(17 ± 5)
FePt	34 ± 1	0.8 ± 0.1	125 ± 30	-3.0 ± 1.0	-2.0 ± 1.0	0.12 ± 0.05	0.75 ± 0.10	(49 ± 5)

Table IV .3: Structural parameters, average domain widths $\overline{D}_{\mathrm{PEEM}}$, regular and anomalous Hall coefficients R_0 and R_{S} and average skew scattering angle Φ_{SK} for $\mathrm{L1_0}$-ordered FePt and FePd films of equal crystallographic ordering S.

light. Both domain patterns show the characteristic maze structure obtained at zero-field for the $L1_0$-ordered Fe-alloys [110, 87] investigated also by MFM before for $L1_0$-FePt in section IV .1, see figure IV .3 (a) and (b), and for $L1_0$-FePd in section IV .2.2.1, see figure IV .11 (a)-(d). The dark and bright interconnected areas shown in figure IV .22(a) and (b) represent magnetic domains of oppositely orientated magnetization perpendicular to the film plane. This demagnetized domain state corresponds to the starting point of each Hall loop at zero applied field shown in figure IV .23(a) and (b). From 1×1 μm^2 area PEEM images one determines the average domain width of $\overline{D}_{\mathrm{PEEM}} = 69$ nm for FePd and $\overline{D}_{\mathrm{PEEM}} = 125$ nm for FePt. These values correspond very well with micromagnetic simulations that have been performed on both materials using experimentally determined simulation parameters, as described in IV .1 and IV .2.2.1, i.e. $\overline{D}_{\mathrm{Oommf}} \approx 89$ nm for the FePd sample and $\overline{D}_{\mathrm{Oommf}} \approx 150$ nm for the FePt sample. See also references [87, 88].

Conventional 4-probe dc Hall measurements were performed at various temperatures ranging from $T = 4$ K to $T = 270$ K on argon-ion milled Hall bars of a width of 100 microns. The samples were demagnetized for each new measurement temperature in order to obtain a domain pattern as shown in figure IV .22(a) and (b). This domain state corresponds for the FePd and the FePt sample to $M \approx 0$ as determined from vibrating-sample magnetometry and is reflected in equal areas of light and dark contrast in the XMCD-PEEM images. The typical hysteretic property of the Hall resistance R_{Hall} is obvious in both $L1_0$-ordered FePd and FePt, see figure IV .23(a) and (b). The FePd sample shows an asymmetric evolution of the hysteretic Hall loops in R_{Hall} with increasing temperature. This is hardly visible in the FePt sam-

ple. The zero-field magnetic domain pattern shown in figure IV .22(a) for FePd and (b) for FePt for the demagnetized domain state corresponds to the center point of each loop shown in figure IV .23(a) and (b). A very weak regular Hall resistance is observable in FePd (figure IV .23(a)), noticeable in the shallow slope of the saturation regions of the Hall loop. From the high field slope a regular Hall coefficient $R_0^{\mathrm{FePd}} = \frac{d\rho_{\mathrm{H}}}{dH} = -28\ \frac{\mathrm{n\Omega cm}}{\mathrm{T}}$ at $T = 50$ K has been derived that decreases only marginally to $R_0^{\mathrm{FePd}} = -16\ \frac{\mathrm{n\Omega cm}}{\mathrm{T}}$ at $T = 270$ K, where the negative sign corresponds to negative-charge carriers, i.e. electrons. The regular Hall coefficient in the FePt sample R_0^{FePt} ranges at all temperatures an order of magnitude lower than R_0^{FePd} in FePd and can safely be considered negligible in comparison to the anomalous Hall signal itself, for details see table IV .3. Figure IV .24(a) and (b) depict the evolution of the Hall resistivity ρ_{H} and the longitudinal resistivity ρ_0 with temperature as determined by extrapolating from the magnetically saturated state back to zero field. The solid line is a parabolic fit in each case. At $T = 270$ K one observes that the anomalous Hall resistivity ρ_{H} increases by approximately a factor of three from $\rho_{\mathrm{H}} \approx 0.6\ \mu\Omega$cm in FePd to $\rho_{\mathrm{H}} \approx 1.6\ \mu\Omega$cm in FePt. At the same temperature the longitudinal resistivity ρ_0 approximately doubles from $\rho_0 = 18\ \mu\Omega$cm in FePd to $\rho_0 = 33\ \mu\Omega$cm in FePt, see upper insets of figure IV .24(a) and (b). For FePd one derives an anomalous Hall coefficient of $R_{\mathrm{S}}^{\mathrm{FePd}} = 11\ \frac{\mathrm{n\Omega cm}}{\mathrm{T}}$ at $T = 50$ K that increases to $R_{\mathrm{S}}^{\mathrm{FePd}} = 0.14\ \frac{\mu\Omega\mathrm{cm}}{\mathrm{T}}$ at $T = 270$ K. For FePt one finds an anomalous Hall coefficient of $R_{\mathrm{S}}^{\mathrm{FePt}} = 0.12\ \frac{\mu\Omega\mathrm{cm}}{\mathrm{T}}$ at $T = 50$ K that increases to $R_{\mathrm{S}}^{\mathrm{FePt}} = 0.75\ \frac{\mu\Omega\mathrm{cm}}{\mathrm{T}}$ at $T = 270$ K, see table IV .3. The offset signal ρ^*, a longitudinal resistance contribution spontaneously observed specifically in the $L1_0$-FePd sample in the demagnetized

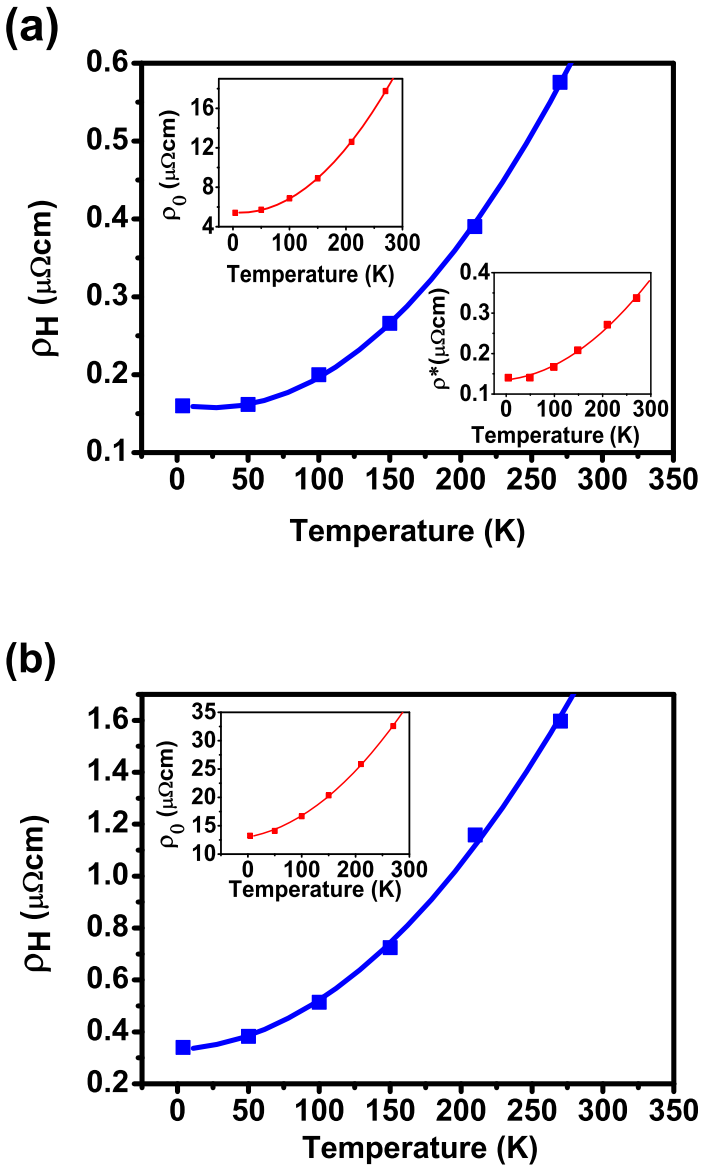

Figure IV .24: Temperature evolution of Hall resistivities ρ_H in $L1_0$-ordered FePd (a) and FePt (b) of equal crystallographic ordering as determined by extrapolating from the magnetically saturated state back to zero field. The insets to the upper left show the longitudial resistivities ρ_0 as a function of temperature while the inset in (a) to the lower right depicts the temperature evolution of the offset signal ρ^* as a consequence of a parasitic serial resistance observed in the demagnetized domain state of $L1_0$-FePd at zero field. The solid lines are fits to the data and exhibit parabolic dependence of resistivity vs. T.

domain state and in zero field as a consequence of a parasitic serial resistance. It is visible in the offset of the center of the Hall hysteresis loops shown for $L1_0$-FePd in figure IV .23(a) and is plotted versus temperature in the lower inset of figure IV .24(a). Its temperature evolution is parabolic as is the temperature dependence of the anomalous Hall signal ρ_H and the longitudinal resistivity ρ_0. This offset is rather pronounced in the case of FePd, which can be seen in the fact that the negative field branches of the hysteretic Hall loops do not exhibit negative Hall resistance values, while this type of effect is negligible in the FePt sample. ρ^* is caused by a longitudinal series resistance superimposed in the Hall measurement and possibly due to the finite size of the Hall cross of 100 microns. This in combination with a very pronounced deflection of a conduction electron per individual scattering event effectively gives rise to a longitudinal resistivity contribution [128]. This may also explain the temperature evolution of ρ^* and one may therefore attribute ρ^* to a small but noticeable longitudinal series resistance in the Hall cross geometry. This was taken into account in a corrective manner for the FePd sample by subtracting the offset signal ρ^* from the overall measured transverse signal to obtain the anomalous Hall signal ρ_H as plotted for both materials in figure IV .24 (a) and (b). Solely the corrected ρ_H was taken to determine the Z-dependence of the atomic spin-orbit scattering energy λ as described further below.

The virgin branch of the hysteretic Hall loops in the $L1_0$-FePt case shows a shift of the starting point to positive values entirely due to a minute but finite imperfection in the sample demagnetization cycle and hence the acquired accomplishment of the demagnetized domain state after the applied

demagnetization field crosses the coercive field of the sample. The demagnetization cycle with an asymptotically decreasing field amplitude alternating from positive to negative field values is much more efficient in FePd than in FePt. This is due to the fact, that on the one hand the coercive field of FePt $H_c \approx 3.5$ kOe is much larger than in FePd. On the other hand, the $\frac{dR_{\mathrm{Hall}}}{dH} \approx 0$ in FePt for fields smaller than the coercive field of the material (see figure IV .23(b)), while in FePd $\frac{dR_{\mathrm{Hall}}}{dH} \neq 0$ for fields smaller than the coercive field of the material (see figure IV .23(a)). Therefore, the position of center point of the hysteretic Hall loops for the $L1_0$-FePt sample, i.e. the starting point of the virgin branch at zero field, depends on the demagnetization history of the sample. Accordingly, the FePt sample yields a minute asymmetric absolute value of Hall resistance measured for positive and negative field saturation.

Analysis of the experimental transport data brings us to relate ρ_{H} to the longitudinal resistivity ρ_0 shown in figure IV .25 in order to clarify the underlying mechanism for the strong AHE in both $L1_0$-materials, i.e. side-jump or skew scattering or a superposition of both extrinsic effects. An intrinsic nature of the origin of anomalous Hall effect in $L1_0$-FePt and -FePd can safely be excluded as the scaling behavior would then be non-linear, i.e. $\sigma_{xy} \propto \sigma_{xx}^{1.6}$ [71], which is not the case here as can be seen in figure IV .25.

ρ_{H} was corrected for the ρ_{H}^{*} contribution. The anomalous Hall resistivity ρ_{AHE} comprising skew scattering term as well as side-jump term can be written as $\rho_{\mathrm{AHE}} = \Phi_{\mathrm{SK}} \cdot \rho_0 + \kappa\rho_0^2$ [62], wherein the quadratic term corresponds to side-jump scattering and Φ_{SK} denotes the skew scattering angle of an electron trajectory deflected in a single scattering event. In non-epitaxial thin films of elemental Fe $\kappa \neq 0$ due to crystallographic disorder [129]. The $L1_0$-

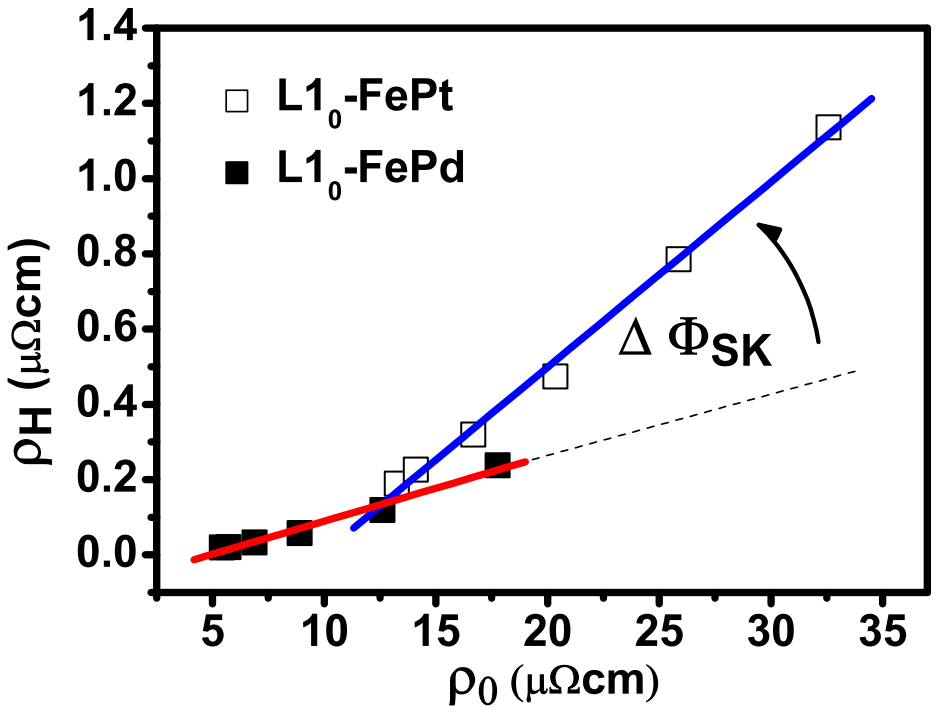

Figure IV .25: Hall resistivity ρ_H vs. longitudinal resistivity ρ_0 for $L1_0$-ordered FePd (empty squares) and FePt (filled squares). Experimental uncertainties are smaller than the data-markers. The solid lines are linear fits to the data, their difference in slope directly yields the change in skew scattering angle $\Delta\Phi_{SK} \approx 30$ mrad due to enhanced skew scattering for higher spin-orbit coupling strength in $L1_0$-ordered FePt compared to $L1_0$-ordered FePd.

ordered binary iron alloys FePd as well as FePt are materials exhibiting a diffusive current spin-polarization of $P \approx 0.8$ over a wide range of temperatures as detailed in IV .2.2 and IV .2.1, i.e. nearly only one spin-channel contributes to diffusive electron transport. Moreover, AHE in ordered ferromagnets is predicted to be governed predominantly by the skew scattering mechanism [67] of conduction electrons while disorder gives rise to an admixture of skew scattering and side jump scattering. In conventional Fe this causes the transverse resistivity to bear an additional longitudinal resistivity term of quadratic nature. Generally, a disordered system is understood to show a strong increase in side-jump mechanism.

As ρ_{H} exhibits a clear linear dependence on ρ_0 for both materials studied, one is unambiguously able to attribute AHE in $L1_0$-ordered FePd and FePt to electronic skew scattering at scattering centers bearing a localized spin moment [110, 62]. The solid lines in figure IV .25 are first order approximations of the data and the slope of each line serves as a direct measure for the skew scattering angle Φ_{SK}. It is obvious in figure IV .25 that in both materials $\kappa \approx 0$, i.e., side-jump scattering plays a negligible role. Thus the absence of the side-jump scattering in $L1_0$-FePd and -FePt is attributed to the high crystallographic ordering since skew-scattering dominates in the weak disorder limit. For $L1_0$-FePd an average skew scattering angle of $\Phi_{\mathrm{SK-FePd}} = 17$ mrad was observed whereas one determines $\Phi_{\mathrm{SK-FePt}} = 49$ mrad for equally ordered $L1_0$-FePt. Essentially, the skew scattering Hall angle nearly triples when Pd is exchanged by Pt in the binary $L1_0$-alloys of equal crystallographic ordering. The Hall angle values of FePt reach similar values as the highest Hall angles reported so far, which is observed in the iron-lanthanide alloy

FeSm [130], where it is $\Phi_{\mathrm{SK-FeSm}} = 48$ mrad in comparison. Alloying Fe with Pt instead of Pd causes the skew scattering Hall angle Φ_{SK} to increase by a factor of $\frac{\Phi_{\mathrm{SK-FePt}}}{\Phi_{\mathrm{SK-FePd}}} \approx 2.9$. This value agrees reasonably well with the ratio of spin-orbit scattering energies $\Delta\lambda_{\mathrm{Pd}}$ and $\Delta\lambda_{\mathrm{Pt}}$ estimated from the perturbation introduced by a solute atom of valence different from that of the host metal in analogy to Rutherford's principle, i.e. $\frac{\Delta\lambda_{\mathrm{Pt}}}{\Delta\lambda_{\mathrm{Pd}}} \approx 3.4$ as detailed further below. The change in atomic spin-orbit energy $\Delta\lambda$ enters the spin-orbit perturbation Hamiltonian as introduced by J. Smit [66]

$$H_{\mathrm{SO}} = \frac{2i\lambda\sigma_{\mathrm{z}}}{\Delta E} V[y\frac{\delta}{\delta x} - x\frac{\delta}{\delta y}]. \qquad \text{(IV .17)}$$

It describes the spin-orbit interaction of a conduction electron in the presence of a perturbation potential V with atomic spin-orbit energy λ, the energy difference of scattered electron wave function ΔE and σ_{z} the z-component of the Pauli-operator. In conjunction with a $Z^{3/2}$ dependence of the valence spin-orbit parameter theoretically predicted [46, 47, 48], a ratio of $\Delta\lambda$ was determined for each component of the binary alloys in FePt and FePd $\frac{\Delta\lambda_{\mathrm{Pt}}}{\Delta\lambda_{\mathrm{Pd}}} = \frac{Z_{\mathrm{Pt}}^{3/2} - Z_{\mathrm{Fe}}^{3/2}}{Z_{\mathrm{Pd}}^{3/2} - Z_{\mathrm{Fe}}^{3/2}} \approx 3.4$. In essence, the $Z^{3/2}$ dependence of the valence spin-orbit parameter confirms the tripling of the skew scattering Hall angle Φ_{SK} upon exchanging Pd ($Z_{Pd} = 106$) with the isoelectronic atomic species Pt ($Z_{Pt} = 195$).

Chapter V

Conclusion

In conclusion, both the diffusive and ballistic transport spin-polarization in high quality epitaxial sputtered $L1_0$-FePt thin films has been determined, as described in detail in IV .2.1. In the diffusive electron transport regime, magnetoresistance of domain walls was used along with a modified form of the Levy-Zhang model to determine the spin current asymmetry and hence the diffusive spin polarization of a dc current flowing in $L1_0$-FePt. In the ballistic electron transport regime, the spin polarization was extracted directly from point contact Andreev reflection measurements at $T = 4.2$ K.

Comparing the polarization in the ballistic transport regime determined in section IV .3.1 to that in the diffusive regime, one finds that at liquid He temperatures, where the comparison is direct, $P_{\text{diffusive}}$ is substantially higher. The ballistic polarization value however needs to be considered a lower limit achievable in $L1_0$-FePt thin films as PCAR does not easily allow for probing the bias voltage dependent conductance of a point contact without possibly introducing a considerable degree of disorder into the $L1_0$-phase of FePt.

The α parameters are within the range of those obtained for various im-

purities introduced as scattering centers into a $3d$ magnetic matrix [120]. For instance, a very high value of $\alpha = 35$ was found for Co impurities in a Ni matrix. It is therefore likely that the asymmetry in the scattering rates for spin-$\uparrow$ and spin-$\downarrow$ for scattering from vacancies, impurities, and antisite defects in the $L1_0$-structure leads to additional polarization in the diffusive current over and above that from the band structure alone. The spin-dependent scattering rates lead to the expectation of a rather high diffusive spin polarization of approximately 90 % at room temperature. Hence $L1_0$ -ordered FePt is an interesting material that combines a large spin-polarization with a strong spin-orbit coupling, which leads to a very strong out-of-plane anisotropy and a large anomalous Hall effect.

Furthermore, experimental evidence for impurity scattering as the decisive phenomenon in diffusive spin transport within an epitaxial ferromagnetic system was found, see section IV .2.2. Epitaxial FePd magnetic thin films of varying degrees of $L1_0$-phase chemical order were used to study the origin of domain wall magnetoresistance. The ordering was reduced by enriching the film with Pd, which also reduces the magnetization and the anisotropy constant, and increases the resistivity. Nevertheless, the domain wall magnetoresistance originating from 10 nm narrow Bloch domain walls was found to rise markedly, roughly doubling on halving the degree of chemical ordering within the epitaxial $L1_0$-FePd films. Meanwhile, there is no noticeable change in the ballistic spin-polarization, as measured by point contact Andreev reflection and interpreted by the modified Blonder-Tinkham-Klapwijk theory. By quantitatively accounting for changes in micromagnetism through simulation and magnetic force microscopy, we showed, within the Levy-Zhang

spin-mistracking theory of domain wall resistance, that this is connected to a change in the average degree of spin-dependence at the scattering centers that control the diffusive transport in this system, suggesting a possible means of producing highly spin-polarized currents in the diffusive electron transport regime.

More precisely, the increase of magnetoresistance due to domain walls DW MR with the degree of long range ordering S decreasing is due to a rise in spin-channel conductance asymmetry α and hence in a change in the ratio of exchange scattering to Coulomb scattering $|j/v|$, which was evaluated as shown table IV .2. Consequently, the ratio of spin-dependent exchange scattering versus pure Coulomb scattering is largest for the samples with the highest DW MR. Figure IV .15 (c) elucidates the linear dependence between $|j/v|$ and the content of atomic Pd within the FePd films as determined by x-ray photoelectron spectroscopy. As one has two different types of scattering centers in the films presented (i.e. Fe and Pd), these values are interpreted as ensemble averages of $|j/v|$. This indicates that the spin-dependence of scattering at deliberately introduced excess Pd atoms is stronger than at spin-dependent scattering centers within the stoichiometric FePd matrix, which in turn gives rise to an enhanced average $|j/v|$ by increasing the spin-polarization of the diffusive current via a preferred imbalance between $\tau_{\uparrow}$ and $\tau_{\downarrow}$. As the average total magnetic moment of an individual iron atom of a unit cell increases with the ordering in the film, the strength of the coupling of this mistracking to domain wall magnetoresistance is enhanced. For all degrees of ordering within the range $0.4 \leq S \leq 0.8$ one observes nearly double the spin polarization in the diffusive transport case as compared to the

ballistic case due to the relevance of spin-dependent relaxation times only in the diffusive spin transport regime. Comparing the ballistic and diffusive current spin polarization results, as plotted in figure IV .21 (a) and (b), it becomes obvious that the increased disorder is only affecting spin-polarized electron transport in the diffusive regime, see also figure IV .15 (b), where the enhanced spin-dependent scattering at an increased surplus of Pd sites accordingly have in increasing effect on both ρ and DW MR, see also table IV .1. Relating the spin-resistivity asymmetry parameter of the diffusive electron transport regime $\alpha_{\text{diffusive}}$ (see equation IV .4) with the ballistic analogon defined in equation IV .5 gives $\alpha_{\text{diffusive}} = \alpha_{\text{ballistic}} \cdot \frac{v_{\text{F}}^{\uparrow}\tau_{\uparrow}}{v_{\text{F}}^{\downarrow}\tau_{\downarrow}}$, hence one finds from the data shown in figure IV .21 a ratio of $[\frac{v_{\text{F}}^{\uparrow}\tau_{\uparrow}}{v_{\text{F}}^{\downarrow}\tau_{\downarrow}}]_{S=0.39} \approx 7$ for the lowest long range order parameter to $[\frac{v_{\text{F}}^{\uparrow}\tau_{\uparrow}}{v_{\text{F}}^{\downarrow}\tau_{\downarrow}}]_{S=0.80} \approx 4$ in the case of the highest long range order parameter within the FePd films investigated in this work.

Two main conclusions follow from this realization. On the one hand, assuming $v_{\text{F}}^{\uparrow} \neq v_{\text{F}}^{\downarrow}$ as anticipated by the spin-split Fermi surface of a ferromagnetic material, one can conclude that it is the enhancement of the product $v_{\text{F}}^{\uparrow}\tau_{\uparrow}$ for the spin-up channel over the spin-down channel, that gives rise to an approximate doubling of the effective current spin polarizations of diffuse compared to ballistic electron transport. Secondly, within the diffusive electron transport regime $\tau_{\uparrow}/\tau_{\downarrow}$ approximately doubles with the degree of crystallographic long range ordering in $L1_0$-FePd halving, see the evolution of α with S figure IV .15 (a) in section IV .2.2. This conclusion can be drawn considering, that band structure properties like Fermi velocity v_{F} and electron density of states $g(E_{\text{F}})$ remain unaffected by the Pd enrichment.

As is found in IV .2.1 for FePt, $P_{\text{ballistic}} < P_{\text{diffusive}}$ by roughly a factor of two

[87] for all samples investigated. Here it is pointed out that in PCAR spectroscopy experiments, as one probes for ballistic electron transport, there is no discernible dependence of the polarization on the sample, implying that $g(E_{\mathrm{F}})$ and v_{F}, and their spin-dependence, are little affected by the Pd enrichment, in spite of a marked reduction in magnetic moment per atom. Thus, one is able to conclude that the additional Pd has a substantial effect on transport properties in the diffusive regime: the resistivity rises, indicating additional scattering centers, which have, on average, a stronger spin-dependence $|j/v|$. The consequence is a higher spin-resistivity asymmetry coefficient $\alpha_{\mathrm{diffusive}} = \alpha$ and hence a higher DW resistance as an experimental signature. This is particularly important, as it suggests that control of the spin-dependent lifetimes may be possible through selection of appropriate dopants, giving rise to the highly spin-polarized electron currents reaching $P \approx 90 - 95$ % via extrinsic impurity scattering as shown in table IV .2.

The second extrinsic and no less important physical phenomenon in ferromagnetic materials, i.e. the anomalous Hall effect that actually has been discovered earlier than domain wall magnetoresistance, was investigated in-depth in both $L1_0$-materials explicitly fabricated in this work. A direct comparison in terms of anomalous Hall signal has been performed to clarify the nature and origin of the anomalous Hall effect in crystallographically equally ordered $L1_0$-FePd and -FePt. This investigation reveals that the extrinsic nature of spin-orbit skew scattering Hall angle scales under consideration of the $Z^{3/2}$ dependence of the valence spin-orbit parameter when substituting Pd with the isoelectronic but heavier Pt. Due to the high crystallographic ordering in both samples, no experimental evidence for the electronic side-

jump mechanism as a possible cause for AHE in the materials studied here was found. From Hall measurements at temperatures ranging from 4 K to 270 K, an average skew scattering angle of 17 mRad per single spin-orbit scattering event was determined in $L1_0$-FePd as compared to 49 mRad in the case of FePt.

The combination of a high magneto-crystalline and out-of-plane magnetic anisotropy, a pronounced and nearly temperature-independent current spin polarization and a pronounced anomalous Hall effect renders $L1_0$-FePt and -FePd as an interesting candidate both for fundamental research as well as applications in modern nanoscale spintronics.

As an outlook, further work should comprise, within the notion of nanoscale domain wall spintronics, experiments such as transport studies again both in the ballistic and the diffusive regime. More specifically, in the diffusive electron transport regime, DC but also AC characteristics of single domain walls in nanoscale wires [131, 132] of $L1_0$-ordered FePd/FePt are of particular interest. Here, photoelectron emission microscopy (XMCD-PEEM) and Lorentz-TEM experiments are planned to image domain structures and possibly the effect of currents of domain walls in nanostructures.

In the ballistic transport regime, carbon nanotubes as nanoscale ballistic conductors are proposed to investigate coherent spin transport [133, 134] between $L1_0$-FePt/FePd contacts with specific domain structure. Micromagnetic simulations of all nanostructures will be carried out using OOMMF. The structures of interest are proposed to be below 200 nm critical dimension and ought to be fabricated employing processes involving photolithography, focussed ion beam milling and electron beam lithography and/or electron

beam lithography in conjunction with argon ion milling.

Acknowledgement

I would like to acknowledge the supervision and help from both of my supervisors, Dr. C.H. Marrows and Prof. B.J. Hickey.

Furthermore, I would like to thank Dr. V. Baltz for the help with PCAR, Prof. D. Edwards and Dr. M. C. Hickey for the help with theory, Prof. J. N. Chapman and Dr. M. MacKenzie for HRTEM, Prof. W. Kuch, Dr. J. Miguel and Dr. F. Kronast for XMCD-PEEM at BESSY, Prof. M. Blamire and Dr. A. Aziz for the argon-ion milling, Dr. A. T. Hindmarch, Dr. D. McGrouther, Dr. S. Lepadatu, Prof. J. Morgan and Dr. M. Ali for their help, assistance and fruitful discussions. I am grateful for the magnetic force microscope of the Molecular and Nanoscale Physics group made available by Dr. S. Connell and Prof. St. Evans. I also would like to thank Dr. J. Cunningham, Dr. A. Blackburn, Dr. P. Steenson, Dr. J. Ebbecke, Prof. E. Linfield and Prof. A. Wixforth for their support.

The technical assistance of J. Turton, M. Patel, L. Harris and A. Price is also gratefully acknowledged.

I am in dept of my parents, brothers and family for their moral support.

I also wish to thank the UK EPSRC for my stipend within the Spin@RT scheme.

Bibliography

[1] J. A. Thornton. *J. Vac. Sci. Technol.*, 15:171, 1978.

[2] K. D. McKinstrey, C. E. Patton, C. A. Edmondson, P. J. McClure, and S. Kern. *Rev. Sci. Instrum.*, 62 (3):779, 1991.

[3] L. Abelmann. *Contribution to European School of Magnetism*, 2005.

[4] M. Birkholz. *Thin Film Analysis by X-ray Scattering.* Wiley-VCH Verlag GmbH & Co. KGaA, Weinheim, 2006.

[5] C. M. Schneider and G. Schönhense. *Rep. Prog. Phys. 65*, 81:R1785–R1839, 2002.

[6] I. Žutić, J. Fabian, and S. Das Sarma. Spintronics: Fundamentals and applications. *Rev. Mod. Phys.*, 76:323, 2004.

[7] S. Mangin, D. Ravelosona, J. A. Katine, M. J. Carey, B. D. Terris, and E. E. Fullerton. *Nature Materials*, 5:210, 2006.

[8] P. Caro, A. Cebollada, F. Briones, and M. F. Toney. *J. Cryst. Growth*, 187:426, 1998.

[9] T. Suzuki, N. Honda, and K. Ouchi. *J. Appl.Phys.*, 85:4301, 1999.

[10] S. Ishio, T. Yoshino, H. Saito, T. Suzuki, and K. Ohuchi. *J. Magn. Magn. Mater.*, 239:217, 2002.

[11] K. Barmak et al. *J. Appl. Phys.*, 95:7501, 2004.

[12] K. Barmak, J. Kim, L. H. Lewis, K. R. Coffey, M. F. Toney, A. J. Kellock, and J.-U. Thiele. *J. Appl. Phys.*, 98:033904, 2005.

[13] C. Clavero, J. M. García-Martin, J. L. Costa Krämer, G. Armelles, A. Cebollada, Y. Huttel, R. A. Lukaszew, and A. J. Kellock. *Phys. Rev. B*, 73:174405, 2006.

[14] C. H. Marrows and B. C. Dalton. *Phys. Rev. Lett.*, 92:097206, 2004.

[15] L. Berger and G. Bergamann. *The Hall effect and its Applications.* Plenum, New York, p. 55, 1980.

[16] S. Zhang. *Phys. Rev. B*, 51:3632, 1995.

[17] G. C. Cabrera and L. M. Falicov. *Phys. Status Solidi B*, 61:539, 1974.

[18] L. Berger. *J. Appl. Phys.*, 49:2156, 1978.

[19] A. D. Kent, J. Yu, U. Rüdiger, and S. S. P. Parkin. *J. Phys.: Cond. Matt.*, 13:461, 2001.

[20] D. Ravelosona, A. Cebollada, F. Briones, C. Diaz-Paniagua, M.A. Hidalgo, and F. Batallan. *Phys. Rev. B*, 59:4322, 1999.

[21] J.-U. Thiele, L. Folks, M. F. Toney, and D. K. Weller. *J. Appl. Phys.*, 84:5686, 1998.

[22] A. Aziz, S. J. Bending, H. G. Roberts, S. Crampin, P. J. Heard, and C. H. Marrows. Angular dependence of domain wall resistivity in artificial magnetic domain structures. *Phys. Rev. Lett.*, 97:206602, 2006.

[23] C. H. Marrows. *Adv. in Physics*, 54:585, 2005.

[24] H. Tanigawa, A. Yamaguchi, S. Kasai, T. Ono, T. Seki, T. Shima, and K. Takanashi. *J. Appl. Phys.*, 99:08G520, 2006.

[25] T. Seki, S. Mitani, K. Yakushiji, and K. Takanashi. *Appl. Phys. Lett.*, 88:172504, 2006.

[26] P. M. Levy and S. Zhang. *Phys. Rev. Lett.*, 79:5110, 1997.

[27] M. Viret, D. Vignoles, D. Cole, J. M. D. Coey, W. Allen, D. S. Daniel, and J. F. Gregg. Spin scattering in ferromagnetic thin films. *Phys. Rev. B*, 53:8464, 1996.

[28] G. Binasch, P. Grünberg, F. Saurenbach, and W. Zinn. *Phys. Rev. B*, 39:4828, 1989.

[29] M. N. Baibich, J. M. Broto, A. Fert, F. Nguyen van Dau, F. Petroff, P. Eitenne, G. Creuzet, A. Friederich, and J. Chazelas. *Phys. Rev. Lett.*, 61:2472, 1988.

[30] W. Gerlach and O. Stern. *Zeitschrift für Physik*, 6:353, 1922.

[31] P. Grünberg. *Physik Journal*, 6:33, 2007.

[32] N. F. Mott. *Proc. Roy. Soc.*, 153:699, 1936.

[33] N. F. Mott. *Proc. Roy. Soc.*, 156:368, 1936.

[34] N. F. Mott. *Adv. Phys.*, 13:325, 1964.

[35] M. Jullière. *Phys. Lett. A*, 54:225, 1975.

[36] J. C. Slonczewski. *J. Magn. Magn. Mater.*, 159:L1, 1996.

[37] L. Berger. *Phys. Rev. B*, 54:9353, 1996.

[38] J. A. Katine, F. J. Albert, R. A. Buhrman, E. B. Myers, and D. C. Ralph. *Phys. Rev. Lett.*, 84:3149, 2000.

[39] S. S. P. Parkin. *US Patent*, page 6834005, 2004.

[40] N. Vernier, N. A. Allwood, D. Atkinson, M. D. Cooke, and R. P. Cowburn. *Euro. Phys. Lett.*, 65:526, 2004.

[41] D. Ravelosona, D. Lacour, J. A. Katine, B. D. Terris, and C. Chappert. *Phys. Rev. Lett.*, 65:117203, 2005.

[42] M. Kläui, P.-O. Jubert, R. Allenspach, A. Bischof, J. A. C. Bland, G. Faini, U. Rüdiger, C. A. F. Vaz, L. Vila, and C. Vouille. *Phys. Rev. Lett.*, 95:026601, 2005.

[43] M. Feigensohn, J. W. Reiner, and L. Klein. *Phys. Rev. Lett.*, 98:247204, 2007.

[44] M. Hayashi, L. Thomas, C. Rettner, R. Moriya, and S. S. P. Parkin. *Nat. Phys.*, 3:21, 2007.

[45] E. H. Hall. *Philos. Mag.*, 12:157, 1881.

[46] F. Herman and S. Skillman. *Atomic structure calculations.* Prentice-Hall, 1963.

[47] J. Friedel. *J. Phys. Chem. Solids*, 25:781, 1964.

[48] K. P. McKenna and G. J. Morgan. *Eur. Phys. J. B*, 59:451, 2007.

[49] J. Bass and W. P. Pratt Jr. *J. Phys.: Condens. Matter*, 19:183201, 2007.

[50] P. M. Levy, S. Zhang, and A. Fert. *Phys. Rev. Lett.*, 65:1643, 1990.

[51] C. Kittel. *Solid State Physics*. Wiley and Sons, New York, 2005.

[52] G. E. Blonder et al. *Phys. Rev. B*, 25:4515, 1982.

[53] S. K. Upadhyay, A. Palanisami, R. N. Louie, and R. A. Buhrmann. *Phys. Rev. Lett.*, 81:3247, 1998.

[54] R. J. Soulen, J. M. Byers, M. S. Osofsky, B. Nadgorny, T. Ambrose, S. F. Cheng, P. R. Broussard, C. T. Tanaka, J. Nowak, J. S. Moodera, A. Barry, and J. M. D. Coey. *Science*, 282:85, 1998.

[55] G. J. Strijkers, Y. Ji, F. Y. Yang, C. L. Chien, and J. M. Byers. *Phys. Rev. B*, 63:104510, 2001.

[56] A. F. Andreev. *Sov. Phys. JETP.*, 37:5015, 1988.

[57] Y. V. Sharvin. *Zh. Éksp. Teor. Fiz. [Sov. Phys. JEPT 21, 655 (1965)]*, 48:984, 1965.

[58] R. Landauer. *IBM J. Res. Dev.*, 1:223, 1957.

[59] L. Landau and E. Lifshitz. *Physik. Z. SU.*, 8:153, 1935.

[60] T. L. Gilbert. *Phys. Rev.*, 8:1243, 1955.

[61] W. F. Brown Jr. *Micromagnetics*. Krieger New York, 1978.

[62] R. C. O'Handley. *Modern magnetic materials : principles and applications*. Wiley, New York, 2000.

[63] R. Karplus and J. M. Luttinger. *Phys. Rev.*, 95:1154, 1954.

[64] L. Berger. *Phys. Rev. B*, 2:4559, 1970.

[65] J. Smit. *Physica*, XXI:877, 1955.

[66] J. Smit. *Physica*, XXIV:39, 1958.

[67] A. Crépieux and P. Bruno. *Phys. Rev. B.*, 64:014416, 2001.

[68] V. K. Dugaev, A. Crépieux, and P. Bruno. *Phys. Rev. B*, 64:104411, 2001.

[69] A. Langenfeld and P. Wölfle. *Phys. Rev. Lett.*, 67:739, 1991.

[70] L. Berger. *Phys. Rev. B*, 5:1862, 1972.

[71] S. Onoda, N. Sugimoto, and N. Nagaosa. *Phys. Rev. Lett.*, 97:126602, 2006.

[72] J. L. Vossen and W. Kern, editors. *Thin film processes*. Academic Press, Inc., 1978.

[73] R. Behrisch, editor. *Sputtering by particle bombardment*. Springer, Berlin, 1981.

[74] G. K. Wehner. *Rep. No. 2309*. General Mills, Minneapolis, 1962.

[75] D. L. Smith. *Thin-film deposition : principles and practice*. McGraw-Hill, New York, London, 1995.

[76] S. Foner. *Rev. Sci. Inst.*, 30:548, 1959.

[77] D. Jiles. *Magnetism and magnetic materials*. Chapman Hall, 1991.

[78] S. Chikazumi and C. D. Graham Jr. *Physics of ferromagnetism*. Clarendon Press, Oxford, 1997.

[79] B. E. Warren. *X-ray Diffraction*. Addison-Wesley, Reading, PA 1969, 1969.

[80] C. H. Macgillaury, G. D. Rieck, and K. Lonsdale, editors. *International Tables for X-ray Crystallography, Vol.III*. The Kynoch Press, Birmingham, England, 1962.

[81] J. A. Ibers and W. C. Hamilton, editors. *International Tables for X-ray Crystallography, Vol.IV*. The Kynoch Press, Birmingham, England, 1974.

[82] V. Holy, U. Pietsch, and T. Baumbach. *High resolution x-ray scattering from thin films and multilayers*, volume 149 of *Springer Tracts in Modern Physics*. Springer, Heidelberg, Berlin, 1999.

[83] A. Hubert and R. Schaefer. *Magnetic Domains*. Springer, Berlin, 1998.

[84] H. Hopster and H. P. Oepen. *Magnetic microscopy of nanostructures*. Springer Berlin London, Nanoscience and Technology, 2005.

[85] D. Sarid. *Scanning force microscopy : with applications to electric, magnetic, and atomic forces*. Oxford Universiy Press, 1994.

[86] M. Viret, Y. Samson, P. Warin, A. Marty, F. Ott, E. Søndergård, O. Klein, and C. Fermon. *Phys. Rev. Lett.*, 85:3962, 2000.

[87] K. M. Seemann, V. Baltz, M. MacKenzie, J. N. Chapman, B. J. Hickey, and C. H. Marrows. *Phys. Rev. B*, 76:174435, 2007.

[88] K. M. Seemann, M. C. Hickey, V. Baltz, B. J. Hickey, and C. H. Marrows. to be published, 2007.

[89] S. M. Sze. *VLSI Technology*. McGraw-Hill, 1988.

[90] M. J. M. de Jong and C. W. J. Beenakker. *Phys. Rev. Lett.*, 74:1657, 1995.

[91] B. Nadgorny, I. I. Mazin, M. Osofsky, R. J. Soulen, P. Broussard, R. M. Stroud, D. J. Singh, V. G. Harris, A. Arsenov, and Y. Mukovskii. *Phys. Rev. B*, 63:184433, 2001.

[92] Y. Ji, G. J. Strijkers, F. Y. Yang, C. L. Chien, J. M. Byers, A. Anguelouch, G. Xiao, and A. Gupta. *Phys. Rev. Lett.*, 86:5585, 2001.

[93] G. T. Woods, R. J. Soulen, Jr., I. Mazin, B. Nadgorny, M. S. Osofsky, J. Sanders, H. Srikanth, W. F. Egelhoff, and R. Datla. *Phys. Rev. B*, 70:054416, 2004.

[94] Y. Bugoslavsky et al. *Phys. Rev. B*, 71:104523, 2005.

[95] C. Hammond. *Basics of crystallography and diffraction*. Oxford University Press, 1997.

[96] A. Rettori and D. Pescia. *Fundamental aspects of thin film magnetism.* World Scientific, 2000.

[97] S. Chikazumi. *Physics of Magnetism.* Wiley and Sons, 1964.

[98] R. M. Bozorth. *Ferromagnetism.* IEEE Press, 1993.

[99] E. Beaurepaire, H. Bulou, F. Scheurer, and J.P. Kappler. *Magnetism: A Synchrotron Radiation Approach.* Springer Berlin Heidelberg, 2006.

[100] R. F. C. Farrow, D. Weller, R. F. Marks, M. F. Toney, A. Cebollada, and G. R. Harp. *J. Appl. Phys.*, 79:5967, 1996.

[101] G. H. O. Daalderop, P. J. Kelly, and M. F. H. Schuurmanns. *Phys. Rev. B*, 44:12054, 1991.

[102] K. Inoue, H. Shima, A. Fujita, K. Oikawa, K. Fukamichi, and K. Ishida. *Appl. Phys. Lett.*, 88:102503, 2006.

[103] S. Okamoto, N. Kikuchi, O. Kitakami, T. Miyazaki, and Y. Shimada. *Phys. Rev. B*, 66:024413, 2002.

[104] V. Gehanno, A. Marty, B. Gilles, and Y. Samson. *Phys. Rev. B*, 55:12552, 1997.

[105] M. MacKenzie, J. N. Chapman, S. Cardoso, H. Li, R. Ferreira, and P. P. Freitas. *J. Phys. D: Appl. Phys.*, 38:1869, 2005.

[106] S. Datta and B. Das. *Appl. Phys. Lett.*, 56:665, 1990.

[107] L. Berger. Exchange interaction between ferromagnetic domain wall and electric current in very thin metallic films. *J. Appl. Phys.*, 55:1954, 1984.

[108] G. Tatara and H. Kohno. Theory of current-driven domain wall motion: Spin transfer versus momentum transfer. *Phys. Rev. Lett.*, 92:086601, 2004.

[109] I. I. Mazin. How to define and calculate the degree of spin polarization in ferromagnets. *Phys. Rev. Lett.*, 83:1427, 1999.

[110] J. Yu, U. Rüdiger, A. K. Kent, R. F. C. Farrow, R. F. Marks, D. Weller, L. Folks, and S. S. P. Parkin. *J. Appl. Phys.*, 87:6854, 2000.

[111] B. Raquet, M. Viret, P. Warin, E. Sondergard, and R. Mamy. *Physica B*, 294-295:102–106, 2001.

[112] B. Raquet, M. Viret, E. Søndergård, O. Cespedes, and R. Mamy. Electron-magnon scattering and magnetic resistivity in $3d$ ferromagnets. *Phys. Rev. B*, 66:024433, 2002.

[113] M. W. Stringfellow. *J. Phys. C*, 1:950, 1968.

[114] A. B. Pippard. *Magnetoresistance in metals*. Cambridge studies in low temperature physics. Cambridge University Press, Cambridge, 1989.

[115] J. M. MacLaren, R. R. Duplessis, R. A. Stern, and S. Willoughby. *IEEE Trans. Magn.*, 41:4374, 2005.

[116] C. H. Kant, O. Kurnosikov, A. T. Filip, P. LeClair, H. J. M. Swagten, and W. J. M. de Jonge. *Phys. Rev. B.*, 66:212403, 2002.

[117] M. Donahue and D. G. Porter. *OOMMF User's Guide, Version 1.0*. Interagency Report NISTIR 6376. National Institute of Standards and Technology, Gaithersburg, MD, 1999.

[118] D. Hinzke, N. Kazantseva, U. Nowak, O. N. Mryasov, P. Asselin, and R. W. Chantrell. Domain wall properties of fept: From bloch to linear walls. *Phys. Rev. B*, 77:094407, 2008.

[119] I.M. Ward and J. Sweeney. *An introduction to the mechanical properties of solid polymers*. Wiley, New York, 2004.

[120] H. A. M. van den Berg. *Magnetic multilayers and giant magnetoresistance: fundamentals and industrial applications*, volume 37 of *Springer series in surface sciences*, page 215. Springer-Verlag, Berlin, 2000.

[121] D. García, R. Casero, M. Vázquez, and A. Hernando. Calculated magnetocrystalline anisotropy of a fepd ordered alloy: Electron-density dependence on the direction of magnetization. *Phys. Rev. B*, 63(10):104421, Feb 2001.

[122] M. C. Hickey. Calculated magneto-resistance due to domain walls : the role of impurity scattering. *arXiv:0805.0443*, 2008.

[123] G. Bergmann and M. Zhang. *arXiv:cond-mat*, page 0501321v1, 2005.

[124] A. Hamzić, S. Senoussi, I. A. Campbell, and A. Fert. *Solid State Communications*, 26:617, 1978.

[125] A. P. Mihai, J. P. Attané, A. Marty, P. Warin, and Y. Samson. *Phys. Rev. B*, 77:060401(R), 2008.

[126] J. Stöhr, Y. Wu, B. D. Hermsmeier, M. G. Samant, G. R. Harp, S. Koranda, D. Dunham, and B. P. Tonner. *Science*, 259:658, 1993.

[127] H. Ebert. *Rep. Prog. Phys.*, 59:1665, 1996.

[128] C. M. Hurd. *The Hall effect in metals and alloys*. Plenum Press, New York, 1972.

[129] T. Miyasato, N. Abe, T. Fujii, A. Asamitsu, S. Onoda, Y. Onose, N. Nagaosa, and Y. Tokura. *Phys. Rev. Lett.*, 99:086602, 2007.

[130] T. W. Kim, S. H. Lim, and R. J. Gambino. *J. Appl. Phys.*, 89:7212, 2001.

[131] E. Saitho, H. Miyajima, T. Yamaoka, and G. Tatara. *Nature*, 432:203, 2004.

[132] A. Yamaguchi, H. Miyajima, T. Ono, Y. Suzuki, S. Yuasa, A. Tulapurkar, and Y. Nakatani. *Appl. Phys. Lett.*, 90:182507, 2007.

[133] C. Schönenberger. *Semicond. Sci. Technol.*, 21:S1–S9, 2006.

[134] L. E. Hueso, J. M. Pruneda, V. Ferrari, G. Burnell, J. P. Valdés-Herrera, B. D. Simons, P. B. Littlewood, E. Artacho, A. Fert, and N. D. Mathur. *Nature*, 445:410, 2007.